

Answers to reviewer 1

We thank the reviewer for the detailed comments, and apologize for the confusion in the description of the thinning function. We found that answers to some of the issues were present in previous drafts of these sections but had been cut in accordance with the desire for a shorter and more streamlined text from the first set of reviews, so we appreciate the opportunity to explain them more. We have changed the description in the main text and added a new section in the supplementary material. We chose to put much of the detail in the supplement because out of the four reviews, only this referee showed particular interest in the thinning function. Therefore, we elected to keep the main text streamlined without adding too many details on the ice-flow modeling.

See below for detailed responses.

The paper estimates a record of snow accumulation for the last 2,700 years at Roosevelt Island, Antarctica. The record shows a decrease in accumulation since the mid-1960s that Bertler et al (2018) relate to an increase in sea ice extent.

The authors extract the information from an ice core following two main steps:

- Obtaining a detailed chronology that combines annual-layer counting, that follows the seasonality traces of a few chemical constituents, and a few historical constraints, like well dated volcanic eruptions.
- Estimating the past-accumulation records from the thickness of annual layers. For this, the authors have to estimate the influence of ice-flow from the time of deposition on the surface to the present: compaction from snow to ice, and compression.

In general, the document is clear and well written. I find a strong difference in level of detail between the sections related to ice-core analysis and establishing a chronology, and the sections related to ice-flow and deriving an accumulation record. More of that later.

I am not an expert on ice-core analysis so I will only say that the description of the methods in those sections reads well and they seem to be referenced. I have however serious concerns related to the reconstruction of past accumulation rates. I will group my concerns in terms of clarity, methodology and uncertainty.

Clarity

Sections 5.2 and 5.3 are simply not clear. Technical terms are not explained or referenced. For example: Raymond stack, divide migration, divide/flank flow transitional type flow or thinning function.

Indeed, the reference to Raymond 1983 had gotten cut from this section, and we have added it back. We have rewritten sections 5.2 and 5.3, and also added a more detailed description of divide and flank flow, and reference Nereson and Waddington (2002), which provides much greater detail on how divide migration affects the internal layering in an ice sheet.

A few important steps are not described or referenced. For example:

- How do the authors extract the information about the divide migration from the radar stratigraphy.

We infer the divide migration from the location of peak amplitude of the Raymond arch. The peak is nearly beneath the modern divide in the shallowest layers, but by about 120m depth is about 500m east. We

have revised and added to the paragraph describing this line of argument, and reference Nereson and Waddington (2012) on the interpretation of internal layering in terms of divide migration.

-How do they derive the thinning function from a vertical velocity that varies in depth and in time.

We have more fully described that we use a transient 1-D model which tracks layer thinning with an annual time step. We iterate to find consistent values of the time-varying accumulation history and the modeled thinning.

-How do they calculate the present surface thinning. The authors state that they use an ice-flow model to match the dated architecture of the Raymond stack. What ice-flow model? 1D, 2D? Using the velocity profile that they describe below and the time-varying vertical velocity implied by the time-varying accumulation?

A full response to this comment will require a manuscript of its own (which we are working on), but we consider this to be beyond the scope of a paper focused on the timescale. To answer, we have two lines of support for the current thinning rate.

The first is from the fitting of the pRES vertical velocity profiles. The vertical velocity at the surface is equal to the sum of the accumulation rate and the ice-sheet thinning rate. We know that the current average accumulation rate is approximately 24cm ice eq/yr. So when fitting the vertical velocity profile to the measurements, any difference between the surface velocity of the fit and the accumulation rate is the ice-sheet thickness change. Kingslake et al. (2014) obtains the best fit for the divide with a surface velocity of 27cm/yr, implying 3-5cm/yr of thinning. However, with this profile, the Lliboutry fit yields too low vertical velocities at mid-depths (40-70% of ice thickness) compared to the measurements. The fit improves with more negative values of the Lliboutry parameter p , but this also requires a higher vertical surface velocity, which becomes unrealistic (more on that below). Kingslake et al. (2014) noted that there is a region of near-linear vertical velocity change in the pRES measurements (Kingslake, Figure 5). We found that continuing the slope starting at approximately 80% of the ice thickness yielded a surface velocity of 26 cm/yr, in line with the current accumulation rate and modest ice-sheet thinning.

The second line of support is from ice-flow modeling. We have used both 1D and 2D models, with both constant and time-varying accumulation rate histories. For 1D, we matched the bump amplitude (as in Conway et al., 1999, Figure 3). For 2D, we have matched the layers directly as well as the bump amplitude. The overall conclusion is that the divide was established at about 3ka and that there is a small amount of thinning; a couple of cm. However, a unique solution is elusive. The lack of velocity measurements near the surface creates uncertainty in the development of the Raymond Arch (and even if there were measurements in the firn column, distinguishing the effect of ice-flow thinning from firn compaction would be tricky). During development of the Raymond Arch, different choices of the vertical strain profile near the surface can be balanced by varying the accumulation history, these forming a similar depth-amplitude relationship. The lack of a strong constraint on the surface vertical velocity is a particular challenge. In addition to impacting the inference of ice-sheet thickness change and the vertical strain profile, it also impacts the implementation of the vertical velocities in 2D. For instance, the variations in near-surface vertical velocity inferred by Kingslake et al. (2014) in Figure 5 could be due to either spatial variations in the ice dynamics or in the accumulation rate at the surface.

Methodology

It is difficult to assess the quality of the methods without fully understanding them. However I want to make a few points with my current understanding of the methods but, in any case, the authors should discuss these points further.

-Divide Migration. The authors make a strong assumption about a divide migration of 500m amplitude between 500yr and 250yr ago. It has a strong effect on accumulation records, particularly when combined with the arbitrary vertical velocity profile assumed. I believe this is the main difference between the accumulation records between the initial and the revised version of the manuscript. 'The correction'.

The 'correction' referred to by the reviewer was the correction of a simple miscalculation of the accumulation rate uncertainties in the original manuscript. In the previous manuscripts, the uncertainty on the thinning rate was given as a percentage of the total thinning. By mistake, instead of using it as a percentage, in the first version of the manuscript these uncertainties were used as absolute values. Correspondingly, with the correct calculation in the revised manuscript, the uncertainties on the past accumulation rates were significantly reduced. There was no change in the most likely thinning function or accumulation history between the two manuscripts.

The assumption on the divide migration history does not impact the inferred accumulation rate history that much, as will be discussed more below. In the new version of the manuscript, we have expanded and recalculated the uncertainties on the thinning function, and here include the possibility that there has been no migration of the divide over time. The obtained uncertainties are reasonably similar to those previously estimated.

The authors assume that this should be evident by looking at Figure 6c. I disagree. In this particular case, we have radar-derived englacial strain-rates (Kingslake et al, 2014; Fig. 6b). The stronger near surface strain-rates are indicating where the weak strain-rates near the bed are at the present. Curiously enough, that area coincide in Figure 6b with the location of the Raymond stack. This shows that a) no migration has occurred as present Raymond area is on top of the bottom-most Raymond bumps and the tilt in Raymond stack is consequence of other factors, or b) the divide has gone back and forth recently. In any case, it is not evident what the authors are assuming and I have bough a new argument to the table.

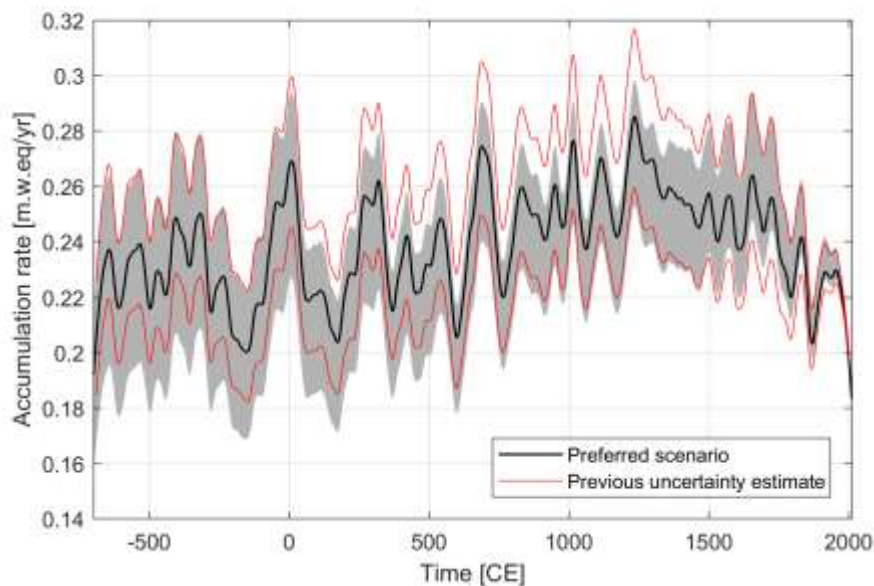
We believe a recent migration of the divide, and divide-flow, is the most likely scenario given the observed tilt in the Raymond arch (e.g. Nereson & Waddington, 2002). However, we agree that the offset in the Kingslake et al. (2014) region of inferred maximum near-surface strain rate from the present topographic divide introduces complexity into the interpretation - the physical topographic divide and the location of maximum divide flow are not necessarily the same. We note that Kingslake find the strongest near-surface strain rates ~200m east of the drill site, whereas the peak of the Raymond arch is located ~500m east. However, as described below there is significant uncertainty in the derivation of near-surface strain rates from the pRES measurements.

In developing our most likely scenario, we first assessed the uncertainty of the vertical velocity profiles and inferred near-surface strain rates from the pRES measurements (Kingslake et al., 2014). We noted that different radar polarizations resulted in large differences in inferred near-surface strain (Figure 6 in Kingslake et al., 2014), with one near-maximum value west of the summit. Given that there are few measurements in the upper 150m (none in the upper 90m) and the near-surface strain rate is an extrapolation from the upper half of the ice sheet, we could not exclude that the current topographic divide has a vertical velocity and near-surface strain rate very similar to the representative divide vertical velocity profile. Thus we considered the most likely scenario that the divide and divide-flow are co-located and the tilt in the peak of the Raymond Arch reflect the divide migration.

For the purpose of this manuscript, the larger point raised by the reviewer is not the specifics of divide migration, but the impact on the inferred thinning function and hence accumulation rate history. We have expanded the uncertainty on the accumulation rate following a more detailed analysis of possible scenarios, as discussed in the supplement. As part of the new uncertainty estimate, we have recalculated

the thinning function using the assumption of stable divide-flow, with the maximum strain rates located slightly east of the ice core drill site. The bump amplitude at mid-depths beneath the core site today is approximately 70% of the peak amplitude and the inferred (by Kingslake et al., 2014) near-surface vertical strain is also approximately 70% of the maximum measured surface strain rate. If the center of the divide-flow has been consistently offset from the physical divide, the ice in the core would have experienced transitional flow (70% divide-flow, 30% flank-flow) for all of the past 3ka, including the past 500 years.

A comparison of the new uncertainties to our previous estimates is shown in the figure below. For some sections, the new uncertainty estimate is smaller than our previous estimate, where we in a simple (and conservative) way accounted for the uncertainties associated with the vertical velocity profile. The uncertainties in the deeper part of the core has become slightly larger compared to the previous estimate, but otherwise the two uncertainty estimates are fairly similar.



-Vertical velocity at the divide. The authors assume that the ice-core site is currently at the divide position and they assume that that corresponds with the divide-type velocity ($\rho=-1.22$ in this paper; $\rho=-0.78$ in Kingslake et al (2014)). However a close inspection to Figure 6b reveals that the 'divide flow' in Figure 4 of Kingslake et al (2014) and Figure 6a in this paper is taken from about 500m east in the Figure of the summit position (green marker in Kinslake et al 2014). This position corresponds currently with the bottom-most position of the Raymond stack and not the ice-core location. This raises an important concern as, in summary, they are assuming that for the last 250yr the strain-rates are distributed following a distribution that does not correspond with the current conditions at the ice core site.

The divide-type flow profile is taken approximately 200m, not 500m, east of the ice core location.

As previously mentioned, the strain rates in Kingslake et al (2014), Figure 6b, have considerable uncertainty and were obtained from the depth interval ~130m-400m. Thus, we considered the vertical velocity profile presented by Kingslake et al. (2014) in Figure 5 as representative for the divide flow velocity profile at Roosevelt Island, regardless that it is not co-located with the current ice-divide. As discussed above, we have also presented scenarios that do not assume a recent transition to full-divide flow for the ice core.

-Vertical velocity at the flank. The authors use an arbitrary combination of two measured vertical velocities. From a combination of 0.7 this and 0.3 of that. Why? There is no explanation and it has a strong impact on the results before 250yrs ago.

For flank-flow, we use the flank-flow velocity profile found by Kingslake et al (2014), figure 4. For flow that is a mix between flank flow and pure divide flow, we use a linear combination of the velocity profiles appropriate for the two flow regimes, following Nereson and Waddington (2002). This allows a smooth transition as the flow regime transitions from partial to full divide-like flow.

The weighting of the two velocity profiles (70% divide flow, 30% flank flow) during the early period, is found from the relative amplitude of the Raymond Arch at the site: The ice core intersects the Raymond Arch at mid-depths at about 70% of the maximum arch amplitude, which we use as an indicator for the importance of divide-like flow. This is now better explained in the manuscript.

-Combination of flank/divide velocities. I have argued that I don't think there is a migration. However, even in that case, why do the authors use the wrong shape functions? There are, according to Kingslake et al (2014), 35 englacial profiles at Roosevelt Island, one of them is really close to the ice-core site. Wouldn't it make sense to use the englacial velocity from the site that is closest to the ice-core site?

First of all, there is considerable noise in individual englacial pRES velocity profiles. Secondly, what we want to obtain from the data in Kingslake et al. are typical "flank-flow" and "divide-flow" velocity profiles. We therefore choose to use the divide and flank profile that were presented in detail in Kingslake et al. (2014), both because these are the cleanest profiles and because they are the most accessible being shown explicitly in their Figure 4.

-Vertical velocity to thinning function. I mentioned earlier that the authors do not explain how do they calculate the thinning function. I just want to highlight here that this is not a trivial point as thinning function includes the cumulative effect of vertical compression from the surface that, in turn, depends on the time-varying accumulation that is unknown (e.g., Parrenin et al (2007) suggest an iterative method). The authors however assume a vertical velocity related to present values of surface accumulation and a varying shape function.

This is now more fully explained in the text. We use a 1-D model with an annual time-step with one iteration. In the first model run, we use a constant accumulation rate. We use the inferred thinning function to calculate the time-varying accumulation rate and then rerun the model. In this second iteration, at each timestep, the vertical velocity profile is scaled by the annual accumulation rate (plus the thickness change rate). We found that additional iterations yielding insignificant changes. While the surface vertical velocity likely does not vary at annual timescales, the resulting thinning functions are smooth, and no significant differences came from using a smoothed accumulation rate history.

Uncertainty.

It is difficult for me to predict the cumulative effect of all the factors I have just mention but, independently of them, the propagation of uncertainty has to be improved.

- I see no problem with the paper showing a favourite hypothesis, a divide migration, but the uncertainty should cover other other hypothesis: from no migration to a more recent migration. All this should be covered by repeating the estimation of accumulation with flank and divide velocities and showing them as two extreme cases within a range of scenarios.

- Also, I reiterate that I don't know how the authors estimate the thinning function. However, they should include in the uncertainty the effect of assuming constant the present accumulation rate and thinning

rate in the derivation of the time-dependent accumulation. The authors currently estimate sensitivity by comparing the effect of assuming $(0.24+0.02)$ m/yr with 0.24 m/yr. My view is that this is a clear underestimation of uncertainty. It should include, at least, the variability of the derived accumulation records through the time of interest, around 0.2m/yr to 0.28m/yr, to capture the uncertainty induced by this assumption.

As recommended by the reviewer, we have expanded our discussion of the uncertainty, and now calculate the uncertainty from an ensemble of different scenarios, including changes in the divide migration history over time, the extreme being no migration at all. As shown, the resulting uncertainties on the accumulation history are, however, relatively similar to our previous estimate.

The thinning function is calculated with a time-varying accumulation history which scales the vertical velocity profile. This is now explained better in the text, and we think we have satisfied this recommendation.

Answers to reviewer 2

We thank the reviewer for the thorough comments, and have revised and improved the manuscript accordingly. We have e.g. added a figure showing the annual layer counts for different depth sections, and expanded our discussion on the volcanic matching process in the manuscript. The paper now also includes two additional figures showing the volcanic matching in other depth sections (in the supplementary), and we have added to table 2 a measure for the statistical significance of peak size of the individual volcanic match-points in RICE.

See below for detailed responses.

Review of revised manuscript "A 2700-year annual timescale and accumulation history for an ice core from Roosevelt Island, West Antarctica" by Mai Winstrup et al.

In their revised manuscript the authors made a serious effort to address the issues raised in the first round of reviews. The manuscript has been restructured for clarity and several potential sources of misunderstanding have been eliminated. In particular the independence of the RICE17 age scale w.r.t the WAIS Divide ice core chronology is now made clear. Likewise the manuscript benefits from several related publications now being published or accessible in their discussion stage. This especially concerns the companion paper of Lee et al.

However, there are still two fundamental issues to be fully resolved before the manuscript can be considered for final publication in CP.

1) The automated annual layer counting by the StratiCounter algorithm is the backbone of the RICE17 chronology, but the authors provide no evidence of its performance in identifying annual layers, especially for the deeper and more thinned core sections. At present, the manuscript only contains one figure (Fig. 4) showing the manual assignment of annual layers in a very shallow section of the core, which is not enough. A separate figure would be needed showing exemplarily the automated layer identification. Of special interest here would be the depth section that has been manually counted to initialize the algorithm, as well as part of the deep sections with thinned layers.

As an added benefit, such a figure would also provide evidence of how clear an annual signal can be counted in the various proxies - here referring to the discussion in the first round of reviews about using BC vs. H+ for counting.

Although the main text would be adequate, I suppose the figure could also be placed in the supplement part S2 if the authors would not like to further increase the volume of the main manuscript.

We agree with the reviewer that the automated layer counting and the CFA data, on which it is based, ought to be illustrated in the manuscript. We have followed the reviewer's suggestion to add a figure showing the layer-counts in three different depth sections of the core, including a deep section and a section with manual layer counts (these also being shown). We eventually decided to place the figure in the main text, and now refer to it when discussing the clarity of annual signal in the various proxies.

The performance of StratiCounter has been thoroughly documented in several previous papers, e.g. Winstrup et al, 2012, Winstrup 2016. It has here been shown that the algorithm is able to produce an unbiased counting even in very noisy data series, for which it is hard to manually count layers in an unbiased fashion. We note that we initiated the algorithm on basis of a set of layer counts, which was

known to have a bias, since according to this initial timescale, the age of the Pleiades tephra was significantly (25 years) younger from that in the WAIS Divide core. However, all StratiCounter timescales placed the age of this tephra layer within a narrow age interval (± 10 years) around the WAIS Divide age. We took this as a sign that StratiCounter performed well in producing a layer counted timescale for RICE. This was further supported by the volcanic matching to WAIS Divide, described in the next comment.

2. The volcanic identification and matching against WAIS remains elusive to me and needs to be clarified further. The detection of a presumably volcanic signal in the various proxies seems to rest on manually selecting even small peaks in the signals. The manual approach appears somewhat arbitrary by comparison to the automated annual layer counting procedure. This is especially so since the authors are aware of the difficulties associated with the high background of non-volcanic sulphur/sulfate and acidity and state to have removed a number of peaks previously considered as volcanic markers. At present, it appears questionable and unclear from the manuscript how reliably volcanic signals are in fact recorded at RICE. Hence, selecting volcanic signals would benefit from a more quantitative detection technique, or at least from employing clearly stated criteria.

First, we note that the majority of peaks (>80%) that were removed from the original table were peaks in the RICE acidity/sulfur records, which were not related to any counterpart in the WAIS Divide core. These were removed from table 2, as they were of no use for evaluation the timescale, and as they may possibly originate from an oceanic rather than volcanic emission source. As we do not include volcanic peaks that – for one reason or another – could not be unambiguously matched to a corresponding peak in WAIS Divide, many peaks of likely volcanic origin in the RICE records are not included in table 2. This has been clarified in the manuscript.

The volcanic matching was indeed difficult for RICE, as also stated in the paper. The matching relied significantly on having accurate layer-counted timescales for both cores. Comparing the ice core records on their respective timescales, we were able to find in both cores a similar series of acidity peaks spaced with similar age differences. In other words, it is predominantly the pattern of acidity peaks that were matched between the two cores, rather than the individual peaks themselves. A similar approach was previously used to synchronize ice cores from Greenland and Antarctica by annual layer counting and linking of bipolar volcanic reference horizons (Svensson et al., 2013; now referenced in the text). In the manuscript, we have revised and extended the description of this approach, and for better illustration of the method, we have added to figure 9 (now figure 10) the age differences between the volcanic match-points in the two cores.

As the reviewer points out, a quantitative approach to identifying and matching volcanoes between the two cores would have been ideal, but a simple “over-the-threshold” technique would have identified many peaks of non-volcanic origin. Furthermore, no simple threshold method is able to account for e.g. changes in baseline and variability of the signal with depth as well as it is possible to do by eye. Even more importantly, a quantitative technique for selecting volcanic marker horizons to be matched to WAIS Divide should, as previously mentioned, not simply be based on the individual peaks, but combining this with some sort of pattern matching technique that could account for their relative age spacing, and the associated age uncertainties. To develop such a rigorous method is a significant undertaking, which we consider far beyond the scope of this work.

Instead, we have added to table 2 a measure for the average peak prominence in the RICE records corresponding to each of the volcanic match points. To account for changes in baseline and variability of the signals with depth (due to varying measurement quality as well as changes in signal with depth), smoothed versions of the four volcanic proxy records (acidity, nss-cond, nssS, ECM) were standardized using z-scores within a running 50-year window. The records were smoothed over a depth section

corresponding to 1/4 year to remove noise while amplifying the volcanic signal. The average value of the peak prominence in the four volcanic proxy records is provided in Table 2. However, we observed that in some cases, the mean value provided in table 2 was not the best indicator for the peak prominence. In some cases, the volcanic peaks were clearly observed in some proxy records, but not others, which significantly decreased the associated average significance level.

The majority of the match points are associated with peaks exceeding two standard deviations of the overall variability of the record. However, while the majority of the volcanic marker horizons are prominently observed in the RICE records, also some smaller peaks were deemed reliable match points, where these formed part of a matching sequence of volcanic events in the two cores.

The development of the non-sea-salt conductivity (nss-cond) may provide remedy in this context, but is not convincingly shown to record volcanic signals. For instance, Figure 9 shows three distinct peaks in nss-cond (around 162, 164 and 168 m RICE depth). The other match points, however, have little or no sign of a peak, including the Pleiades tephra horizon. There is an additional peak around 169 m not considered. Moreover, judging from Figure 9 the signals of H+ and ECM appear to perform equal or even better (less noise) in indicating peaks at the presumed volcanic markers - which would argue against the need to use nss-cond. Based on Figure 9, I am not convinced that the acidity signal provides more information than the nss-S signal, other than its higher depth resolution.

While the non-sea-salt conductivity record would not necessarily be sufficient for identification of volcanic marker horizons on its own, the record adds valuable information to the other data series. In order to obtain the best volcanic matching of the RICE record, we used the information in all four records: ECM, nssS (available down to 249m), H+, and non-sea-salt conductivity. This has been clarified in the manuscript. Not only do the various records contain complementary information, the existence of multiple data series also helps to identify variability caused by measurement errors in a single data series, as well as to retrieve volcanic match points in sections where other data series are missing (we note in table 2 the peaks that are not based on all 4 data series due to missing data).

With the high depth resolution of the non-sea-salt conductivity and H⁺-records, the combination of these two were particularly useful for distinguishing between measurement noise and acidic signal. However, the usefulness of the individual records varied with depth, as well as it depended on the individual volcanic horizon. For the deeper part, the nssS-record became significantly less useful as the much lower depth resolution became critical. During our revisions, we realized that the ECM record shown in the figure in the previous draft was not the ECM record, but a smoothed version of H⁺. This has now been corrected. The ECM record is generally very noisy, but some sections are better than others. This was primarily due to variability in the ice core quality, but variation between ECM operators was also a factor.

Regarding figure 10 (previously fig. 9):

For the Pleiades horizon: The identification of this match point was not based on chemical signals in the core, but was found by visual identification of a dusty layer in the core, later confirmed to be tephra. Indeed, the horizon cannot be observed in the CFA data for a very good reason: The section with tephra was removed before the CFA analysis, meaning that we do not have chemistry data for exactly this depth interval. We have made sure that this is now clear from the figure, which no-longer shows interpolated values across the missing data interval.

As the reviewer points out, two of the volcanic peaks are less prominent in the nss-conductivity record. We have changed the color of the two less prominent marker horizons mentioned by the reviewer (161m, 166.7m) to illustrate that in terms of peak height, these peaks are among the less significant peaks of all identified volcanic match points in the core, and they do not exceed a 2 σ threshold for peak significance.

Our reasoning behind nevertheless identifying them as volcanic horizons (and match points to WAIS Divide) is as follows:

At 161m, we observe a broad peak in the nssS-record, which we identify as very likely to be a volcanic horizon: At this depth, the layer thickness (~17cm) is sufficiently large that ~3 IC measurements of S exist per year. As the biologic S-component is a summer signal, an extreme biological influx event should not express itself as a series of successive data points with elevated sulfur values, also through winter, as it is present here. In the remaining records, there is a (smaller) peak in the H+ and nss-cond records, with e.g. the peak in the normalized nss-conductivity record reaching 1.8σ . Since further this peak is located at exactly the right spot according to the respective timescales and the surrounding match points, we believe that we can safely assume this to be a reliable match point.

Also at 166.7m, nss-cond is the record out of the four, which, after smoothing and normalization, has the largest peak (1.5σ). However, we would not have identified this as a reliable match point, had it not been surrounded by two very clear match points, and being located exactly at the right spot between them.

The above illustrates the importance of looking for patterns of volcanic peaks to obtain reliable match points, as well as the ability of non-sea-salt conductivity to record volcanic marker horizons, even if the peaks do not always exceed a 2σ threshold.

The “peak” around 169m mentioned by the reviewer is very likely an artifact from the calculation of the non-sea-salt conductivity, and caused by a slight discrepancy in the depth alignment of the calcium and conductivity records, this causing a “heart-beat” pattern: a very thin peak immediately followed by very low (here: negative) values. There were several similarly shaped “heartbeat” patterns in the same figure (e.g. at 161.5m, 164.5m, 167m) and even more of smaller size. We emphasize that only broad peaks in the nss-cond should be considered possible volcanic horizons. In the revised version of the figure, we now show a more smoothed version of the nss-conductivity record. The smoothing removes these heart-beat shaped patterns, and hopefully makes the broader peaks more apparent to the reader. As in the previous version of the figure, we also have colored the area under the graph in order to focus the attention of the reader to the broader peaks.

The authors are aware of potential pitfalls associated with nss-cond calculated as a secondary quantity, but do not quantify how much (or how little) the signal is affected by these problems. For example, this concerns potential false peaks produced by uncertainty in depth-alignment between Cond and Ca^{++} , as well as peaks through very low Ca^{++} .

As mentioned in the previous comment, an incorrect depth alignment of the conductivity and Ca^{2+} records gave rise to a very particular heart-beat pattern, which easily could be recognized. We further used several approaches to account for the various issues associated with the non-sea-salt conductivity being a secondary quantity: 1) We focused on the broader peaks as these are not affected by depth-scale issues, 2) We used smoothed versions of the conductivity and Ca^{2+} records before calculating the nss-conductivity, since this reduces the impact of depth-scale differences, and, finally but most importantly, 3) we always double-checked against a direct plot of the two records overlaying each other to identify whether peaks in non-sea-salt conductivity were caused by obvious errors in alignment or measurement issues. The conductivity-to-calcium excess is now also shown as a green area on the figures.

Indeed, often peaks in the conductivity-to-calcium excess could often much easier be recognized when comparing the two records directly. This is perhaps best illustrated in Figure S4, second panel from the top, where e.g. the Krakatau volcanic horizon is visible as a distinct peak in conductivity (grey) that is not present in the Ca^{2+} record (green). This peak cannot be explained by e.g. depth alignment issues or

different smoothing in the two records, which may account for many of the other smaller peaks in the derived non-sea-salt conductivity record.

Consequently, I believe the volcanic identification and matching needs to be expanded and clarified, ideally including: i) a quantitative approach to peak detection, e.g. by employing a local "peak-over-threshold" criterion, ii) a more convincing demonstration of the new volcanic proxy nss-cond, including addressing the pitfalls of a secondary quantity, and iii) showing a more extended version of Figure 9 as a side-by-side comparison between RICE and WAIS volcanic signals, also at depths not including the distinct tephra marker of Pleiades.

Replies to i) and ii) were provided above. Regarding iii) we now have added an extra figure to the supplementary showing the volcanic matching of the two cores for a deeper section. For this section, the marker horizons are significantly more sparsely located, making it harder to see the details of the various records. The nssS-record for RICE does not exist below 249m, and is therefore not shown.

Detailed comments:

Introduction: The companionship to the Lee et al. paper should be mentioned explicitly when stating the scope of this work.

This has been included.

P6 L37-38: " Some uncertain layers were counted as a year in the timescale, while others were not." This procedure remains unclear. As I am sure the authors are aware, a typical approach here is to count uncertain layers as 0.5 ± 0.5 years. Why was this procedure not adopted in this case? It is also not clear what uncertainty estimate was obtained and why this should be a 95% confidence interval.

Always increasing the timescale uncertainty by 1/2 year when encountering uncertain layers would give rise to an always-increasing uncertainty estimate with depth, which is not appropriate for timescales constrained by known-age marker horizons (as those present in the upper part of RICE).

Instead, our approach for estimating the uncertainty on the manually-layer counted part of the timescale was as follows: We identified the most likely set of layers, while any uncertainties in the layer identification (layers that possibly could be added or removed from the most likely set of annual layers, while still adhering to the age constraints) were reflected as an increase in the associated age uncertainty. The resulting age uncertainty is largest midway between two age constraints. We have revised the description of the process in the paper. We believe this to be a very conservative estimate of the uncertainty, roughly corresponding to a 95% confidence interval. We chose this approach as it produces an uncertainty estimate most similar to that obtained from StratiCounter (which is a 95% confidence interval), and we desired to keep the definition of the counting uncertainty along the core as similar as possible.

P8 L5-6: "The calcium and conductivity records frequently displayed multiple peaks per year, limiting their contribution to the annual layer interpretations."

This is another reason why it would be very important to see the performance of StratiCounter in such a case.

Sections of the calcium and conductivity records have been included in the new figure 6, along with the inferred annual layers from StratiCounter.

P8 L20-23: "Using ... the modelled density profile fits well the observed values". How were the parameters used here obtained, i.e. why these values selected? Also, from Figure S2 it can be seen that this statement is true only for the top 50 m. Below that depth there is a substantial misfit in the lower core - including depth of the firn-ice transition. This should at least be mentioned - I assume consequences of the misfit would be negligible if only an extrapolation of near-surface values was concerned.

The parameters used are observed values for accumulation rate, surface temperature, and initial snow density. This has now been clarified in the manuscript. Indeed, there is a small misfit between the model and the observations below 50m, but the top part fits well. It is unclear why there is this difference between modelled and observed densities, but as mentioned briefly in the supplementary (S3), it could potentially be due to the additional vertical strain present at divide locations.

Because of the misfit between model and observations, we have used the observed density values to correct the layer thickness for density changes with depth. Since we use the model only for correcting for the density in the very top part of the core, the misfit between modelled and observed densities in the deeper part should have no impact on our results.

P9 L15: "estimated using an ice-flow model to match the dated architecture of the Raymond stack" This is rather vague. What ice-flow model was used? Is this work done by the authors or the approach of Kingslake et al. (2014)? Please clarify.

This ambiguity in the text was also pointed out by reviewer #2, and we have provided a detailed answer there.

In short, we have used both 1D and 2D models, matching respectively the bump amplitude and the internal layering directly. This work will be presented in a paper by itself (which we are working on). For the present paper, we have added a comment that this is on-going work (see supplementary).

P9 L19-20: "a linear combination with divide-type velocities weighted by 0.7 and flank-type velocities weighted by 0.3."

Please state why these values were used. Was this an arbitrary selection? If so, would uncertainty in these values contribute to the uncertainty in thinning function? This approach remains unclear.

As requested by reviewer #2, we have rewritten the section on the ice-flow modelling to clarify our approach. We use a linear combination of flank and divide-like flow profiles to account for the migration of the ice divide, which causes the flow to become increasingly divide-like over time. The specific weights come from the relative magnitude of the Raymond arch at the ice core site: The amplitude of the Raymond Arch at the core site is approximately 70% of the peak amplitude, and we use this number to indicate the relative importance of the divide-like flow profile in the deeper part of the core.

Following the suggestions from reviewer 1, we have recalculated the uncertainty in the thinning function. It is now calculated based on the envelope of thinning functions obtained from 12 different scenarios, which includes the uncertainty in divide-migration over time, and how it has impacted the vertical velocity profile. The resulting uncertainties are in reasonable agreement with our previous estimates.

P9 L29-30: "Except for the uppermost part of the record, uncertainty in the thinning function dominates the total uncertainty, and only this factor will be considered here."

This is an important statement but is not supported by any evidence. Please explain.

Additional uncertainties could be caused by the density profile or misinterpretation of annual layers.

With regard to density: Except for the top 8m, we use measured densities, and the uncertainty associated with these should be minor. The extrapolation of densities to the surface is aided by the measurements of surface density in nearby snow pits. This, and the good agreement between modelled and measured densities in the top 50m, ensures that the density correction only causes minor uncertainty for the estimation of past accumulation rates.

Misinterpretation in annual layers may give rise to the annual accumulation for some years being significantly too high (e.g. twice as high if a layer is missing) or too low (e.g. half the actual amount, if there is a layer too many). However, due to the negligible bias of the timescale (as backed up by the volcanic matching to WAIS Divide), the uncertainty on average accumulation rates will be very small throughout the core. This argumentation has been added to the manuscript.

In the top part, the uncertainty in the thinning function is zero (no stain thinning has taken place), and hence the other two factors, while small, will dominate here. However, for the deeper part, it is a very good assumption to neglect the uncertainties of other factors than the thinning rate.

P9 L31 ff: This paragraph has some vague statements making it hard to fully comprehend. E.g. Was the near-surface uncertainty in density (it is only extrapolated) considered here? And: "(b) variation of the vertical velocity profile over time in ways not accounted for." E.g. I assume you are referring here to your change in weights of the linear combination?

The section only concerns the uncertainty associated with the thinning function, not the density correction. This section has been rewritten, and a section has been added to the supplementary, discussing the derivation of new estimates of the uncertainty on the accumulation rates.

P10 L3-4: "We suggest to interpret this uncertainty as a 95% (2σ) confidence interval." It is not clear why this needs to be exactly a 95% confidence level, or why this confinement to 95% is even needed.

We believe that our uncertainty bound is rather conservative, as it is calculated as the envelope of 12 scenarios, each of which represent (at least one) extreme parameter or scenario. As we wish to convey to the reader that this is a conservative estimate of the uncertainty, we have elected to keep the above sentence that we interpret the uncertainty as a 95% confidence interval.

P10 L13-14: "The CFA acidity record is driven primarily by the influx of non-sea-salt sulfur-containing compounds, as evident by its high resemblance to the IC non-sea-salt sulfate and ICP-MS non-sea-salt sulfur records in the top part of the core (Fig. 4)."

This may be true, but how can it be reconciled with the later statements about using acidity as a more reliable tracer of volcanic events, e.g. the statements about halide acids from regional volcanism? See comment for P19 L23 below.

Comparing the CFA acidity record with the non-sea-salt sulfur record, we observe more or less the same overall signal in the two records. However, at times there are peaks of excess acidity in the acidity record. We consider it likely that some of these peaks are caused by halogenic acids originating from regional volcanic eruptions. The two statements are therefore not contradictory. See also our reply to the last question, where we have provided some examples of distinct acidity peaks that are less prominent in the sulfur-record, although the remaining part of the records show fairly similar variability.

We note that we used all the available records for identifying volcanic eruptions in the RICE records. We do not as such consider the acidity record the most reliable tracer of volcanic events, but it was among the most useful records due to its high depth resolution.

P10 L28 and L33: Should be now Figure 9, not 8.

Corrected.

P13 L24: Please give a definition of how the conductivity-to-calcium excess was calculated.

The conductivity-to-calcium excess was calculated as follows:

$$\text{nss-cond} = \text{cond} - (a \cdot \text{Ca} + b),$$

with the coefficients a and b found from a linear fit for a running 2m window around the specific depth section. This definition has been added to the manuscript. The resulting record was subsequently smoothed in order to eliminate false peaks caused by slight differences in depth alignment between the two records.

P13 L27-28: "Nevertheless, peaks in the conductivity-to-calcium excess showed high consistency with peaks in total acidity, and it proved to be a reliable tracer for volcanic activity." Referring to main comment 2., this needs to be shown in more convincing detail. For instance, how does the excess signal look for the recent historical eruptions used in the paper, such as Krakatau?

We have added a figure to the supplementary showing the volcanic records (and the matching to WAIS Divide) in the top part of the record, including the Krakatau and Makian volcanic horizons. Both display a very distinct excess of conductivity relative to the calcium, which is especially visible when comparing the two records directly. The same peaks are visible in the acidity record.

P13 L36: The Kalteyer, 2015 reference is not accessible without a login from the University of Maine.

The reference has been removed.

P14 L44: "Fig 9a" should be Figure 10.

Corrected

P15 L40: "It has been suggested that this shift is due to other factors than temperature (Bertler et al., 2018),..."

Vague statement, please clarify what "other factors" are.

In Bertler et al, it is suggested that this change in isotope level may be related to changes in regional sea ice extent and atmospheric circulation. This has been added.

P16 L35-36: "Present accumulation rates show a distinct decrease on the downwind (western) side of the ice divide with a gradient of $\sim 5 \cdot 10^{-3}$ m w.e./km yr⁻¹, although muted around the summit area." Where does this data come from? Is there a missing citation?

Citation has been added.

P19, L23 ff. "The halide acids are highly soluble, and will be removed from the atmosphere relatively quickly during transport. Hence, they will contribute to increased ice acidity in ice cores located close to the eruption site, whereas only sulfate is deposited from distant volcanic eruptions. By focusing on acidity as volcanic tracer instead of sulfur, the RICE volcanic proxies may thus be more sensitive to regional volcanism than to larger far-field eruptions."

As pointed out above, if acidity is dominated by non-sea-salt sulfur as claimed earlier in the manuscript, how would additional, presumably volcanic acids, leave a detectable imprint? In other words, if the H+

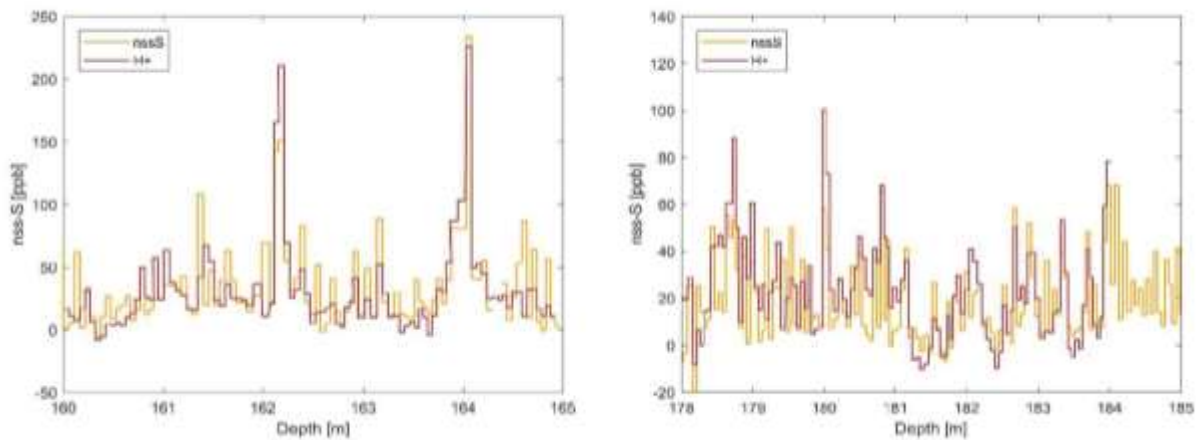
data shown in Figure 9 would be down-sampled to the depth-resolution of nss-S shown in the same Figure, would there be in fact a discernible difference between the two datasets, especially at the locations of the assumed eruptions? The reader is unable to evaluate this based on the presented data in Figure 9.

We have rewritten the section so that it becomes clear that while this is suggested from our preliminary investigations, we do not attempt to quantify the importance of the effect on the RICE records.

When comparing the acidity record, down-sampled to the same depth resolution as nssS, we observe a tendency towards a larger relative size of peaks in acidity for volcanic horizons that were not classified as originating from far-field eruptions. However, any further quantification is tricky due to: 1) changes in baseline with depth due to calibration issues, 2) the low resolution of the down-sampled records, and 3) a limited number of non-bipolar volcanic horizons for which both data sets are available.

Below is shown the nssS record and the acidity record down-sampled to the same depth resolution for two depth sections. We selected these two sections, as they both contained a volcanic horizon that could be matched to a non-bipolar volcanic horizon in the WAIS Divide ice core, i.e. the horizon was likely to represent a regional eruption. We would therefore expect the acidity peak for these eruptions to be relatively larger than the peak in nssS.

This is also what we observe: Comparing the two peaks at 164m (Samalas; bipolar) and 162m (not bipolar), the two peaks are of the same size in the acidity record, whereas the Samalas bipolar horizon is significantly larger in sulfate than the horizon at 162m. The second depth section contains only a single volcanic match-point horizon, namely at 180m. Compared to the overall range of variability in nssS and H⁺, there is also here an indication that the volcanic horizon has additional acidity compared to its sulfur content. We also observe that in general, the nssS and acidity show fairly similar (though not identical) variability throughout both sections.



1 A 2700-year annual timescale and accumulation history for an 2 ice core from Roosevelt Island, West Antarctica

3 Mai Winstrup^{1,*}, Paul Vallelonga¹, Helle A. Kjær¹, Tyler J. Fudge², James E. Lee³, Marie H.
4 Riis¹, Ross Edwards^{4,5}, Nancy A.N. Bertler^{6,7}, Thomas Blunier¹, Ed J. Brook³, Christo Buizert³,
5 Gabriela Ciobanu¹, Howard Conway², Dorthe Dahl-Jensen¹, Aja Ellis⁴, B. Daniel
6 Emanuelsson^{6,7}, Richard C.A. Hindmarsh⁸, Elizabeth D. Keller⁷, Andrei V. Kurbatov⁹, Paul A.
7 Mayewski⁹, Peter D. Neff¹⁰, Rebecca L. Pyne⁷, Marius F. Simonsen¹, Anders Svensson¹,
8 Andrea Tuohy^{6,7}, Edwin D. Waddington², Sarah Wheatley⁹

9 1: Centre for Ice and Climate, Niels Bohr Institute, University of Copenhagen, Copenhagen,
10 Denmark

11 2: Earth and Space Sciences, University of Washington, Seattle, WA, USA

12 3: College of Earth, Ocean, and Atmospheric Sciences, Oregon State University, Corvallis, OR,
13 USA

14 4: Physics and Astronomy, Curtin University, Perth, Western Australia, Australia

15 5: Department of Civil and Environmental Engineering, University of Wisconsin-Madison,
16 Madison, USA

17 6: Antarctic Research Centre, Victoria University of Wellington, Wellington, New Zealand

18 7: GNS Science, Lower Hutt, New Zealand

19 8: British Antarctic Survey, Cambridge, UK

20 9: Climate Change Institute, University of Maine, Orono, Maine, USA

21 10: Earth and Environmental Sciences, University of Rochester, Rochester, NY, USA

22 *: Now at: Danish Meteorological Institute, Copenhagen, Denmark

23 Correspondance to: Mai Winstrup (mai@nbi.ku.dk)

24 Abstract

25 We present a 2700-year annually-resolved chronology and snow accumulation history for the
26 Roosevelt Island Climate Evolution (RICE) ice core, Ross Ice Shelf, West Antarctica. [The core
27 adds information on past accumulation changes in an otherwise poorly constrained sector of
28 Antarctica.](#)

29 The timescale was constructed by identifying annual cycles in high-resolution impurity records,
30 and it constitutes the top part of the Roosevelt Island Ice Core Chronology 2017 (RICE17).
31 ~~The timescale was~~ Validation ~~ed~~ by volcanic and methane matching to the WD2014
32 chronology from the WAIS Divide ice core ~~shows that, and the~~ two timescales are in excellent
33 agreement. [In a companion paper, gas matching to WAIS Divide is used to extend the timescale
34 for the deeper part of the core where annual layers cannot be identified.](#)

35 [Based on the annually-resolved timescale, we produced a record of past snow accumulation at
36 Roosevelt Island.](#)

37 The ~~RICE-snow~~ accumulation history shows that Roosevelt Island experienced slightly
38 increasing accumulation rates between 700 BCE and 1300 CE, with an average accumulation
39 of 0.25 ± 0.02 m water equivalent (w.e.) per year. Since 1300 CE, trends in the accumulation
40 rate have been consistently negative, with an acceleration in the rate of decline after the mid-
41 17th century. The current accumulation rate at Roosevelt Island is 0.2104 ± 0.002 m w.e. y^{-1}

42 (average since 1965 CE, $\pm 2\sigma$), and rapidly declining with a trend corresponding to 0.8 mm yr⁻².
43 The decline observed since the mid-1960s is 8 times faster than the long-term decreasing
44 trend taking place over the previous centuries, with decadal mean accumulation rates
45 consistently being below average.

46 Previous research has shown a strong link between Roosevelt Island accumulation rates and the
47 location and intensity of the Amundsen Sea Low (ASL), with significant impact on regional
48 sea ice extent. The decrease in accumulation rates at Roosevelt Island may therefore be
49 explained in terms of a recent strengthening of the ASL and expansion of sea ice in the Eastern
50 Ross Sea. The start of the rapid decrease in RICE accumulation rates observed in 1965 CE may
51 thus mark the onset of significant increases in regional sea ice extent.

52 **1. Introduction**

53 Accurate timescales are fundamental for reliable interpretation of paleoclimate archives,
54 including ice cores. Ice-core chronologies can be produced in a variety of ways. Where annual
55 snow deposition is sufficiently high and reasonably regular throughout the year, seasonal
56 variations in site temperature and atmospheric impurity deposition lead to annual cycles in the
57 ice-core water isotope and impurity records (Dansgaard, 1964; Hammer et al., 1978). By
58 identifying and counting the annual cycles, an annual-layer-counted ice-core timescale can be
59 produced (Sigl et al., 2016; Steig et al., 2005; Svensson et al., 2008). This technique is
60 commonly employed for producing ice-core timescales at sites with moderate to high snow
61 accumulation, including coastal Antarctica. Annual-layer-counted ice-core timescales have
62 traditionally been obtained by manual counting, but this task can now be performed using
63 machine-learning algorithms for pattern recognition (Winstrup et al., 2012).

64 Where possible, identification of annual layers allows the development of a high-resolution ice-
65 core chronology, but unless constrained by other data, the uncertainty of such a timescale will
66 increase with depth, as the number of uncertain layers accumulate to produce some age
67 uncertainty (Andersen et al., 2006; Rasmussen et al., 2006). Marker horizons found in the ice-
68 core records can be used to evaluate the accuracy of a layer-counted timescale, or, alternatively,
69 to constrain the timescale. Such marker horizons carry evidence of events of global or regional
70 nature, and may be; (a) layers of enhanced radioactivity resulting from nuclear bomb tests
71 (Arienzo et al., 2016); (b) sulfuric acids (Hammer, 1980) and/or tephra (Abbott et al., 2012)
72 from volcanic eruptions; or (c) enhanced flux of cosmogenic radionuclides caused by changes
73 in solar activity, reduction of the Earth's magnetic field, or cosmic events (Muscheler et al.,
74 2014; Raisbeck et al., 2017; Sigl et al., 2015).

75 Ice cores can also be stratigraphically matched using records of past atmospheric composition
76 from trapped air in the ice (Blunier, 2001; Blunier et al., 1998; EPICA Community Members,
77 2006). Variations in atmospheric composition are globally synchronous. Accounting for the
78 time required to sequester the air into the ice, the ice-core gas records can be used also for
79 stratigraphic matching of records measured on the ice matrix. Even during periods of stable
80 climate, the atmospheric composition displays multi-decadal fluctuations (Bender et al., 1994;
81 Mitchell et al., 2011, 2013) allowing synchronization on sub-centennial timescales.

82 Annually-resolved ice-core chronologies provide long-term reconstructions of annual snow
83 accumulation (Alley et al., 1993; Dahl-Jensen et al., 1993): Annual layer thicknesses can be
84 converted to past accumulation rates by applying corrections due to density changes during the
85 transformation from snow to ice (Herron and Langway, 1980), and thinning of annual layers
86 caused by ice flow (Nye, 1963). Reconstructions of past accumulation rates are important for
87 improving our understanding of the natural fluctuations in snow accumulation and their climate

88 drivers. Such knowledge is essential to accurately evaluate the current and future surface mass
89 balance of glaciers and ice sheets, a critical and currently under-constrained factor in sea level
90 assessments (Shepherd et al., 2012).

91 Here we present an ice-core chronology ([RICE17](#)) and accumulation history for the last 2,700
92 years from Roosevelt Island, an ice rise located in the Eastern Ross Embayment, Antarctica
93 (Fig. 1). The ice core was extracted as part of the Roosevelt Island Climate Evolution (RICE)
94 project (2010-2014) (Bertler et al., 2018). RICE forms a contribution to the Antarctica2k
95 network (Stenni et al., 2017; Thomas et al., 2017), which seeks to produce Antarctica-wide ice-
96 core reconstructions of temperature and snow accumulation for the past 2000 years. [The](#)
97 [chronology presented here was produced by annual-layer counting. In a companion paper](#) (Lee
98 et al., 2018), [we extend the timescale to cover the deeper core by gas matching to the WAIS](#)
99 [Divide ice core on the WD2014 chronology](#) (Lee et al., 2018). (Buizert et al., 2015; Sigl et al.,
100 2016).

101 ECMWF ERA-Interim (ERAi) reanalysis fields (Dee et al., 2011) indicate that precipitation at
102 Roosevelt Island is strongly influenced by the Amundsen Sea Low (ASL) and associated
103 ridging (Raphael et al., 2016), and anti-correlated with precipitation in Ellsworth Land and the
104 Antarctic Peninsula (Bertler et al., 2018; Emanuelsson et al., 2018; Hosking et al., 2013). These
105 differences emphasize the need for high spatial and temporal coverage when reconstructing
106 regional mass balance patterns. With few other ice cores from the Ross Sea region, the RICE
107 accumulation history adds information on past changes in mass balance from an otherwise
108 poorly-constrained sector of the Antarctic continent.

Field Code Changed

109 2. Site characteristics

110 Roosevelt Island is located within the eastern part of the Ross Ice Shelf (Fig. 1), from which it
111 protrudes as an independent ice dome that is grounded 214 meters below sea level. Snow
112 accumulates locally on the ice dome, with ice originating from the Siple Coast ice streams
113 flowing around the island in the Ross Ice Shelf. Geophysical and glaciological surveys across
114 Roosevelt Island in the 1960s established ice thickness, surface topography, surface velocity
115 and accumulation rate (Bentley and Giovinetto, 1962; Clapp, 1965; Jiracek, 1967). The island
116 was revisited during 1974-75 as part of the Ross Ice Shelf Project. During this project, shallow
117 cores (up to 70m) were collected across the ice shelf, including two firn cores from Roosevelt
118 Island summit (Clausen et al., 1979). The shortest (11 m) firn core from near the summit was
119 measured for water isotopes and total β -activity in high resolution; we here refer to it as RID-
120 75 (Table 1). Results from the shallow cores show that seasonal signals of stable isotopes and
121 ionic chemistry are well preserved in the ice (Clausen et al., 1979; Herron and Langway, 1979;
122 Langway et al., 1974).

123 Ice-penetrating radar surveys of Roosevelt Island that took place in 1997 revealed a smoothly
124 varying internal stratigraphy of isochronal reflectors (Conway et al., 1999). There was no
125 evidence of disturbed internal layering that would indicate high strain rates or buried crevasses,
126 suggesting the summit of the island to be a good place for an ice core. Of special interest was a
127 distinctive arching pattern of the internal layers beneath the divide. This pattern has implications
128 for the ice history, since isochronal layers arch upward beneath divides that are stable and frozen
129 at the bed (Raymond, 1983). Analyses of the geometry of the [internal layering is so-called](#)
130 [Raymond stack](#) indicate that the current divide-type ice-flow regime started about 3000 years
131 ago (Conway et al., 1999; Martín et al., 2006), and thus has been in existence throughout the
132 time period investigated in this paper. [At mid-depths, the Raymond arches are offset from the](#)
133 [current topographic summit by ~500m towards north east, indicating a slight migration of the](#)
134 [ice divide in past centuries.](#) Combined with a recently-measured vertical ice velocity profiles

135 ~~across~~ the ice divide (Kingslake et al., 2014), the stability of the ice flow regime at Roosevelt
136 Island facilitates interpretation of past accumulation rates from annual layers in the RICE ice
137 core.

138 The RICE deep ice core was drilled at the summit of Roosevelt Island (79.364S, 161.706W,
139 550 m above sea level (Bertler et al., 2018)), and less than 1 km from the old RID-75 shallow
140 core. It was drilled in austral summers of 2011/12 and 2012/13. During the first season, the core
141 was dry-drilled down to 130 m, and then the borehole was cased. An Estisol-240/Coasol drilling
142 fluid mixture was used to maintain core quality during the second drilling season. The ice
143 thickness is 764.6 m. The upper 344 m of the core spans the past 2700 years; the period for
144 which an annual-layer-counted timescale can be constructed. In addition to the deep core,
145 several shallow cores were drilled in the vicinity. During the 2012/13 field season, a 20 m firn
146 core (RICE-12/13-B) was drilled near the main core, and it was used to extend the records up
147 to the 2012/13 snow surface. Table 1 provides an overview of the relevant firn and ice cores
148 collected at Roosevelt Island. An automated weather station near the RICE drill site recorded
149 mean annual temperatures of -23.5°C over the duration of the RICE project (2010-2014), and
150 an average snow accumulation of approximately 0.20 m w.e. yr⁻¹ (Bertler et al., 2018).

151 **Methods**

152 **3. Ice core processing and impurity analysis**

153 The RICE ice cores were processed and analyzed at the GNS Science National Ice Core Facility
154 in Lower Hutt, New Zealand. The cores were cut longitudinally to produce a 15x35 mm
155 triangular piece for water isotope analysis and two 35x35 mm square sticks for continuous flow
156 analysis (CFA) (Fig. 2). The second CFA piece was for use in case the core quality of the
157 primary piece was compromised, or for repeat measurements to test measurement accuracy and
158 system stability.

159 In parallel with ice core cutting and processing, CFA and electrical conductivity measurements
160 (ECM₂ (Hammer, 1980)) were carried out. ECM (Hammer, 1980) was measured using a low-
161 power hand-held instrument from Icefield Instruments Inc. directly on the ice-core surfaces
162 after the initial cutting of the core. In 2012, the uppermost section (8.57-40 m) of the RICE
163 main core was processed and analyzed using the GNS Science melter system, with continuous
164 measurements of stable water isotopes (δD , $\delta^{18}O$) and black carbon, and discrete sampling of
165 major ion and trace element concentrations. The following year, this set-up was replaced by an
166 expanded version of the Copenhagen CFA system (Bigler et al., 2011), providing high-
167 resolution continuous measurements of liquid conductivity, calcium (Ca²⁺), insoluble dust
168 particles, acidity (H⁺), and black carbon (BC), as well as stable water isotopes (δD , $\delta^{18}O$) and
169 methane gas concentrations (Table 1). The RICE-12/13-B firn core was analyzed using this
170 system. Next, the RICE main core was melted and analyzed from 40 m to 475 m, at which depth
171 the ice brittle zone was reached. Subsequent repeat measurements of the top section (8.57-40
172 m) of the main core were made using the second, parallel CFA stick.

173 Primary adaptations to the Copenhagen CFA system involved: 1) Depth assignment via a digital
174 encoder using a 1-second sampling rate (Keller et al., 2018); 2) Continuous analysis of stable
175 water isotopes ($\delta^{18}O$, δD) using a Los Gatos Research (LGR) analyzer (Emanuelsson et al.,
176 2015); 3) Black carbon analysis by a Single Particle Soot Photometer (Droplet Measurement
177 Technologies, Boulder, CO; DMT SP2) following the method reported by McConnell et al.
178 (2007); 4) Acidity measurements based on direct registration of H⁺ concentrations using an
179 optical dye method (Kjær et al., 2016); 5) Continuous methane concentration analysis using a
180 Picarro Cavity Ring-Down Spectroscopy (CRDS) instrument (Stowasser et al., 2012); and 6)

181 Inclusion of three fraction collectors for discrete sample analyses by, respectively, ion
182 chromatography (IC), Inductively-Coupled Plasma Mass Spectrometry (ICP-MS), including
183 measurements of ^{239}Pu using an ICP-SFMS technique (Gabrieli et al., 2011), and measurements
184 of stable water isotopes on the LGR. Figure 3 shows a diagram of the CFA system set-up.

185 The ice was melted at a rate of 3 cm min^{-1} , producing approximately 16.8 mL contamination-
186 free water and gas mixture per minute of melting. Air bubbles were separated in a debubbler,
187 dried, and sent to the Picarro CRDS instrument for methane analysis. Each minute, 5 mL
188 meltwater was directed to each of two fraction collectors (IC and ICP-MS aliquots) and 1.1 mL
189 was used for continuous measurements of water isotopes (0.05 mL) and black carbon (1.05 mL)
190 by the LGR and DMT SP2 instruments. The remaining 1.8 mL was sent to flow-through liquid
191 conductivity and insoluble particle analyzers (Bigler et al., 2011), and then split for continuous
192 analysis of soluble calcium (Traversi et al., 2007) and acidity (Kjær et al., 2016). A third
193 fraction collector was used to collect discrete samples for water isotopes from the melt-head
194 overflow lines originating from the outer core section, these being used for quality assurance
195 of the continuous measurements.

196 On average, 20 metres of ice were melted during a 24-hour period, including measurements,
197 calibrations and routine maintenance. Calibrations for water isotopes, calcium, acidity and
198 black carbon were carried out before and after each melting run, which comprised the
199 continuous analysis of $3\times 1\text{ m}$ long ice rods. Calibrations for methane, based on standard gases
200 with methane concentrations corresponding to glacial and preindustrial Holocene levels, were
201 carried out twice daily. Core breaks and/or contamination in the system caused some sections
202 of missing data. The percentage of affected core varied between chemistry species, ranging
203 from $<1\%$ (BC) to 17% (H^+) (see supplementary Table S1), the majority being small sections
204 of missing data that did not severely impact annual layer interpretation.

205 The CFA chemistry records were very densely sampled (1 data point per mm). Mixing in the
206 tubing as the meltwater sample travelled from melt head to the analytical systems caused
207 individual measurements to be correlated, and hence the effective depth resolution of the system
208 was significantly less than the sampling resolution. This was ~~particularly especially-important~~
209 ~~the case~~ for the RICE CFA set-up owing to the relatively small fraction of total meltwater
210 directed to the continuous measurement systems. Following the technique used in Bigler et al.
211 (2011), the effective depth resolution for the CFA measurements was estimated to range from
212 0.8 cm (conductivity) to 2.5 cm (Ca^{2+}) (Table S1).

213 **4. Constructing the Roosevelt Island Ice Core Chronology,** 214 **RICE17, for the last 2700 years**

215 The Roosevelt Island Ice Core Chronology 2017, RICE17, was constructed using multiple
216 approaches, as necessitated by changing properties and availability of data with depth. ~~Here we~~
217 ~~This section~~ describes the methodology used to construct the most recent 2700 years of
218 RICE17, the period for which annual layer identification was feasible. For the deeper part of
219 the core, RICE17 was constructed by gas matching to the WAIS Divide ice core on the WD2014
220 chronology, as reported in Lee et al. (2018).

221 **4.1. Overview of the annual-layer counting strategy**

222 The uppermost section (0–42.34 m) of the core was dated by manual identification of annual
223 cycles in records of water isotopes and chemical impurities from the RICE main core as well
224 as the RICE-12/13-B shallow core. For this most recent period, several distinct marker horizons
225 from well-known historical events were used to constrain the chronology (section 4.2).

226 Below 42.34m (1885 CE), the timescale was augmented using the *StratiCounter* layer-counting
227 algorithm (Winstrup, 2016; Winstrup et al., 2012) applied to multiple CFA impurity records
228 from the RICE main core (section 4.3). A previously-dated tephra layer at 165 m (Pleiades;
229 1251.6±2 CE according to WD2014) was used to optimize the algorithm settings, but other than
230 that, RICE17 is a fully independent layer-counted ice-core chronology.

231 The layer-counted part of RICE17 stops at 343.72 m (700 BCE). At this depth, the annual layers
232 ~~became~~ ~~are~~ too thin (<6 cm, i.e. less than 8 independent data points/year in the best resolved
233 records) for reliable layer identification in data produced by the RICE CFA set-up. ~~The~~
234 ~~timescale was~~ ~~extended back to 83,000 years before present~~ ~~the RICE17 timescale further~~
235 ~~back, the layer-counted timescale was combined with~~ using the gas-derived timescale, which
236 covers the entire core with lower resolution (Lee et al., 2018). Excellent agreement (±3 years)
237 between the layer-counted timescale and the independent gas-derived age at 343.7m allows us
238 to produce the combined Roosevelt Island Ice Core Chronology 2017, RICE17, by joining the
239 two without any further adjustments.

240 **4.2. Manual layer interpretation with historical constraints (0 - 42.34 m;** 241 **2012 - 1885 CE)**

242 The top 42.34 m of the RICE17 chronology was obtained by manually counting annual layers
243 in the combined set of discretely-measured IC and ICP-MS data, where available, as well as the
244 continuous water isotope and chemistry records produced by the RICE CFA system. The RICE
245 main core starts at 8.65 m depth, so the top part of the timescale is based exclusively on the
246 RICE-12/13-B shallow core. At 12.5 m, both cores display a distinct peak in their isotope
247 profiles, showing that they can be spliced directly without need for any depth adjustments.
248 Layer marks for the top 12.5 m were placed according to the RICE-12/13-B shallow core; lower
249 layer marks refer to the main core. In the overlap section (8.65-19.55m), we used the combined
250 data set from both cores to reduce the risk of timescale errors caused by core breaks or bad data
251 sections.

252 Layer identification in this section of the core relied predominantly on annual signals in non-
253 sea-salt sulfate (nss-SO₄²⁻), acidity (H⁺) and iodine (I), as these records displayed the most
254 consistent annual signals (Fig. 4). Extreme sea-salt influx events occasionally caused large
255 sulfate peaks, necessitating the removal of the sea-salt sulfate fraction before layer
256 identification. For the top 20 m, the water isotope records also significantly strengthened the
257 annual layer interpretations. Smoothing through diffusion of water molecules in the firn,
258 however, ~~caused~~ ~~es-~~ ~~t-~~ the annual signal in the water isotope records to diminish with depth,
259 resulting in a loss of annual signals below 20 m.

260 Summers could be identified as periods with high stable water isotope ratios, high
261 concentrations of nss-SO₄²⁻ and associated acidity [originating from phytoplankton activity in
262 the surrounding ocean during summer (Legrand et al., 1991; Udisti et al., 1998)], and low iodine
263 concentrations [due to summertime photolysis of iodine in the snowpack (Frieß et al., 2010;
264 Spolaor et al., 2014)]. Layer marks were placed according to the depths of concurrent summer
265 peaks in water isotope ratios, nss-SO₄²⁻ concentrations, and acidity levels, and assigned a
266 nominal date of January 1st.

267 The uppermost 42.34 m of the RICE17 chronology was tied to several distinctly identifiable
268 marker horizons found in the ice-core records relating to well-known historical events (sections
269 4.2.1-4.2.3; Table 2). ~~The timescale was obtained by identifying the most likely set of annual~~
270 ~~layers, while accounting for age constraints from marker horizons (Fig. 4).~~ We conservatively
271 estimated the age uncertainty of the marker horizons to be ±1 year, thereby allowing for some
272 uncertainty in timing of deposition of e.g. volcanic material. ~~We further kept track of uncertain~~

273 layers (i.e. layers that possibly could be added or removed from the most likely set of layers,
274 while still adhering to the age constraints), thereby producing an uncertainty estimate for the
275 timescale. A confidence interval was assigned to the timescale by classifying layers as certain
276 or uncertain (Fig. 4), while accounting for age constraints from marker horizons. We
277 conservatively estimated the age uncertainty of the marker horizons to be ± 1 year, thereby
278 allowing for some uncertainty in timing of deposition of e.g. volcanic material. We interpret it
279 as the 95% confidence interval of the age at a given depth, similar to that obtained from
280 automated layer identification deeper in the core (section 4.3). Some uncertain layers were
281 counted as a year in the timescale, while others were not.

~~4.2.1. In this way, a most likely timescale was constructed along with an
uncertainty estimate, which we interpret as the 95% confidence interval of
the age at a given depth, similar to that obtained from automated layer
identification deeper in the core (section 4.3).~~

4.2.2.4.2.1. The 1974/75 snow surface

287 The uppermost age constraint was established by successfully matching the RICE water isotope
288 profile to that from the RID-75 firn core (Fig. 5). Drilled in austral summer 1974/75, the snow
289 surface in RID-75 provided the first tie-point for the RICE17 chronology at a depth of 14.62m
290 (Table 2).

4.2.3.4.2.2. Nuclear bomb peaks

292 High-resolution ^{239}Pu measurements on the upper part of the RICE core show a significant rise
293 in plutonium levels, starting from very low background levels at 22m and reaching peak values
294 at 21.6m. This increase can be attributed to atmospheric nuclear bomb testing during the Castle
295 Bravo Operation, Marshall Islands, in March 1954, which globally caused large amounts of
296 nuclear fallout over the following year (see e.g. Arienzo et al., 2016).

297 Total specific β -activity levels in the RID-75 core show the same evolution (Clausen et al.,
298 1979), confirming both the isotopic matching between the two cores, and the age attribution of
299 this event (Fig. 5). The abrupt increase in ^{239}Pu -fallout at 22m was used as age constraint for
300 the RICE17 chronology (Table 2). Subsequent peaks in the ^{239}Pu and β -activity records can be
301 attributed to successive nuclear tests and subsequent test ban treaties (Table 2). These changes
302 were much less distinct, and were therefore not used during development of the timescale.

4.2.4.4.2.3. Recent volcanic eruptions

304 A couple of volcanic horizons in RICE during this most recent part could be related to well-
305 known volcanic eruptions. Rhyolitic tephra located between 18.1-18.2m was found to have a
306 similar geochemical composition to a tephra layer found in the WAIS Divide core deposited
307 late 1964 CE (Wheatley and Kurbatov, 2017). The tephra likely originates from Raoul Island,
308 New Zealand, which erupted from November 1964 to April 1965. This is consistent with the
309 RICE17 chronology, according to which the tephra is located in early 1965 CE (Table 2).

310 Only two volcanic eruptions could be unambiguously identified in the acidity records over this
311 period; the historical eruptions of Santa Maria (1902 CE; 37.45m) and Krakatau (1883 CE;
312 42.34m) (Table 2). These two horizons were used to constrain the deeper part of the manually-
313 counted interval of RICE17, which terminates at the Krakatau acidity peak. Deposition age of
314 volcanic material for these events was assumed identical to those observed in the WAIS Divide
315 ice core (Sigl et al., 2013). Imprints from other large volcanic eruptions taking place during
316 recent historical time, such as Agung and Pinatubo, did not manifest themselves sufficiently in
317 the RICE records to be confidently identified.

4.3. Automated annual layer identification (42.34 - 343.7 m; 1885 CE - 700 BCE)

For the section 42.34-343.7 m (1885 CE - 700 BCE), the RICE17 annual layer-counted timescale was produced using the StratiCounter algorithm (Winstrup et al., 2012), extended to interpret the annual signal based on multiple chemistry series in parallel (Winstrup, 2016).

StratiCounter is a Bayesian algorithm built on machine-learning methods for pattern recognition, using a Hidden Markov Model (HMM) framework (Rabiner, 1989; Yu, 2010). StratiCounter computes the most likely timescale and the associated uncertainty by identifying annual layers in overlapping data batches stepwise down the ice core. For each batch, the layering is inferred by combining prior information on layer appearance with the observed data, thereby obtaining a posteriori probability distributions for the age at a given depth. The output of StratiCounter is the most likely annual timescale, along with a 95% confidence interval for the age as function of depth. The confidence interval assumes the timescale errors to be unbiased, implying that uncertainties in layer identification partly cancel out over longer distances. Previous research has documented the skill of StratiCounter to produce accurate and unbiased layer-counted ice-core timescales (e.g. Sigl et al., 2015; Winstrup, 2016).

StratiCounter was applied to the full suite of CFA records: black carbon, acidity, insoluble dust particles (42.3-129m), calcium, and conductivity. See ~~sSupplementary~~ S2 for the specifics of the algorithm set-up. Figure 6 shows three depth sections of CFA data and resulting layer counts. Annual cycles in the high-resolution black carbon (BC) record became more distinct prior to 1900 CE, and it was one of the most reliable annual proxies in the core (~~section 6~~). As observed in the topmost part of the core, acidity also displayed an ~~distinct~~ annual signal, although the ~~relatively lower~~ effective depth resolution of the acidity record (Table S1) made it ~~much~~ less useful with depth. The calcium and conductivity records frequently displayed multiple peaks per year, but contained complementary information to the other proxies, and hence were also useful for layer identification (Fig. 6). From 0 to 129 m, an irregular annual signal was also observed in the insoluble particle record, but data below 129 m was corrupted by the presence of drill fluid in the CFA system, which forced us to exclude the deeper part of this record. The discretely-sampled ICP-MS data records did not have sufficient resolution to resolve annual layers.

Decreasing layer thicknesses caused the annual signal in the impurity records to become increasingly difficult to identify with depth, and the layer-counted timescale stops at 343m (700 BCE).

5. Reconstructing past accumulation rates

The accumulation rate history at Roosevelt Island can be inferred from depth profiles of annual-layer thicknesses in the RICE core, when corrected for firn densification and thinning of layers due to ice flow.

5.1. Changes in density with depth

Bag-mean densities were measured on the main RICE core for the interval 8-130 m, at which depth ice densities were reached (see ~~sSupplementary~~ S3). A steady-state Herron-Langway density model (Herron and Langway, 1980) ~~fitted to the measurements~~ was used to extend the density profile to the surface. Using observed values for an initial snow density of (410 kg m⁻³), a surface temperature of (-23.5°C), and an accumulation rate of (0.22 m w.e yr⁻¹), the

362 modelled density profile fits well the observed values, especially for the top 50m (Fig. S2-1). At
363 8 m depth, the model agrees with the measured values, providing a smooth transition between
364 observed and modelled densities.

365 **5.2. Thinning of annual layers due to ice flow**

366 To obtain past accumulation rates, the annual layer thickness profile must be corrected for the
367 amount of vertical strain experienced by the ice. This correction factor can be represented by a
368 thinning function, which informs on the cumulative effects of ice flow on the thickness of an
369 ice layer after since it was deposited at the surface (this being the ice equivalent accumulation
370 rate at that time). The observed layer thickness relative to its initial thickness as a function of
371 depth, i.e. the “thinning function”, depends on the history of vertical strain at the core site. The
372 vertical strain rates can vary significantly over short distances near ice divides, with near-
373 surface ice flow being more compressive at the divide than at the flanks (Raymond, 1983). As
374 a result, the divide flow causes an upward arch in the internal layers beneath stable ice divides.
375 This is termed a Raymond Arch, and one is present beneath the Roosevelt Island ice divide
376 (Fig. 7c; Conway et al., 1999). The vertical strain pattern was measured across Roosevelt Island
377 (Kingslake et al., 2014) using repeat measurements of phase sensitive radar (pRES). These
378 measurements show significant spatial variation in the vertical velocity pattern and provide
379 important constraints for developing the RICE thinning function.

380 The RICE ice core was drilled at the topographic summit of Roosevelt Island. The shallowest
381 layers in the Raymond Arch peak below the current summit, but by mid-depth, the maximum
382 bump amplitude of the arches is offset by approximately 500 m towards east (Figure 7c).
383 Following Nereson and Waddington (2002), we interpret this slant in Raymond Arch position
384 as a slight migration of the Roosevelt Island ice divide during recent centuries, with the divide
385 previously being located 500 m east of its present position. The ice core intersects the Raymond
386 Arch at mid-depths (~120 m; ~1500 CE) at about 70% of the maximum arch amplitude. Thus
387 it has experienced a transitional flow regime, i.e. a mixture between pure divide flow and flank
388 flow, for much of the past 2700 years. We consider a recent migration of the ice divide towards
389 its present position to be the most likely scenario, with ice flow at the core site becoming
390 increasingly divide-like over recent centuries. For this scenario, we prescribe the following
391 history of divide migration history: Prior to 500 years before 2013 CE, the divide was located
392 500 m east of its present position. Since then, the divide migrated westward, arriving at its
393 present position 250 years ago. During the migration period, the ice flow regime linearly
394 transitioned to full divide flow, and subsequently remained as full divide flow until present. An
395 alternative, although less likely, scenario is that the location of maximum divide-flow has
396 always been offset from the topographic summit, in which case the ice in the core has
397 experienced transitional flow throughout the entire period. The uncertainty on the thinning
398 function associated with the divide history is explained in detail in the supplement (S4).

399 We used a one-dimensional transient ice-flow model with annual time steps to integrate the
400 vertical strain experienced by an ice layer, and thereby track the cumulative layer thinning as
401 function of time and depth. At each time step, the full-depth vertical velocity profile was found
402 by scaling the shape of the vertical profile (as discussed below) with the surface velocity: The
403 vertical surface velocity was determined as the sum of the time-varying accumulation rate and
404 the rate of change in ice-sheet thickness. The ice-sheet thickness change was prescribed, and
405 assumed constant in time. Model iterations were run to get an accumulation history consistent
406 with the cumulative thinning computed by the model.

407 The shape of the vertical velocity profile was found by fitting an ice-flow parameterization
408 (Lliboutry, 1979) to the measured englacial velocities (Kingslake et al., 2014) corresponding to

409 divide flow and flank flow, respectively (Fig. 7a). Details are given in the Supplementary S4.
410 The present vertical velocity profile was constrained to match within uncertainty the current
411 vertical velocity at the surface. During the period of transitional flow, the shape of the vertical
412 velocity profile was taken as a linear combination of the velocity profiles for divide and flank
413 flow, following Nereson and Waddington (2002). We used the relative amplitude of the
414 Raymond Arch as indicator for the importance of the two flow regimes, and during the early
415 period of transitional flow, the vertical velocity profile was weighted as 70% divide-type and
416 30% flank-type flow.

417 ~~A thinning function appropriate for RICE was produced using vertical velocity profiles~~
418 ~~obtained by fitting a simple ice flow model (Lliboutry, 1979) to englacial velocities deduced~~
419 ~~from repeat radar measurements (Kingslake et al., 2014), while (a) constraining the model~~
420 ~~parameters to match the present-day accumulation rate and ice sheet thinning, and (b)~~
421 ~~accounting for velocity changes caused by the shift in position of the ice divide at Roosevelt~~
422 ~~Island within the past centuries.~~

423 ~~Near-surface vertical strain rates are more compressive near ice divides than on the flanks.~~
424 ~~Hence, due to migration of the ice divide at Roosevelt Island, ice recovered from different~~
425 ~~depths in the RICE core has experienced different regimes of vertical strain. Informed by the~~
426 ~~architecture of the Raymond stack (Fig. 6e), we assumed the following divide migration~~
427 ~~history: Until 500 years before ice core drilling (1512 CE), the divide was located 500 m east~~
428 ~~of the present position, as indicated by the position of the deeper Raymond arches. Since 500~~
429 ~~years ago, the divide migrated westward, arriving at its present position by 1762 CE (250 years~~
430 ~~ago).~~

431 ~~Radar measurements of near-surface vertical strain rates (Fig. 6b in Kingslake et al. 2014) show~~
432 ~~that the transition from divide to flank type flow at Roosevelt Island occurs over a distance of~~
433 ~~~900 m. For the older part of the ice core (prior to 1512 CE; ice originating 500 m east of the~~
434 ~~current divide) we used a vertical velocity profile appropriate for divide/flank transitional-type~~
435 ~~ice flow. While the ice divide migrated to its present position over the following 250 years~~
436 ~~(1512-1762 CE), the vertical velocity profile transitioned to the present divide-type flow (Fig.~~
437 ~~6a).~~

438 ~~Following Kingslake et al. (2014), the vertical velocity profiles (w) at normalized depth (ζ) was~~
439 ~~parameterized using a shape factor (p) and the vertical velocity at the surface (w_s) (Lliboutry,~~
440 ~~1979):~~

$$w = \left(\frac{w_s}{p} \left(\frac{z}{z_s} \right)^p \right)$$

442 ~~The long-repeat interval (3 years) for the radar measurements meant that no vertical velocity~~
443 ~~measurements were obtained in the firn layer (Fig. 6a). The velocity profile was therefore~~
444 ~~linearly extended to the surface, starting at 155m ice equivalent depth. The vertical surface~~
445 ~~velocity was taken to be 0.26 m ice eq. yr⁻¹, obtained as the sum of the modern accumulation~~
446 ~~rate (0.24 m ice eq. yr⁻¹, i.e. 0.22 m w.e yr⁻¹) and recent ice sheet thinning (0.02m ice eq. yr⁻¹;~~
447 ~~estimated using an ice flow model to match the dated architecture of the Raymond stack). For~~
448 ~~divide-type flow with $w_s = 0.26$, the overall misfit to the measured vertical velocity~~
449 ~~measurements was minimized using $p = 1.22$. For flank type flow, we used $p = 4.16$~~
450 ~~(Kingslake et al., 2014). For the divide/flank transitional-type flow prior to 1512 CE was used~~
451 ~~a linear combination with divide type velocities weighted by 0.7 and flank type velocities~~
452 ~~weighted by 0.3. As the divide migrated, the weighting was changed linearly to obtain full~~
453 ~~divide-type ice flow velocities by 250 years ago.~~

454 Figure 76b shows the resulting thinning function derived for the RICE core site. It decreases
455 from 1.0 at the surface (no strain thinning) to 0.24 at 344 m depth. Past annual accumulation
456 rates in water equivalents can be calculated as the annual layer thicknesses divided by the
457 thinning function and multiplied with the firn/ice density.

458 5.3. Uncertainties in the accumulation history

459 Uncertainties in the inferred accumulation history originate from three sources: (i) identification
460 of the annual layers; (ii) the density profile; (iii) the derived thinning function. Since the
461 RICE17 timescale was found to have negligible bias (Section 7), average layer thicknesses are
462 also not biased, and uncertainties in accumulation history due to layer identification are minor.
463 Uncertainty associated with the density correction is also small. Hence, Except for the
464 uppermost part of the record (with essentially no strain thinning), uncertainty in the thinning
465 function dominates the total uncertainty, and only this factor will be considered here.

466
467 At the surface, uncertainty in the thinning function is zero (~~no strain thinning~~). Increasing
468 uncertainty with depth (Fig. 76b; grey area) arises from: (a) ~~the a~~ lack of measurements in the
469 upper 90 m of the ice sheet to constrain the present near-surface vertical velocity; (b) variation
470 of the vertical velocity profile over time as the divide may have migrated; and (c) in ways not
471 accounted for the amount of ice-sheet thickness change that has occurred. Some of the The
472 second source of uncertainty is mitigated by the information contained in the internal layering
473 of the Roosevelt Island ice dome. because tThe amplitudes of the Raymond stack ~~constrain~~
474 indicate that the onset of divide flow was approximately to about 3000 years ago (Conway et
475 al., 1999; Martín et al., 2006), i.e. prior to the period considered here; that there has been only
476 modest ice-sheet thinning; and that flow conditions have been relatively stable.

477 ~~, and the existence of the Raymond stack reveals that flow conditions have been stable since.~~
478 We develop an estimate for the uncertainty by calculating the thinning function using an
479 ensemble of model assumptions: two different parametrizations of the vertical velocity profiles,
480 two assumptions about the divide migration history, and three values of ice-sheet thickness
481 change. See Supplement S4 for an extended discussion. The uncertainty was defined as the full
482 range of these 12 scenarios, which we suggest to be a 95% confidence interval. The uncertainty
483 on the thinning function is substantial for the older portion of the record as the layers have
484 thinned to a quarter of their initial thickness.

485 ~~Hence, we believe that most uncertainty arises from the lack of vertical velocity measurements~~
486 ~~in the upper part of the ice sheet.~~

487 ~~To assess the magnitude of this uncertainty, we compared results using two alternate thinning~~
488 ~~functions. First, the same method as described above (section 5.2) was used to find the best fit~~
489 ~~to measured vertical velocities, but using a vertical surface velocity of 0.24 m ice eq. yr⁻¹,~~
490 ~~thereby neglecting the contribution from surface lowering. Second, we used the best fit derived~~
491 ~~by Kingslake (2014) The mean difference between the three thinning functions is ~5%, with the~~
492 ~~largest difference (9%) at 78.5 m depth. Accounting also for unknown factors, the uncertainty~~
493 ~~of the thinning function was set to increase from 0% at the surface to 10% at 78.5 m (1730 CE),~~
494 ~~and to remain constant at 10% deeper in the core. This translates to approximately the same~~
495 ~~percentage-wise uncertainty in derived accumulation rates. We suggest to interpret this~~
496 ~~uncertainty as a 95% (2 σ) confidence interval. As the strain increases continuously with depth,~~
497 ~~the relative uncertainty on the accumulation rates is much smaller than the absolute values.~~

498 Results

499 6. Seasonality of impurity influx to Roosevelt Island

500 Using the RICE17 timescale, we can quantify the seasonality of impurity influx to Roosevelt
501 Island visible in the ~~five~~ RICE CFA records: ~~acidity, calcium, conductivity, black carbon and~~
502 ~~insoluble dust particles~~. Figure 87 shows the average seasonal pattern of the various impurities
503 at different depths, assuming constant snowfall through the year.

504 6.1. Acidity

505 The CFA acidity record is driven primarily by the influx of non-sea-salt sulfur-containing
506 compounds, as evident by its high resemblance to the IC non-sea-salt sulfate and ICP-MS non-
507 sea-salt sulfur records in the top part of the core (Fig. 4). Sulfur-containing compounds have a
508 variety of sources, one of which is dimethylsulfide (DMS) emissions by phytoplankton activity
509 during summer (Legrand et al., 1991; Udisti et al., 1998). Correspondingly, acidity displays a
510 regular summer signal, with maximum values in late austral summer (January/February), and
511 minimum values from June through October. This is similar in timing to the seasonal pattern of
512 non-sea-salt sulfate at Law Dome (Curran et al., 1998) and WAIS Divide (Sigl et al., 2016).
513 The acidity contains an annual signal even in the deepest part of the layer-counted timescale
514 (Fig. 87a-c).

~~515 Episodic influxes of sulfuric acids from explosive volcanic eruptions are overprinted on the~~
~~516 annual acidity signal. Biogenic peak values of up to 200ppb non sea salt sulfate are of the same~~
~~517 order as the expected sulfate deposition from large volcanic eruptions, causing the seasonal~~
~~518 signal to effectively obscure the volcanic contributions to the non-sea salt sulfate~~
~~519 concentrations. Volcanic signals are slightly more prominent in the acidity record (Fig. 8a).~~
~~520 This may be explained by only a fraction of the biogenic sulfur emissions being oxidized to~~
~~521 acids, whereas volcanic SO₂ emissions are almost completely oxidized to H₂SO₄ (a strong acid).~~

522 6.2. Sea-salt derived species: Calcium and conductivity

523 As previously noted by Kjær et al. (2016), the RICE conductivity record is almost identical to
524 the mostly sea-salt-derived calcium record (~~see e.g. F~~Fig. s-4, 6-8), suggesting sea spray to be
525 responsible also for peaks in liquid conductivity. We hence consider these two records to be
526 representative of sea salt deposition at Roosevelt Island.

527 Both records typically peak during early-to-mid-winter (June/July), but with large spread in
528 magnitude and timing from year to year (Fig. 78d-i), and oftentimes there are multiple peaks
529 per year. The timing of peak values is approximately similar to sea-salt tracers in WAIS Divide
530 (Sigl et al., 2016), and a few months earlier than peak values in Law Dome (Curran et al., 1998).
531 During the most recent period (1900-1990 CE), we observe a summer peak in the average
532 seasonal conductivity signal, which is not present in the calcium record. This is likely the steady
533 summer contribution ~~to conductivity~~ from biogenic acidity, the seasonality of which being
534 sufficiently prominent to show up in seasonal averages of conductivity in the top part of the
535 core.

536 6.3. Black carbon

537 Seasonal deposition of black carbon (BC) in Antarctic snow is primarily driven by biomass
538 burning and fossil fuel combustion in the Southern Hemisphere, modulated by changes in
539 efficiency of the long-range atmospheric transport- (Bisiaux et al., 2012). Southern Hemispheric
540 fossil fuel emissions have increased since the 1950s (Lamarque et al., 2010), but are ~~still~~

541 believed to be a minor contributor to total black carbon deposition in Antarctica (Bauer et al.,
542 2013).

543 Biomass burning in the Southern Hemisphere peaks towards the end of the dry season, e.g. late
544 summer (Schultz et al., 2008). Given the distinct annual signal in the black carbon record (Fig.
545 78j-l), StratiCounter was set up to assign peaks in BC a nominal date of January 1st (mid-
546 summer). We note that peaks in BC approximately coincide with peaks in acidity (similar to
547 observed in WAIS Divide), thus ensuring consistency of nominal dates throughout the core.
548 Minimum concentration-values of BC are reached in Austral winter (June/July).

549 The annual signal in black carbon changes with depth in the RICE core. During the 20th century,
550 annual cycles exist, but are not very prominent (Fig. 87j). Prior to 1900 CE, the signal is much
551 more distinct, with larger seasonal amplitude as well as higher annual mean concentrations (Fig.
552 87k-l). A recent decrease in BC concentrations has been observed also in the WAIS Divide and
553 Law Dome ice cores, and attributed to a reduction in biofuel emissions from grass fires (Bisiaux
554 et al., 2012). At WAIS Divide and Law Dome, however, the shift takes place several decades
555 later than observed in RICE.

556 With increasing depth in the ice core, thinner annual layers cause the amplitude of the seasonal
557 signal to slowly be reduced. Yet, aided by the high effective depth resolution of the black carbon
558 record, the seasonal cycle persists to great depths in the RICE core, with the deepest part of the
559 layer-counted RICE17 timescale primarily relying on the annual signal in this parameter.

560 6.4. Dust

561 The seasonal pattern in insoluble dust particle concentrations showed a weak annual signal,
562 with a tendency to peak in summer. The simultaneous deposition of black carbon and dust is
563 consistent with both tracers arriving via long-range transport from southern hemispheric
564 continental sources. ~~The dust record showed large non-annual variability, and had limited
565 contribution to the annual layer identification in RICE17.~~

566 7. The layer-counted RICE17 chronology

567 The layer-counted timescale was constructed back to 700 BCE (0-343.72 m), and it forms the
568 most recent part of the Roosevelt Island Ice Core Chronology 2017 (RICE17). It is an
569 independent timescale, constrained only by a few well-known historical events over the last
570 hundred years. Its independence is reflected in the timescale uncertainty: Age confidence
571 intervals show an approximately linear increase with depth (Fig. 98b), reaching a maximum
572 age uncertainty of ± 45 years (95% confidence) at 700 BCE, ~~the end of the layer-counted
573 timescale.~~

574 RICE17 was evaluated by comparing to the ~~highly accurate~~ annual-layer-counted WD2014
575 chronology from WAIS Divide (Sigl et al., 2015, 2016). Timescale comparison was aided by
576 the relative proximity of the two ice cores, and accomplished using two complementary
577 approaches: 1) matching multi-decadal variations in the RICE methane record to a similar
578 record from WAIS Divide; and 2) by matching volcanic marker horizons in the two cores. The
579 two matching procedures were performed independently, and are described in the following
580 sections.

581 Volcanic matching allows very precise age comparisons, but suffers from the risk of incorrect
582 event attribution. Erroneous alignment is less likely to occur when matching records of methane
583 concentration variability. This approach does not allow as high precision, however, due to the
584 multi-decadal nature of the methane variations, as well as the need to account for the gas-age-

585 ice-age difference. Combining the two lines of evidence, the methane match points were used
586 ~~to confirm the independently-obtained volcanic match points, and~~ to validate the absolute ages
587 ~~of the timescale (relative to WD2014), and to confirm the independently-obtained volcanic~~
588 ~~match points. Based on the volcanic matches, a~~ high-precision comparison to WD2014 was
589 achieved ~~based on the volcanic matches~~, allowing an in-depth quality assessment of the RICE17
590 chronology.

591 **7.1. Timescale validation using multi-decadal variability in methane** 592 **concentrations**

593 Centennial-scale variations in methane concentrations observed in the RICE gas records can
594 also be found in similar records from WAIS Divide (Mitchell et al., 2011; WAIS Divide Project
595 Members, 2015). Stratigraphic matching of these records allowed a comparison of the
596 respective ice-core timescales.

597 The gas records from RICE and WAIS Divide were matched using a Monte Carlo technique
598 reported in Lee et al. (2018). The feature-matching routine employed discretely-measured
599 records of methane as well as the isotopic composition of molecular oxygen ($\delta^{18}\text{O}_{\text{atm}}$). Over
600 recent millennia, however, the $\delta^{18}\text{O}_{\text{atm}}$ concentrations have been stable, and hence provided
601 minimal matching constraints. An average spacing of 26 years between successive RICE
602 methane samples contributed to the matching uncertainty. The matching routine identified 18
603 match-points over the past 2700 years, i.e. an average spacing of 150 years. Subsequent visual
604 comparison of the methane profiles suggested minor manual refinements of the match-points
605 (8 years on average, maximum 23 years; all within the uncertainty of the automated matching).
606 These adjustments resulted in a slightly improved fit.

607 Through ~~the~~ methane feature matching, WAIS Divide ages could be transferred to the RICE
608 gas records, i.e. provide an estimate for the RICE gas ages. During the snow densification
609 process, there is a continuous transfer of contemporary air down to the gas lock-in depth,
610 resulting in an offset (Δage) between the ages of ice and gas at a given depth (Schwander and
611 Stauffer, 1984). To obtain the corresponding ice-core ice ages relevant for this study, Δage was
612 calculated using a dynamic Herron-Langway firn densification model (Herron and Langway,
613 1980) following Buizert et al. (2015). The approach is described in detail in Lee et al. (2018).
614 The model is forced using a site temperature history derived from the RICE stable water
615 isotopes, and the firn column thickness is constrained by the isotopic composition of molecular
616 nitrogen ($\delta^{15}\text{N}$ of N_2). In addition to Δage , this formulation of the Herron-Langway
617 densification model produces as output a low-resolution accumulation rate history (section 8.3).

618 Compared to most other Antarctic sites, the relatively high surface temperature and
619 accumulation rate at Roosevelt Island give rise to low Δage values (averaging 160 years over
620 recent millennia) associated with small uncertainties (~ 36 years; 1σ). Combined with the feature
621 matching uncertainty (average: 48 years), total age uncertainty (1σ) in the transfer of WD2014
622 to the RICE core is on average 64 years (maximum: 101 years) over the last 2700 years.

623 The RICE17 timescale is consistent with the WD2014 age of the methane match points (Fig.
624 ~~9a~~**b**). Based on the automatic matching routine, agreement of RICE17 to the gas-matched
625 WD2014 ages is better than 33 years for all age markers, with a root-mean-square (RMS)
626 difference of 17 years. Agreement between the two timescales is even better when using the
627 manually-adjusted match-points, for which the RMS difference is reduced to 13 years. We
628 observe, however, that all methane match points below 275 m are associated with older ages in
629 WD2014 than in RICE, suggesting a small bias in the deeper part of RICE17.

630 7.2. Timescale evaluation from volcanic matching

631 Using the layer counts in RICE17 as guide, volcanic horizons identified in RICE could be linked
632 to the WAIS Divide volcanic record (Sigl et al., 2013, 2015), allowing a detailed comparison
633 of their respective timescales. ~~However, a high background level of marine biogenic sulfuric~~
634 ~~acids precluded a straight-forward identification of volcanic eruptions in the RICE records was~~
635 ~~non-trivial. Based on multiple volcanic proxy records, including –but feasible after the~~
636 ~~introduction of two new volcanic tracers, described below, –match points were found by~~
637 ~~identifying common sequential patterns of acidity spikes in the two cores.~~

638 7.2.1. –

639 ~~7.2.2.7.2.1.~~ **New and conventional ice-core tracers for volcanic activity**

640 With its coastal location and low altitude, the RICE drilling site receives significant seasonal
641 influx of sulfuric acids from biological oceanic sources. ~~Biogenic peak values of up to 200ppb~~
642 ~~non-sea-salt sulfate are of the same order as the expected sulfate deposition from large volcanic~~
643 ~~eruptions, causing the seasonal signal to partly obscure the episodic deposition of sulfuric acids~~
644 ~~from volcanic eruptions. Volcanic signals appeared more distinct in the acidity record (Fig. S4),~~
645 ~~primarily due to the higher resolution of this record.~~

646 ~~–, which tends to obscure sulfur deposition from volcanic eruptions (section 6.1). Traditional~~
647 ~~volcanic ice-core tracers, ECM and sulfur, were not sufficient –generally of limited value– for~~
648 ~~identifying volcanic horizons. The ECM record was very noisy, with few peaks extending~~
649 ~~above the noise level. Resolution of the discretely-sampled sulfur record was too low (below~~
650 ~~67m: 5 cm, i.e. less than <4 samples/year), and it was therefore most valuable in the top. Even~~
651 ~~here, –and even– large volcanoes only left a vague imprint in form of slightly increased sulfur~~
652 ~~levels over a multi-year period (e.g. Fig. 109a), with their most distinct feature being elevated~~
653 ~~sulfur concentrations also during winter. –Detection of volcanic horizons in the RICE core~~
654 ~~therefore primarily relied on two new high-resolution tracers for volcanic activity: direct~~
655 ~~measurements of total acidity (Kjær et al., 2016) and estimated non-sea-salt liquid conductivity.~~

656 Peaks in the RICE liquid conductivity record were caused primarily by sea salts, and thus this
657 record could not on its own be used as volcanic tracer. However, from the close similarity of
658 the conductivity and the mostly sea-salt-derived calcium record (e.g. Figs. 6–4, 9), we could
659 extract a signal of non-sea-salt conductivity, obtained as the conductivity-to-calcium excess
660 ~~($nss\text{-conductivity} = \text{conductivity} - (a \cdot [Ca^{2+}] + b)$, with a and b calculated from linear regression).~~
661 ~~–Being a secondary product, this tracer is prone to measurement errors, calibration and co-~~
662 ~~registration uncertainties, and further complicated by differences in measurement resolution.~~
663 ~~We therefore always double-checked by direct comparison between the two records (Fig. 10a:~~
664 ~~green and grey lines), allowing peaks caused by misalignment and obvious measurement issues~~
665 ~~to be identified. We observed high consistency between peaks in Nevertheless, peaks in the~~
666 ~~non-sea-salt conductivity-to-calcium excess and the total acidity records.~~

667 ~~showed high consistency with peaks in total acidity, and it proved to be a reliable tracer for~~
668 ~~volcanic activity.~~

669 ~~Based on the combined evidence from all proxies, we were able to identify volcanic horizons~~
670 ~~in RICE. A sea sequence of volcanic signals is shown in Figure 109a. Additional sections~~
671 ~~are found in the supplementary (S5). Compared to acidic peaks resulting from unusually high~~
672 ~~biogenic summer activity, volcanic imprints could be distinguished as more prominent and/or~~
673 ~~broader features. Small and short-lived volcanic eruptions, however, were not easily identified.~~

674 **7.2.3-7.2.2. The Pleiades: A tephra-chronological marker horizon**

675 A visible tephra layer was found in RICE at 165m depth, with a RICE17 age of 1251.5±13 CE.
676 Geochemistry of the tephra particles is consistent with an eruption from the Pleiades (Kurbatov
677 et al., 2015), a volcanic group located in Northern Victoria Land, Antarctica (Fig. 1). Tephra of
678 similar geochemistry has been found in several other Antarctic cores dated to approximately
679 the same time, including WAIS Divide (1251.6±2 CE; Dunbar et al. 2010) and Talos
680 Dome/TALDICE (1254±2 CE; Narcisi, Proposito, and Frezzotti 2001; Narcisi et al. 2012). The
681 Pleiades tephra horizon allowed a firm volcanic matching of the RICE and WAIS Divide ice
682 cores at this depth (Fig. 109).

683 The Pleiades tephra horizon was used to select the optimal settings for the StratiCounter
684 algorithm, seeking to reproduce the WD2014 age of the tephra layer as well as possible. The
685 observed compliance of the two age-scales at this depth is therefore to be expected. However,
686 we note that our use of this layer as chronological marker had little impact on the resulting
687 RICE17 timescale: All StratiCounter solutions produced very similar ages for the tephra
688 horizon, and, within the age-scale uncertainties, all were in agreement with the WD2014 age of
689 the tephra.

690 **7.2.4-7.2.3. Volcanic matching to WAIS Divide**

691 Based on the layer counts in RICE17, ~~sequences of volcanic horizons in RICE were~~ we could
692 matched up to volcanic horizons observed in RICE with the WAIS Divide volcanic record (Sigl
693 et al., 2013, 2015). Using an approach similar to the one applied in e.g. Svensson et al. (2013).
694 ~~The matching relied on identifying successive equenees of volcanic events in the two cores~~
695 ~~with similar age spacing (within the associated uncertainties), according to their respective~~
696 ~~timescales (Fig. 10, see also Supplement S5). By taking advantage of the information contained~~
697 ~~within the annual layer counting, we were able to -identify common patterns of volcanic spikes~~
698 ~~in the two cores, allowing a unique match between them (Table 2).~~

699 ~~-Taking this approach was especially important due to the few prominent volcanic horizons in~~
700 ~~the RICE core, and the risk of confounding volcanic and biogenic signals in the RICE records.~~
701 ~~Indeed, for some sections an unequivocal sequence could not be identified; Sections with too~~
702 ~~few or too many closely-spaced acidity spikes in either core were particular problematic. Most~~
703 ~~match points are associated with peaks exceeding two standard deviations of the overall~~
704 ~~variability of the record (Table 2). However, also some smaller peaks were useful, where these~~
705 ~~formed part of a matching sequence of volcanic events. -Reliability increased with density of~~
706 ~~match points in the volcanic sequence. In some sections such sequences were hard to identify,~~
707 ~~either due to timescale differences, too many or too few volcanic events. The volcanic matches~~
708 ~~are provided in Table 2. Multiple additional events in the RICE records of likely volcanic origin~~
709 ~~are not included in Table 2, since they could not be unambiguously matched to a peak in WAIS~~
710 ~~Divide.~~

711 The volcanic matching was in excellent agreement with the independently-obtained methane
712 matching, especially when using the manually-adjusted match points (Fig. 9b).

713 ~~The volcanic matching was in excellent agreement with the independently-obtained methane~~
714 ~~matching, especially when using the manually-adjusted match points (Fig. 8b). A majority of~~
715 ~~the volcanic links identified between the RICE and WAIS Divide ice cores have previously~~
716 ~~been classified as bipolar signals, originating from large tropical volcanoes (Sigl et al., 2013,~~
717 ~~2015). This further strengthens our trust in the volcanic matching, since these large eruptions~~
718 ~~usually deposit acids over an extended area and period, and therefore are expected to be~~
719 ~~recognizable exist also in -from the RICE volcanic records.~~

720

721 **7.2.5.7.2.4. Quality assessment of RICE17**

722 The volcanic matching to WAIS Divide allowed a detailed evaluation of RICE17. The WD2014
723 counting uncertainty is merely 7 years over the last 2700 years, much less than the uncertainty
724 associated with RICE17, and we hence consider it to be the more accurate of the two. Within
725 their respective uncertainties, the RICE17 and WD2014 chronologies are in full agreement at
726 all volcanic marker horizons (Table 2; Fig. 98b). Indeed, the age differences are much less than
727 the accumulated RICE17 age uncertainties. We hence conclude that the inferred confidence
728 bounds on the RICE17 chronology are reliable, if somewhat conservative.

729 Agreement between the two ice-core timescales is particularly remarkable down to 285 m (~150
730 CE). For this most recent part of the RICE17 timescale, the age discrepancy is less than 7 years
731 at all marker horizons, with a RMS age difference of 3 years. Below 285 m, the volcanic
732 matches indicate that RICE17 ~~has a slight~~ ~~may be slightly biased~~ (~3%) ~~bias~~ towards younger
733 ages. This is corroborated by the methane match points (section 7.1). At 285 m, the effective
734 depth resolution of the CFA impurity records (1-2 cm) becomes marginal compared to the
735 annual layer thicknesses (7 cm at 285 m), and we suspect that this has caused the thinnest
736 fraction of annual layers to be indiscernible in the ice core records.

737 Consequently, the deepest section of the layer-counted RICE17 chronology slowly diverges
738 from WD2014, reaching a maximum age difference of 30 years at the oldest identified volcanic
739 marker horizon (343.3 m, 691 BCE \pm 45 years; Table 2). This age offset is of similar magnitude
740 to the uncertainty of the methane-derived RICE17 ages at this depth.

741 **8. Roosevelt Island accumulation history**

742 Annual layer thicknesses in the RICE ice core smoothly decrease with depth, starting from more
743 than 40 cm at the surface to ~6 cm at 344 m (Fig. 99a). After corrections for density changes
744 and ice flow thinning of annual layers with depth (section 5), an annual accumulation rate
745 history for Roosevelt Island over the last 2700 years was obtained (Fig. 101f).

746 **8.1. Long-term accumulation trends**

747 Mean accumulation rates at Roosevelt Island over the entire 2700 year period was 0.25 ± 0.02 m
748 w.e. yr^{-1} . From 700 BCE to ~1300 CE, the accumulation rate at Roosevelt Island shows a
749 slightly increasing trend (Fig. 101f; Table 3), and in 1250 CE, the 20-year running mean
750 accumulation rate reached its maximum over the last 2700 year (0.32 m w.e. yr^{-1}). Since then,
751 accumulation rates have decreased: very slowly until ~1650 CE, then more rapidly (0.10
752 mm/yr^2 from 1650-1965 CE; Table 3). A continued acceleration in the decline of accumulation
753 rates is observed towards the present. Change points and trend estimates with their associated
754 uncertainties were identified using a break function regression analysis (Mudelsee, 2009).
755 ~~However, the analysis revealed that~~ high inter-annual variability in accumulation rates
756 prohibited ~~a~~ very accurate determination of the breakpoints.

757 **8.2. Significant decrease in recent accumulation rates**

758 The Roosevelt Island accumulation history reveals a distinct and rapid accumulation decrease
759 in recent decades (~~Fig. 11~~): Since the mid-1960s, the annual accumulation has decreased with
760 a rate corresponding to 0.8 mm/yr^2 , i.e. 8 times faster than ~~the average~~ over previous centuries.
761 We note, however, that the relatively short time period for conducting the trend analysis,
762 combined with the large inter-annual variability in accumulation rates, causes significant
763 uncertainty in the precise timing of the change-point as well as the trend estimate.

764 Considering the period since 1700 CE (Fig. 12), the lowest decadal mean value of the
765 accumulation rate is observed in the 1990s (0.194 ± 0.001 m w.e. yr^{-1}). Except for very low
766 accumulation rates during the 1850s and 1800s, the remaining top six decades of lowest mean
767 accumulation take place after 1950 CE (Table 4). Indeed, over the last 50 years, only one decade
768 (1960s) stands out as not having experienced below-average accumulation at Roosevelt Island.

769 The current accumulation rate at Roosevelt Island of 0.2104 ± 0.002 m w.e. yr^{-1} (average since
770 1965 CE, $\pm 2\sigma$) is 34% less than the peak accumulation rates around 1250 CE, and 16% below
771 the average of the last 2700 years.

772 8.3. Comparison to the gas-based accumulation rates

773 The RICE17 accumulation history is in reasonable agreement with the low-resolution
774 accumulation rate output from the dynamic Herron-Langway firn densification model (section
775 7.4; Fig. 10f, dashed line). The gas-based accumulation rate history does not resolve high-
776 frequency variations, but shows a slow increase in accumulation rates of 0.02 mm/ yr^2 , similar
777 to the trend obtained from the annual layer thicknesses prior to 1300 CE. However, in contrast
778 to the accumulation rate history derived here, the firn-based accumulation rates continue to
779 increase until present. Further, the absolute value of the inferred gas-based accumulation rates
780 tend to generally underestimate the accumulation rates by ~ 0.04 m w.e. yr^{-1} (16%).

781 We speculate that the discrepancies may have to do with the shift in RICE water isotope levels
782 occurring around 1500 CE (Fig. 10g), which in the firn model is used to represent temperature
783 change. It has been suggested that this shift is due to other factors than temperature (e.g. changes
784 in atmospheric circulation patterns and/or regional sea ice extent (Bertler et al., 2018), and the
785 shift ~~is also~~ coincides with commencement of the divide migration period). By using δD to
786 estimate temperature change, the firn densification model will produce an increase in
787 accumulation rates towards present in order to preserve a constant thickness of the firn column,
788 as indicated by relatively steady values of $\delta^{15}\text{N}-\text{N}_2$ (Fig. 10f, black dots). Further, the model
789 showed a tendency to underestimate the firn column thickness during the earlier part of the
790 period, which may explain the generally lower level of the modelled accumulation rates here.

791 8.4. Spatial consistency in recent accumulation rates

792 Spatial representativeness of the RICE accumulation rates was evaluated by comparing year-
793 to-year profiles of layer thicknesses obtained for the overlap sections of the three available
794 cores: RICE main core, RICE-12/13-B, and RID-75 (Fig. 123), with RID-75 located less than
795 1 km away from the two RICE cores. All cores were corrected for density changes and ice flow
796 thinning using the density and thinning profile from the main RICE core.

797 Annual accumulation records from the three cores are very strongly correlated (correlation
798 coefficients ranging between 0.85 and 0.87), indicating the spatial accumulation pattern across
799 Roosevelt Island to be stable through recent time. The spatial consistency of snow deposition
800 at Roosevelt Island is ~~further confirmed~~ corroborated by the agreement between their measured
801 water isotope records (Fig. 5a). We may therefore disregard depositional noise, and consider
802 the temporal variability in RICE annual layer thicknesses as representative of local snow
803 accumulation.

804 This consistency in accumulation history is in contrast to a high spatial variability in mean
805 accumulation rates across Roosevelt Island ice divide. Repeat surveys over three years (2010-
806 2013) of 144 survey stakes set across Roosevelt Island showed a strong spatial gradient in snow
807 accumulation across the ice divide: Accumulation rates of up to 0.32 m w.e. yr^{-1} were measured
808 on the north eastern flank, decreasing to 0.09 m w.e. yr^{-1} on the south western flank (Bertler et

809 al., 2018). In accordance with these stake measurements, the absolute accumulation rate is
810 found to be significantly less (~7%) for RID-75 than for the ~~two~~-RICE cores. ~~Insignificant~~
811 ~~differences in accumulation rate between the two RICE cores were insignificant-present~~
812 ~~between the two RICE cores~~. Spatial variability in mean accumulation rates, combined with
813 different averaging periods, may explain why previous estimates of Roosevelt Island
814 accumulation rates have varied quite significantly (Bertler et al., 2018; Conway et al., 1999;
815 Herron and Langway, 1980; Kingslake et al., 2014).

816 The representativeness of the Roosevelt Island accumulation rates is corroborated by high
817 spatial correlation of the RICE accumulation rates to gridded ERA-interim precipitation data
818 during recent decades (Bertler et al., 2018). These results suggest that precipitation variability
819 at Roosevelt Island, as observed in RICE, is representative for an extended area, which includes
820 the Ross Ice Shelf, the Southern Ross Sea, and the western part of West Antarctica.

821 **8.5. Influence of ice divide migration on the accumulation history**

822 The recent period (~1500-1750 CE) of divide migration at Roosevelt Island may impact
823 interpretation of the climate records from the RICE core. Ice recovered in the deeper part of the
824 RICE core, deposited before divide migration, have originated west of the ice divide. Present
825 accumulation rates show a distinct decrease on the downwind (western) side of the ice divide
826 with a gradient of $\sim 5 \cdot 10^{-3}$ m w.e./km yr⁻¹ (Bertler et al., 2018), although muted around the
827 summit area. Assuming a stable snowfall pattern through time relative to the divide, the divide
828 ~~its~~ migration would have caused reduced accumulation rates to be observed during the early
829 part (until 1500 CE) of the RICE accumulation history. With the ice originating up to 500m
830 west of the divide at time of deposition, our estimates of Roosevelt Island accumulation rates
831 during this early period may therefore have a small negative bias of up to $2.5 \cdot 10^{-3}$ m w.e. yr⁻¹.

832 Correcting for the influence of ice divide migration, the main impact on the Roosevelt Island
833 accumulation history is an earlier onset of the period with more rapid decrease in accumulation
834 rates. The differences are small, however, and the overall pattern of trends in accumulation rate
835 through time remains the same. In particular, ice divide migration has no impact on
836 accumulation rate trends observed before and after the migration period.

837 **Discussion**

838 **9. The RICE accumulation history in a regional perspective**

839 **9.1. Past accumulation trends across West Antarctica**

840 Regional differences in accumulation, from Northern Victoria Land across West Antarctica to
841 Ellsworth Land, may be evaluated by accumulation reconstructions based on ice core records
842 (Fig. 101).

843 The RICE accumulation history (Fig. 110f) is much more variable on inter-annual and decadal
844 scales than the accumulation rate reconstruction from e.g. WAIS Divide (Fig. 101d). Snowfall
845 at Roosevelt Island is dominated by large and episodic precipitation events (Emanuelsson et al.,
846 2018), which likely contributes to the high inter-annual variability in RICE accumulation rates.
847 A highly dynamic synoptic-scale system brings this precipitation to Roosevelt Island: Positive
848 RICE precipitation anomalies have been linked to the increased occurrence of Eastern Ross
849 Sea/Amundsen Sea blocking events associated with a weak state of the quasi-stationary
850 Amundsen Sea Low (ASL) pressure system. These blocking events impede the prevailing

851 westerly winds, and direct on-shore winds towards the Eastern Ross Sea, thereby increasing the
852 precipitation at Roosevelt Island and Western Marie Byrd Land (Emanuelsson et al., 2018).

853 Only the WAIS Divide and RICE ice cores are available for evaluating multi-millennial-scale
854 accumulation trends and corresponding change points in West Antarctica. Over the past 2700
855 years, WAIS Divide accumulation rates (Fudge et al., 2016) have continuously decreased from
856 a level approximately 25% higher than today (Fig. 40e11d). Accumulation rates declined
857 slowly (-0.01 mm/yr²) until around 900 CE, after which the decline became more rapid (-0.04
858 mm/yr²). This change took place a few centuries before the trend in RICE accumulation rates
859 turned from positive to negative (1300 CE). Covering the last 800 years, the Talos Dome
860 accumulation record (Fig. 40e11c) shows a relatively constant level during this early period,
861 albeit with large decadal variability (Stenni et al., 2002).

862 Considering accumulation changes over the last century, more ice-core accumulation records
863 are available from across West Antarctica; from Victoria Land through to Ellsworth Land. Most
864 West Antarctic ice cores display decreasing accumulation rates over recent decades, but timing
865 and strength of the decrease is location-dependent. The strongest and most recent decrease is
866 observed at RICE (rate change at 1965 CE, this work), with Siple Dome accumulation rates
867 starting to decrease slightly later (1970 CE, Fig. 40e11e; Kaspari et al., 2004). The WAIS
868 Divide site displays the latest and weakest change of rate (ca. 1975 CE; estimated from nearby
869 firn cores; Burgener et al., 2013). An extension of the Talos Dome accumulation record to
870 2010CE using snow stakes (Fig. 40e11c), suggests a recent decrease in accumulation rate also
871 at this location (Frezzotti et al., 2007). In contrast, significant increases in accumulation rates
872 are observed in ice cores from Ellsworth Land, where accumulation rates have shown a steady
873 and marked increase during the 20th century (Fig. 101b, Thomas et al. 2015).

874 The difference in accumulation rate trends across West Antarctica may to a large extent be
875 explained by changes in location and intensity of the ASL over time. The ASL influences
876 ~~precipitation accumulation~~ rates in a dipole pattern: By reducing the number of blocking events,
877 a strong state of the ASL leads to less ~~precipitation accumulation~~ over the Ross Ice Shelf area,
878 and greater ~~precipitation accumulation~~ over Ellsworth Land and the Antarctic Peninsula
879 (Emanuelsson et al., 2018; Raphael et al., 2016). Thus, imposed on West Antarctic-wide
880 accumulation trends, the RICE accumulation history likely reflects the state of the ASL back in
881 time. The ~~precipitation accumulation~~ dipole is centered at the West Antarctic ice divide. Hence,
882 the WAIS Divide ice core should be minimally influenced by the strength of the ASL, and may
883 therefore be ~~considered most~~ representative for West Antarctica as a whole (Fudge et al., 2016).
884 The Northern Victoria Land region, located west of the Ross Ice Shelf, appears to be relatively
885 unaffected by this ASL-induced dipole effect ~~in precipitation~~ which influences Ellsworth Land
886 and West Antarctica. The recent accumulation decrease observed at Talos Dome has been
887 suggested to be caused partly by increased wind-driven sublimation after deposition, due to an
888 increase in mean wind velocities associated with the deepened ASL (Frezzotti et al., 2007).

889 9.2. Connection to sea ice variability in the Ross Sea

890 Throughout the satellite era, RICE accumulation rates are strongly correlated (~~Bertler et al.,~~
891 ~~2018~~) with sea ice extent in the Ross-Amundsen Sea (Jones et al., 2016): Years of reduced sea
892 ice extent are associated with higher accumulation of more isotopically enriched snow and
893 above-normal air temperatures (Bertler et al., 2018).

894 The expansion of sea ice in the Ross Sea during recent decades has taken place concurrently
895 with a marked reduction of sea ice in the Bellingshausen Sea (Comiso and Nishio, 2008), and

896 both trends have been associated with a strengthening of the ASL: The deepened pressure
897 system causes warm poleward-flowing air masses to cross the Bellingshausen Sea, while the
898 returning cold air passes over the Ross Sea, allowing conditions favorable for sea ice expansion
899 (Hosking et al., 2013; Raphael et al., 2016; Turner et al., 2016). The strength of the ASL
900 ~~concurrently~~ affects RICE accumulation rates (section 9.1), with a deep pressure system
901 causing less ~~precipitation accumulation~~ at Roosevelt Island. In addition, an extended regional
902 sea ice cover reduce the availability of local moisture sources. With ~40-60% of the
903 precipitation arriving to Roosevelt Island originating from local sources in the Southern Ross
904 Sea (Tuohy et al., 2015), the relationship between sea ice extent and ~~precipitation accumulation~~
905 rate at Roosevelt Island may also be ascribed a longer distillation pathway of moist air masses
906 during periods of extended sea ice (Kuttel et al., 2012; Noone and Simmons, 2004).

907 The rapid recent decline in Roosevelt Island accumulation rates likely reflects the recent
908 increase in regional sea ice extent, and we ~~hence~~ suggest 1965 CE to mark the modern onset of
909 rapid sea ice expansion in the region. Further investigations are required to determine if the
910 strong relationship between Roosevelt Island accumulation rates and Western Ross Sea sea-ice
911 extent holds over longer timescales. However, the decline in RICE accumulation rates observed
912 since 1300 CE is consistent with previous research indicating that the present increase in sea
913 ice extent in the Ross-Amundsen Seas is part of a long-term trend, having lasted at least the
914 past 300 years (Thomas and Abram, 2016).

915 **9.3. Large-scale circulation changes and implications for recent and** 916 **future trends in Roosevelt Island accumulation**

917 The ASL is sensitive to large-scale circulation patterns, in particular the Southern Annual Mode
918 (SAM) [positive SAM: stronger ASL (e.g. Hosking et al., 2013)] and via teleconnections to the
919 tropical El Niño-Southern Oscillation (ENSO) [stronger ASL during La Niña phase (e.g. Yuan
920 & Martinson 2000)], and the degree to which the two are acting in phase (Clem and Fogt, 2013).
921 A recent strengthening of SAM has been reported (Marshall 2003), consistent with the recent
922 deepening of the ASL (e.g. Raphael et al. 2016).

923 It is not clear whether the recent trends in ASL and Ross Sea sea-ice extent can be ascribed to
924 natural variability. Some studies have attributed the positive trend of SAM in recent decades to
925 Antarctic stratospheric ozone depletion and/or global warming from greenhouse gas emissions
926 (Kushner et al., 2001; Turner et al., 2009), thus suggesting that anthropogenic forcing may play
927 a role. In the future, the competing effects of the two (Arblaster et al., 2011) may define the
928 future state of the ASL, and thereby the accumulation trends observed at Roosevelt Island and
929 across West Antarctica.

930 Most other coastal Antarctic sites have experienced a significant increase (~10%) in
931 accumulation rates since the 1960s (Frezzotti et al., 2013). The broad similarities and
932 differences noted here raise the question of whether West Antarctic accumulation, as a whole,
933 is decreasing, or whether the observed trends merely represent a redistribution of precipitation.
934 It highlights the issue that the current trend in total Antarctic mass balance can only be fully
935 understood pending large spatial data coverage.

936 **10. The RICE volcanic record**

937 **10.1. ~~A record b~~Biased towards regional volcanism**

938 ~~The volcanic proxy records from RICE were significantly different from those from e.g. WAIS~~
939 ~~Divide. At Roosevelt Island, the ~~The coastal setting of Roosevelt Island challenged the~~~~
940 ~~identification of volcanic eruptions in the RICE records, as~~ high background levels of marine

941 sulfate efficiently masked the presence of sulfate from volcanic eruptions. ~~Furthermore, the~~
942 ~~The RICE volcanic proxy acidity~~ records contained a large number of significant peaks without
943 counterpart in WAIS Divide. While some of these may be ~~explained as caused by~~ extreme
944 ~~seasonal influx events~~ of ~~marine seasonal~~ biogenic sulfuric acids ~~sur~~ influx, others may have
945 been produced by regional volcanism.

946 Apart from sulfate, many volcanoes emit acidic compounds based on halogens, e.g. bromine,
947 chlorine and fluoride. The halide acids are highly soluble, and will be removed from the
948 atmosphere relatively quickly during transport. Hence, they will contribute to increased ice
949 acidity in ice cores located close to the eruption site, whereas only sulfate is deposited from
950 distant volcanic eruptions (e.g. Clausen et al., 1997). ~~By~~ ~~using focusing on~~ acidity as ~~the~~
951 ~~primary~~ volcanic tracer (instead of sulfur), ~~we would therefore expect~~ the ~~RICE resulting~~
952 volcanic ~~proxies record to may thus~~ be ~~particularly more~~ sensitive to regional volcanism ~~than~~
953 ~~to larger far-field eruptions~~. ~~This may be a disadvantage of using acidity as volcanic tracer,~~
954 ~~since a high number of regional volcanic horizons will tend to complicate volcanic matching to~~
955 ~~other cores.~~

956 Such geographical bias may be ~~especially particularly~~ important for the Roosevelt Island ice-
957 core records, since there is a prevalence of quiescent regional volcanism with relatively high
958 halogen content in West Antarctica (Zreda-Gostynska et al., 1997). ~~Indeed, preliminary~~
959 ~~investigations suggest that the RICE volcanic records may be biased towards regional~~
960 ~~volcanism: Comparing down-sampled acidity to the discrete sulfur measurements, we observed~~
961 ~~a tendency towards a larger relative size of peaks in acidity for volcanic horizons that were not~~
962 ~~classified as originating from far-field eruptions. Some of the peaks distinctly observed in the~~
963 ~~RICE acidity records, but not present in the WAIS Divide sulfur records, may therefore be due~~
964 ~~to regional volcanism. This may be part of the explanation why the volcanic records from the~~
965 ~~two sites are so different.~~

966 ~~10.2.~~

967 ~~10.3.10.2.~~ Dipole effect in deposition of volcanic tracers across West 968 Antarctica

969 Differences in snow deposition across West Antarctica, influenced by the ASL, may further
970 complicate volcanic matching between ice cores in this region. The ASL dipole acts to direct
971 storm systems either toward the Antarctic Peninsula/Ellsworth Land region, or toward the
972 western Marie Byrd Land/Ross Ice Shelf region. As these storm tracks are associated with
973 snowfall and wet deposition of ions, this is likely to favor deposition and preservation of
974 volcanic signals in one location (e.g. Antarctic Peninsula) at expense of the other (RICE, Siple
975 Dome).

976 An anti-phase in snow accumulation may ~~thus~~ be part of the explanation for the difference
977 between the WAIS Divide and RICE volcanic records. While most of the major volcanic signals
978 in WAIS Divide also exist in RICE, they are not necessarily associated with a prominent signal.
979 Absence of volcanic signal in the RICE core from ~~these~~ large far-field volcanic eruptions may
980 be due to a particularly strong ASL state at the time, directing precipitation and sulfate ions
981 away from Roosevelt Island. A detailed comparison of volcanic records from multiple ice cores
982 is required to evaluate the importance of the ASL for deposition of volcanic tracers across West
983 Antarctica.

984 **10.4.10.3. Volcanic synchronization of low-elevation coastal ice**
985 **cores**

986 A range of ~~five~~ obstacles were overcome to carry out volcanic identification in the RICE core.
987 Similar difficulties will likely challenge volcanic synchronization for other low-elevation
988 coastal Antarctic ice cores (e.g. Philippe et al., 2016), for which many drilling projects are
989 planned within the near future. The methods proposed here may be relevant also for these cores.

990 Robust volcanic matching of RICE and WAIS Divide was possible only by the aid of accurate,
991 high-resolution ice-core timescales for both cores. This demonstrates the importance of
992 building an Antarctic-wide network of accurately-dated volcanic reference horizons, based on
993 tephra, sulfate and acidity. Particular emphasis should be placed on the production of annually-
994 counted timescales for Antarctic ice cores, especially as new and/or improved measurement
995 methods allow the production of high-resolution impurity records for relatively high-
996 accumulation Antarctic sites, such as RICE.

997 **Conclusions**

998 The upper part of the RICE ice core from Roosevelt Island, Ross Ice Shelf, West Antarctica,
999 was dated by annual layer counting back to 700 BCE based on multiple high-resolution impurity
1000 records. The timescale covers a period of stable ice flow after establishment of an ice divide at
1001 Roosevelt Island. The chronology was validated by comparison to the timescale from the WAIS
1002 Divide ice core, West Antarctica, by matching sequences of volcanic events visible primarily
1003 in direct measurements of ice-core acidity and non-sea-salt conductivity. The maritime
1004 environment at Roosevelt Island gave rise to challenging conditions for identifying volcanic
1005 signatures in the ice core, and the volcanic matching was confirmed by matching centennial-
1006 scale variability in atmospheric methane concentrations measured in the two ice cores. The
1007 RICE17 and WD2014 timescales were found to be in excellent agreement.

1008 Based on the layer thickness profile, we produced an annual accumulation record for Roosevelt
1009 Island for the past 2700 years. Similar accumulation histories are observed in three Roosevelt
1010 Island ice cores covering recent times, giving confidence that RICE is a reliable climate archive
1011 suitable for further understanding of climate ~~and geophysical~~ variability across West
1012 Antarctica.

1013 Roosevelt Island accumulation rates were slightly increasing from 700 BCE until 1300 CE,
1014 after which accumulation rates have consistently decreased. Current accumulation trends at
1015 Roosevelt Island indicate a rapid decline of 0.8 mm/yr², starting in the mid-1960s. The modern
1016 accumulation rate of 0.21 ± m.w.e yr⁻¹ (average since 1965CE) is at the low extreme of observed
1017 values during the past several thousands of years. The low present-day accumulation rate has
1018 been linked to a strengthening of the Amundsen Sea Low, and expansion of sea ice in the
1019 Western Ross Sea. The current increase of sea ice in the Ross Sea is therefore likely part of a
1020 long-term increasing trend, although the rapid increase since the mid-1960s may have an
1021 anthropogenic origin.

1022 **Data availability:**

1023 The following data will be made available on the Centre for Ice and Climate website
1024 (<http://www.iceandclimate.nbi.ku.dk/data/>) as well as public archives PANGAEA and NOAA
1025 paleo-databases: RID-75 isotope and beta-activity records; RICE-12/13-B and RID-75
1026 accumulation rates; RICE17 timescale; RICE accumulation rates; and volcanic match points
1027 between RICE and WAIS Divide. Roosevelt Island GPS and radar data ~~have been~~ archived

1028 at the U.S. Antarctic Program Data Center, available
1029 at: <https://gcmd.gsfc.nasa.gov/search/Metadata.do?entry=USAP0944307&subset=GCMD>.

1030 Acknowledgements

1031 This work is a contribution to the Roosevelt Island Climate Evolution (RICE) Program, funded
1032 by national contributions from New Zealand, Australia, Denmark, Germany, Italy, China,
1033 Sweden, UK and USA. The main logistic support was provided by Antarctica New Zealand
1034 (K049) and the US Antarctic Program. We thank all the people involved in the RICE logistics,
1035 fieldwork, sampling and analytical programs. The Danish contribution to RICE was funded by
1036 the Carlsberg Foundation's North-South Climate Connections project grant. The research also
1037 received funding from the European Research Council under the European Community's
1038 Seventh Framework Programme (FP7/2007-2013) ERC grant agreement 610055 as part of the
1039 Ice2Ice project. The RICE Program was supported by funding from NSF grants (PLR-1042883,
1040 ANT-0837883, ANT-0944021, ANT-0944307 and ANT-1643394) and New Zealand Ministry
1041 of Business, Innovation, and Employment grants issued through Victoria University of
1042 Wellington (RDF-VUW-1103, 15-VUW-131), GNS Science (540GCT32, 540GCT12) and
1043 Antarctica New Zealand (K049). Figure 1 was made using Quantarctica2 (Norwegian Polar
1044 Institute) basemaps and QGIS software. [We acknowledge the WAIS Divide ice-core project,
1045 and thank J. McConnell, Jihong Cole-Dai, and the students and staff of the ice core labs at the
1046 Desert Research Institute and at South Dakota State University for providing the WAIS Divide
1047 sulfate data.](#)

1048 We have presented here ice core data collected and analyzed by Henrik Clausen, Willi
1049 Dansgaard, [Sigfus Johnsen](#), Steffen Bo Hansen and Jan Nielsen under the Ross Ice Shelf Project
1050 (RISP) carried out between 1973 and 1978. We acknowledge the pioneering work conducted
1051 by these researchers and the ongoing international collaborations they established.

1052 References

- 1053
- 1054 Abbott, P. M., Davies, S. M., Steffensen, J. P., Pearce, N. J. G., Bigler, M., Johnsen, S. J.,
1055 Seierstad, I. K., Svensson, A. and Wastegård, S.: A detailed framework of Marine Isotope
1056 Stages 4 and 5 volcanic events recorded in two Greenland ice-cores, *Quat. Sci. Rev.*, 36, 59–
1057 77, doi:10.1016/j.quascirev.2011.05.001, 2012.
- 1058 Alley, R. B., Meese, D. A., Shuman, C. A., Gow, A. J., Taylor, K. C., Grootes, P. M., White, J.
1059 W. C., Ram, M., Waddington, E. D., Mayewski, P. A. and Zielinski, G. A.: Abrupt increase in
1060 Greenland snow accumulation at the end of the Younger Dryas event, *Nature*, 362(6420), 527–
1061 529, doi:10.1038/362527a0, 1993.
- 1062 Andersen, K., Svensson, A., Johnsen, S., Rasmussen, S., Bigler, M., Röthlisberger, R., Ruth,
1063 U., Siggaard-Andersen, M.-L., Steffensen, J., Dahl-Jensen, D., Vinther, B. and Clausen, H.:
1064 The Greenland Ice Core Chronology 2005, 15–42ka. Part 1: constructing the time scale, *Quat.*
1065 *Sci. Rev.*, 25(23–24), 3246–3257, doi:10.1016/j.quascirev.2006.08.002, 2006.
- 1066 Arblaster, J. M., Meehl, G. A. and Karoly, D. J.: Future climate change in the Southern
1067 Hemisphere: Competing effects of ozone and greenhouse gases, *Geophys. Res. Lett.*,
1068 38(L02701), 1–6, doi:10.1029/2010GL045384, 2011.
- 1069 Arienzo, M. M., McConnell, J. R., Chellman, N., Criscitiello, A. S., Curran, M., Fritzsche, D.,
1070 Kipfstuhl, S., Mulvaney, R., Nolan, M., Opel, T., Sigl, M. and Steffensen, J. P.: A Method for

1071 Continuous ²³⁹Pu Determinations in Arctic and Antarctic Ice Cores, *Environ. Sci. Technol.*,
1072 50, 7066–7073, doi:10.1021/acs.est.6b01108, 2016.

1073 Bauer, S. E., Bausch, A., Nazarenko, L., Tsigaridis, K., Xu, B., Edwards, R., Bisiaux, M. and
1074 McConnell, J.: Historical and future black carbon deposition on the three ice caps: Ice core
1075 measurements and model simulations from 1850 to 2100, *J. Geophys. Res. Atmos.*, 118(14),
1076 7948–7961, doi:10.1002/jgrd.50612, 2013.

1077 Bender, M. L., Sowers, T., Barnola, J. M. and Chappellaz, J.: Changes in the O₂/N₂ ratio of the
1078 atmosphere during recent decades reflected in the composition of air in the firn at Vostok
1079 Station, Antarctica, *Geophys. Res. Lett.*, 21(3), 189–192, doi:10.1029/93GL03548, 1994.

1080 Bentley, C. R. and Giovinetto, M. B.: Ice-flow studies on the ice dome of Roosevelt Island,
1081 Antarctica, *Trans. Am. Geophys. Union*, 43(3), 369–372, doi:10.1029/TR043i003p00345,
1082 1962.

1083 Bertler, N. A. N., Conway, H., Dahl-Jensen, D., Emanuelsson, D. B., Winstrup, M., Vallelonga,
1084 P. T., Lee, J. E., Brook, E. J., Severinghaus, J. P., Fudge, T. J., Keller, E., Baisden, W. T.,
1085 Hindmarsh, R. C. A., Neff, P. D., Blunier, T., Edwards, R., Mayewski, P. A., Kipfstuhl, S.,
1086 Buizert, C., Canessa, S., Dacic, R., Kjær, H. A., Kurbatov, A. V., Zhang, D., Waddington, E.
1087 D., Baccolo, G., Beers, T., Brightley, H. J., Carter, L., Clemens-Sewall, D., Ciobanu, V. G.,
1088 Delmonte, B., Eling, L., Ellis, A. A., Ganesh, S., Colledge, N., Haines, S. A., Handley, M.,
1089 Hawley, R. L., Hogan, C. M., Johnson, K. M., Korotkikh, E., Lowry, D. P., Mandeno, D.,
1090 McKay, R. M., Menking, J. A., Naish, T. R., Noerling, C., Ollive, A., Orsi, A., Proemse, B. C.,
1091 Pyne, A. R., Pyne, R. L., Renwick, J., Scherer, R. P., Semper, S., Simonsen, M., Sneed, S. B.,
1092 Steig, E. J., Tuohy, A., Ulayottill Venugopal, A., Valero-Delgado, F., Venkatesh, J., Wang, F.,
1093 Wang, S., Winski, D. A., Winton, V. H. L., Whiteford, A., Xiao, C., Yang, J. and Zhang, X.:
1094 The Ross Dipole - temperature, snow accumulation, and sea ice variability in the Ross Sea
1095 Region, Antarctica, over the past 2700 years, *Clim. Past*, 14, 193–214, doi:10.5194/cp-14-193-
1096 2018, 2018.

1097 Bigler, M., Svensson, A., Kettner, E., Vallelonga, P., Nielsen, M. E. and Steffensen, J. P.:
1098 Optimization of high-resolution continuous flow analysis for transient climate signals in ice
1099 cores, *Environ. Sci. Technol.*, 45(10), 4483–4489, doi:10.1021/es200118j, 2011.

1100 Bisiaux, M. M., Edwards, R., McConnell, J. R., Curran, M. A. J., Van Ommen, T. D., Smith,
1101 A. M., Neumann, T. A., Pasteris, D. R., Penner, J. E. and Taylor, K.: Changes in black carbon
1102 deposition to Antarctica from two high-resolution ice core records, 1850-2000 AD, *Atmos.*
1103 *Chem. Phys.*, 12(9), 4107–4115, doi:10.5194/acp-12-4107-2012, 2012.

1104 Blunier, T.: Timing of Millennial-Scale Climate Change in Antarctica and Greenland During
1105 the Last Glacial Period, *Science*, 291(5501), 109–112, doi:10.1126/science.291.5501.109,
1106 2001.

1107 Blunier, T., Chappellaz, J., Schwander, J., Dällenbach, A., Stauffer, B., Stocker, T. F., Raynaud,
1108 D., Jouzel, J., Clausen, H. B., Hammer, C. U. and Johnsen, S. J.: Asynchrony of Antarctic and
1109 Greenland climate change during the last glacial period, *Nature*, 394, 739–743,
1110 doi:10.1038/29447, 1998.

1111 Buizert, C., Cuffey, K. M., Severinghaus, J. P., Baggenstos, D., Fudge, T. J., Steig, E. J.,
1112 Markle, B. R., Winstrup, M., Rhodes, R. H., Brook, E. J., Sowers, T. a., Clow, G. D., Cheng,
1113 H., Edwards, R. L., Sigl, M., McConnell, J. R. and Taylor, K. C.: The WAIS Divide deep ice
1114 core WD2014 chronology - Part 1: Methane synchronization (68–31 ka BP) and the gas age–
1115 ice age difference, *Clim. Past*, 11, 153–173, doi:10.5194/cp-11-153-2015, 2015.

- 1116 Burgener, L., Rupper, S., Koenig, L., Forster, R., Christensen, W. F., Williams, J., Koutnik, M.,
 1117 Miège, C., Steig, E. J., Tingey, D., Keeler, D. and Riley, L.: An observed negative trend in West
 1118 Antarctic accumulation rates from 1975 to 2010: Evidence from new observed and simulated
 1119 records, *J. Geophys. Res. Atmos.*, 118(10), 4205–4216, doi:10.1002/jgrd.50362, 2013.
- 1120 Clapp, J. L.: Summary and Discussion of Survey Control for Ice Flow Studies on Roosevelt
 1121 Island, Antarctica, Univ. Wisconsin Res. Rep., 65(1), 1965.
- 1122 Clausen, H. B., Dansgaard, W., Nielsen, J. O. and Clough, J. W.: Surface accumulation on Ross
 1123 Ice Shelf, *Antarct. J. United States*, 14(5), 68–74, 1979.
- 1124 [Clausen, H. B., Hammer, C. U., Hvidberg, C. S., Dahl-Jensen, D., Steffensen, J. P., Kipfstuhl,](#)
 1125 [J. and Legrand, M.: A comparison of the volcanic records over the past 4000 years from the](#)
 1126 [Greenland Ice Core Project and Dye 3 Greenland ice cores, *J. Geophys. Res. Ocean.*, 102\(C12\),](#)
 1127 [26707–26723, doi:10.1029/97JC00587, 1997.](#)
- 1128
- 1129 Clem, K. R. and Fogt, R. L.: Varying roles of ENSO and SAM on the Antarctic Peninsula
 1130 climate in austral spring, *J. Geophys. Res. Atmos.*, 118, 11481–11492, doi:10.1002/jgrd.50860,
 1131 2013.
- 1132 Comiso, J. C. and Nishio, F.: Trends in the sea ice cover using enhanced and compatible
 1133 AMSR-E, SSM/I, and SMMR data, *J. Geophys. Res. Ocean.*, 113(C02S07), 1–22,
 1134 doi:10.1029/2007JC004257, 2008.
- 1135 Conway, H., Hall, B., Denton, G., Gades, A. and Waddington, E.: Past and future grounding-
 1136 line retreat of the West Antarctic ice sheet, *Science*, 286(280), 280–283,
 1137 doi:10.1126/science.286.5438.280, 1999.
- 1138 Curran, M. A. J., van Ommen, T. D. and Morgan, V.: Seasonal characteristics of the major ions
 1139 in the high-accumulation Dome Summit South ice core, Law Dome, Antarctica, *Ann. Glaciol.*,
 1140 27, 385–390, doi:10.3189/1998AoG27-1-385-390, 1998.
- 1141 Dahl-Jensen, D., Johnsen, S., Hammer, C., Clausen, H. and Jouzel, J.: Past accumulation rates
 1142 derived from observed annual layers in the GRIP ice core from Summit, Central Greenland, in
 1143 NATO ASI Series, vol. I12, edited by W. R. Peltier, pp. 517–532, Springer-Verlag Berlin
 1144 Heidelberg, doi: 10.1007/978-3-642-85016-5, 1993.
- 1145 Dansgaard, W.: Stable isotopes in precipitation, *Tellus*, 16(4), 436–468,
 1146 doi:10.3402/tellusa.v16i4.8993, 1964.
- 1147 Dee, D. P., Uppala, S. M., Simmons, A. J., Berrisford, P., Poli, P., Kobayashi, S., Andrae, U.,
 1148 Balmaseda, M. A., Balsamo, G., Bauer, P., Bechtold, P., Beljaars, A. C. M., van de Berg, L.,
 1149 Bidlot, J., Bormann, N., Delsol, C., Dragani, R., Fuentes, M., Geer, A. J., Haimberger, L.,
 1150 Healy, S. B., Hersbach, H., Hólm, E. V., Isaksen, I., Kållberg, P., Köhler, M., Matricardi, M.,
 1151 McNally, A. P., Monge-Sanz, B. M., Morcrette, J. J., Park, B. K., Peubey, C., de Rosnay, P.,
 1152 Tavolato, C., Thépaut, J. N. and Vitart, F.: The ERA-Interim reanalysis: Configuration and
 1153 performance of the data assimilation system, *Q. J. R. Meteorol. Soc.*, 137(656), 553–597,
 1154 doi:10.1002/qj.828, 2011.
- 1155 Dunbar, N. W., Kurbatov, A. V., Koffman, B. G. and Kreutz, K. J.: Tephra Record of Local
 1156 and Distal Volcanism in the WAIS Divide Ice Core, in WAIS Divide Science Meeting
 1157 September 30th–October 1st, La Jolla, CA, USA. [online] Available from:
 1158 <https://geoinfo.nmt.edu/staff/dunbar/publications/abstracts/dakk2010.html>, 2010.

- 1159 Emanuelsson, B. D., Baisden, W. T., Bertler, N. A. N., Keller, E. D. and Gkinis, V.: High-
1160 resolution continuous-flow analysis setup for water isotopic measurement from ice cores using
1161 laser spectroscopy, *Atmos. Meas. Tech.*, 8(7), 2869–2883, doi:10.5194/amt-8-2869-2015,
1162 2015.
- 1163 Emanuelsson, B. D., Bertler, N. A. N., Neff, P. D., Renwick, J. A., Markle, B. R., Baisden, W.
1164 T. and Keller, E. D.: The role of Amundsen–Bellingshausen Sea anticyclonic circulation in
1165 forcing marine air intrusions into West Antarctica, *Clim. Dyn.*, 1–18, doi:10.1007/s00382-018-
1166 4097-3, 2018.
- 1167 EPICA Community Members: One-to-one coupling of glacial climate variability in Greenland
1168 and Antarctica., *Nature*, 444, 195–198, doi:10.1038/nature05301, 2006.
- 1169 Frezzotti, M., Urbini, S., Proposito, M., Scarchilli, C. and Gandolfi, S.: Spatial and temporal
1170 variability of surface mass balance near Talos Dome, East Antarctica, *J. Geophys. Res. Earth
1171 Surf.*, 112(2), doi:10.1029/2006JF000638, 2007.
- 1172 [Frezzotti, M., Scarchilli, C., Becagli, S., Proposito, M. and Urbini, S.: A synthesis of the](#)
1173 [Antarctic surface mass balance during the last 800 yr, *Cryosphere*, 7\(1\), 303–319,](#)
1174 [doi:10.5194/tc-7-303-2013, 2013.](#)
- 1175
- 1176 Frieß, U., Deutschmann, T., Gilfedder, B., Weller, R. and Platt, U.: Iodine monoxide in the
1177 Antarctic snowpack, *Atmos. Chem. Phys.*, 2439–2456, doi:10.5194/acp-10-2439-2010, 2010.
- 1178 Fudge, T. J., Markle, B. R., Cuffey, K. M., Buizert, C., Taylor, K. C., Steig, E. J., Waddington,
1179 E. D., Conway, H. and Koutnik, M.: Variable relationship between accumulation and
1180 temperature in West Antarctica for the past 31,000 years, *Geophys. Res. Lett.*, 3795–3803,
1181 doi:10.1002/2016GL068356, 2016.
- 1182 Gabrieli, J., Cozzi, G., Vallelonga, P., Schwikowski, M., Sigl, M., Eickenberg, J., Wacker, L.,
1183 Boutron, C., Gäggeler, H., Cescon, P. and Barbante, C.: Contamination of Alpine snow and ice
1184 at Colle Gnifetti, Swiss/Italian Alps, from nuclear weapons tests, *Atmos. Environ.*, 45(3), 587–
1185 593, doi:10.1016/j.atmosenv.2010.10.039, 2011.
- 1186 Hammer, C.: Acidity of polar ice cores in relation to absolute dating, past volcanism, and radio-
1187 echoes, *J. Glaciol.*, 25, 359–372, doi:10.3189/S0022143000015227, 1980.
- 1188 Hammer, C. ., Clausen, H. B., Dansgaard, W., Gundestrup, N., Johnsen, S. and Reeh, N.: Dating
1189 of Greenland ice cores by flow models, isotopes, volcanic debris, and continental dust, *J.
1190 Glaciol.*, 20(82), 3–26, doi:10.3189/S0022143000021183, 1978.
- 1191 Haran, T., Bohlander, J., Scambos, T., Painter, T. and Fahnestock, M.: MODIS Mosaic of
1192 Antarctica 2003–2004 (MOA2004) Image Map, National Snow and Ice Data Center, Boulder,
1193 Colorado, USA, 2013.
- 1194 Herron, M. M. and Langway, C. C.: Dating of Ross Ice Shelf Cores by Chemical Analysis, *J.
1195 Glaciol.*, 24(90), 345–356, doi:10.3189/S0022143000014866, 1979.
- 1196 Herron, M. M. and Langway, C. C.: Firn densification: an empirical model, *J. Glaciol.*, 25(93),
1197 373–385, doi:10.3189/S0022143000015239, 1980.
- 1198 Hosking, J. S., Orr, A., Marshall, G. J., Turner, J. and Phillips, T.: The influence of the
1199 amundsen-bellingshausen seas low on the climate of West Antarctica and its representation in

- 1200 coupled climate model simulations, *J. Clim.*, 26(17), 6633–6648, doi:10.1175/JCLI-D-12-
1201 00813.1, 2013.
- 1202 Jiracek, G. R.: Radio sounding of Antarctic ice, *Univ. Wisconsin Res. Rep.*, 67(1), 1967.
- 1203 Jones, J. M., Gille, S. ., Goosse, H., Abram, N. J., Canziani, P., Charman, D., Clem, K., Crosta,
1204 X., Lavergne, C. de, Eisenman, G., England, M. H., Fogt, R., Frankcombe, L. M., Marshall, G.,
1205 Masson-delmotte, V., Morrison, A. K., Orsi, A., Raphael, M. N., Renwick, J. A., Schneider, D.
1206 P., Simpkins, G. R., Steig, E. J., Stenni, B., Swingedouw, D. and Vance, T. R.: Assessing recent
1207 trends in high-latitude Southern Hemisphere surface climate, *Nat. Clim. Chang.*, 6, 917–926,
1208 doi:10.1038/nclimate3103, 2016.
- 1209 ~~Kalteyer, D. A.: Tephra in Antarctic Ice Cores, Master Thesis, University of Maine, 2015.~~
- 1210 Kaspari, S., Mayewski, P. A., Dixon, D. A., Spikes, V. B., Sneed, S. B., Handley, M. J. and
1211 Hamilton, G. S.: Climate variability in West Antarctica derived from annual accumulation-rate
1212 records from ITASE firn/ice cores, *Ann. Glaciol.*, 39, 585–594,
1213 doi:10.3189/172756404781814447, 2004.
- 1214 Keller, E. D., Baisden, W. T., Bertler, N. A. N., Emanuelsson, B. D., Canessa, S. and Phillips,
1215 A.: Calculating uncertainty for the RICE ice core continuous flow analysis water isotope record,
1216 *Atmos. Meas. Tech. Discuss.*, 2018, 1–20, doi:10.5194/amt-2017-387, 2018.
- 1217 Kingslake, J., Hindmarsh, R. C. A., Adalgeirsdottir, G., Conway, H., Pritchard, H. D., Corr, H.
1218 F. J., Gillet-Chaulet, F., Martin, C., King, E. C., Mulvaney, R. and Pritchard, H. D.: Full-depth
1219 englacial vertical ice sheet velocities measured using phase-sensitive radar, *J. Geophys. Res.*
1220 *Earth Surf.*, 119, 2604–1618, doi:10.1002/2014JF003275, 2014.
- 1221 Kjær, H. A., Vallelonga, P., Svensson, A., Elleskov Kristensen, M. L., Tibuleac, C., Winstrup,
1222 M. and Kipfstuhl, S.: An Optical Dye Method for Continuous Determination of Acidity in Ice
1223 Cores, *Environ. Sci. Technol.*, 50(19), 10485–10493, doi:10.1021/acs.est.6b00026, 2016.
- 1224 Kurbatov, A. V., Kalteyer, D. A., Dunbar, N. W., Yates, M. G., Iverson, N. A. and Bertler, N.
1225 A.: Major element analyses of visible tephra layers in the Roosevelt Island Climate Evolution
1226 Project ice core (Antarctica), *Interdiscip. Earth Data Alliance*, doi:10.1594/IEDA/100554,
1227 2015.
- 1228 Kushner, P. J., Held, I. M. and Delworth, T. L.: Southern Hemisphere Atmospheric Circulation
1229 Response to Global Warming, *J. Clim.*, 14(10), 2238–2249, doi:10.1175/1520-
1230 0442(2001)014<0001:SHACRT>2.0.CO;2, 2001.
- 1231 Kuttel, M., Steig, E. J., Ding, Q., Monaghan, A. J. and Battisti, D. S.: Seasonal climate
1232 information preserved in West Antarctic ice core water isotopes : relationships to temperature,
1233 large-scale circulation, and sea ice, *Clim. Dyn.*, 39, 1841–1857, doi:10.1007/s00382-012-1460-
1234 7, 2012.
- 1235 Lamarque, J. F., Bond, T. C., Eyring, V., Granier, C., Heil, A., Klimont, Z., Lee, D., Liousse,
1236 C., Mieville, A., Owen, B., Schultz, M. G., Shindell, D., Smith, S. J., Stehfest, E., Van
1237 Aardenne, J., Cooper, O. R., Kainuma, M., Mahowald, N., McConnell, J. R., Naik, V., Riahi,
1238 K. and Van Vuuren, D. P.: Historical (1850–2000) gridded anthropogenic and biomass burning
1239 emissions of reactive gases and aerosols: Methodology and application, *Atmos. Chem. Phys.*,
1240 10(15), 7017–7039, doi:10.5194/acp-10-7017-2010, 2010.
- 1241 Langway, C. C., Herron, M. and Cragin, J. H.: Chemical Profile of the Ross Ice Shelf at Little
1242 America V, Antarctica, *J. Glaciol.*, 13(69), 431–435, doi:10.3189/S0022143000023200, 1974.

- 1243 Lee, J., Brook, E. J., Bertler, N. A. N., Buizert, C., Baisden, W. T., Blunier, T., Ciobanu, G.,
1244 Conway, H., Dahl-Jensen, D., Fudge, T. J., Hindmarsh, R. C. A., Keller, E. D., Parrenin, F.,
1245 Severinghaus, J. P., Vallelonga, P., Waddington, E. D. and Winstrup, M.: A 83,000 year old ice
1246 core from Roosevelt Island, Ross Sea, Antarctica, *Clim. Past Discuss.*, 1–44, doi:10.5194/cp-
1247 2018-68, 2018.
- 1248 Legrand, M., Feniet-Saigne, C., Saltzman, E. S., Germain, C., Barkov, N. I. and Petrov, V. N.:
1249 Ice-core record of oceanic emissions of dimethylsulphide during the last climate cycle, *Nature*,
1250 350(6314), 144–146, doi:10.1038/350144a0, 1991.
- 1251 Lliboutry, L. A.: A critical review of analytical approximate solutions for steady state velocities
1252 and temperatures in cold ice sheets, *Gletscherkd. Glazialgeol.*, 15(2), 135–148, 1979.
- 1253 Marshall, G. J.: Trends in the Southern Annular Mode from Observations and Reanalyses, *J.*
1254 *Clim.*, 16(24), 4134–4143, doi:10.1175/1520-0442(2003)016<4134:TITSAM>2.0.CO;2,
1255 2003.
- 1256 Martín, C., Hindmarsh, R. C. A. and Navarro, F. J.: Dating ice flow change near the flow divide
1257 at Roosevelt Island, Antarctica, by using a thermomechanical model to predict radar
1258 stratigraphy, *J. Geophys. Res. Earth Surf.*, 111(1), 1–15, doi:10.1029/2005JF000326, 2006.
- 1259 McConnell, J. R., Edwards, R., Kok, G. L., Flanner, M. G. and Zender, C. S.: 20th-Century
1260 industrial black carbon emissions altered Arctic climate forcing, *Science*, 317(5843), 1381–
1261 1384, doi:10.1126/science.1144856, 2007.
- 1262 Mitchell, L. E., Brook, E. J., Sowers, T., McConnell, J. R. and Taylor, K.: Multidecadal
1263 variability of atmospheric methane, 1000–1800 C.E., *J. Geophys. Res. Biogeosciences*, 116(2),
1264 1–16, doi:10.1029/2010JG001441, 2011.
- 1265 Mitchell, L. E., Brook, E. J., Lee, J. E., Buizert, C. and Sowers, T.: Constraints on the Late
1266 Holocene Anthropogenic Contribution to the Atmospheric Methane Budget, *Science*,
1267 342(6161), 964–966, doi:10.1126/science.1238920, 2013.
- 1268 ~~Mudelsee, M.: Ramp function regression: A tool for quantifying climate transitions, *Computers,*
1269 *26*, 293–307, doi:10.1140/epjst/e2009-01089-3, 2009.~~
- 1270 Mudelsee, M.: Break function regression, *Eur. Phys. J. Spec. Top.*, 174(1), 49–63,
1271 doi:10.1140/epjst/e2009-01089-3, 2009.
- 1272 Muscheler, R., Adolphi, F. and Knudsen, M. F.: Assessing the differences between the IntCal
1273 and Greenland ice-core time scales for the last 14,000 years via the common cosmogenic
1274 radionuclide variations, *Quat. Sci. Rev.*, 106, 81–87, doi:10.1016/j.quascirev.2014.08.017,
1275 2014.
- 1276 Narcisi, B., Proposito, M. and Frezzotti, M.: Ice record of a 13th century explosive volcanic
1277 eruption in northern Victoria Land, East Antarctica, *Antarct. Sci.*, 13(2), 174–181,
1278 doi:10.1017/S0954102001000268, 2001.
- 1279 Narcisi, B., Petit, J. R., Delmonte, B., Scarchilli, C. and Stenni, B.: A 16,000-yr tephra
1280 framework for the Antarctic ice sheet: A contribution from the new Talos Dome core, *Quat.*
1281 *Sci. Rev.*, 49, 52–63, doi:10.1016/j.quascirev.2012.06.011, 2012.
- 1282 ~~Nereson, N. A. and Waddington, E. D.: Isochrones and isotherms beneath migrating ice divides,
1283 *J. Glaciol.*, 48(160), 95–108, doi:10.3189/172756502781831647, 2002.~~
- 1284

- 1285 Noone, D. and Simmons, I.: Sea ice control of water isotope transport to Antarctica and
1286 implications for ice core interpretation, *J. Geophys. Res.*, 109, 1–13,
1287 doi:10.1029/2003JD004228, 2004.
- 1288 Nye, J. F.: Correction Factor for Accumulation Measured by the Thickness of the Annual
1289 Layers in an Ice Sheet, *J. Glaciol.*, 4(36), 785–788, doi:10.3189/S0022143000028367, 1963.
- 1290 Philippe, M., Tison, J. L., Fjøsne, K., Hubbard, B., Kjær, H. A., Lenaerts, J. T. M., Drews, R.,
1291 Sheldon, S. G., De Bondt, K., Claeys, P. and Pattyn, F.: Ice core evidence for a 20th century
1292 increase in surface mass balance in coastal Dronning Maud Land, East Antarctica, *Cryosph.*,
1293 10(5), 2501–2516, doi:10.5194/tc-10-2501-2016, 2016.
- 1294 Rabiner, L. R.: A Tutorial on Hidden Markov Models and Selected Applications in Speech
1295 Recognition, *Proc. IEEE*, 77(2), 257–286, doi:10.1109/5.18626, 1989.
- 1296 Raisbeck, G. M., Cauquoin, A., Jouzel, J., Landais, A., Petit, J.-R., Lipenkov, V. Y., Beer, J.,
1297 Synal, H.-A., Oerter, H., Johnsen, S. J., Steffensen, J. P., Svensson, A. and Yiou, F.: An
1298 improved north–south synchronization of ice core records around the 41 kyr ¹⁰Be peak, *Clim.*
1299 *Past*, 13(3), 217–229, doi:10.5194/cp-13-217-2017, 2017.
- 1300 Raphael, M. N., Marshall, G. J., Turner, J., Fogt, R. L., Schneider, D., Dixon, D. A., Hosking,
1301 J. S., Jones, J. M. and Hobbs, W. R.: The Amundsen sea low: Variability, change, and impact
1302 on Antarctic climate, *Bull. Am. Meteorol. Soc.*, 97(1), 111–121, doi:10.1175/BAMS-D-14-
1303 00018.1, 2016.
- 1304 Rasmussen, S. O., Andersen, K. K., Svensson, A. M., Steffensen, J. P., Vinther, B. M., Clausen,
1305 H. B., Siggaard-Andersen, M. L., Johnsen, S. J., Larsen, L. B., Dahl-Jensen, D., Bigler, M.,
1306 Röthlisberger, R., Fischer, H., Goto-Azuma, K., Hansson, M. E. and Ruth, U.: A new Greenland
1307 ice core chronology for the last glacial termination, *J. Geophys. Res. Atmos.*, 111(6),
1308 doi:10.1029/2005JD006079, 2006.
- 1309 Raymond, C. F.: Deformation in the Vicinity of Ice Divides, *J. Glaciol.*, 29(103), 357–373,
1310 doi:10.3189/S0022143000030288, 1983.
- 1311 Schultz, M. G., Heil, A., Hoelzemann, J. J., Spessa, A., Thonicke, K., Goldammer, J. G., Held,
1312 A. C., Pereira, J. M. C. and van Het Bolscher, M.: Global wildland fire emissions from 1960 to
1313 2000, *Global Biogeochem. Cycles*, 22(2), 1–17, doi:10.1029/2007GB003031, 2008.
- 1314 Schwander, J. and Stauffer, B.: Age difference between polar ice and the air trapped in its
1315 bubbles, *Nature*, 311, 45–47, doi:10.1038/311045a0, 1984.
- 1316 Shepherd, A., Ivins, E. R., A, G., Barletta, V. R., Bentley, M. J., Bettadpur, S., Briggs, K. H.,
1317 Bromwich, D. H., Forsberg, R., Galin, N., Horwath, M., Jacobs, S., Joughin, I., King, M. A.,
1318 Lenaerts, J. T., Li, J., Ligtenberg, S. R. M., Luckman, A., McMillan, M., Meister, R., Milne,
1319 G., Mouginot, J., Muir, A., Nicolas, J., Paden, J., Payne, A. J., Pritchard, H. D., Rignot, E., Rott,
1320 H., Sørensen, L. S., Scambos, T. A., Scheuchl, B., Schrama, E. J. O., Smith, B., Sundal, A. V.,
1321 Angelen, J. H. van, Berg, W. J. van der, Broeke, M. R. van der, Vaughan, D. G., Velicogna, I.,
1322 Wahr, J., Whitehouse, P. L., Wingham, D. J., Yi, D., Young, D. and Zwally, H. J.: A Reconciled
1323 Estimate of Ice-Sheet Mass Balance, *Science*, 338, 1183–1190, doi:10.1126/science.1228102,
1324 2012.
- 1325 Sigl, M., McConnell, J. R., Layman, L., Maselli, O., McGwire, K., Pasteris, D., Dahl-Jensen,
1326 D., Steffensen, J. P., Vinther, B., Edwards, R., Mulvaney, R. and Kipfstuhl, S.: A new bipolar
1327 ice core record of volcanism from WAIS Divide and NEEM and implications for climate

- 1328 forcing of the last 2000 years, *J. Geophys. Res. Atmos.*, 118(3), 1151–1169,
1329 doi:10.1029/2012JD018603, 2013.
- 1330 Sigl, M., Winstrup, M., McConnell, J. R., Welten, K. C., Plunkett, G., Ludlow, F., Büntgen, U.,
1331 Caffee, M., Chellman, N., Dahl-Jensen, D., Fischer, H., Kipfstuhl, S., Kostick, C., Maselli, O.
1332 J., Mekhaldi, F., Mulvaney, R., Muscheler, R., Pasteris, D. R., Pilcher, J. R., Salzer, M.,
1333 Schüpbach, S., Steffensen, J. P., Vinther, B. M. and Woodruff, T. E.: Timing and climate
1334 forcing of volcanic eruptions for the past 2,500 years., *Nature*, 523(7562), 543–9,
1335 doi:10.1038/nature14565, 2015.
- 1336 Sigl, M., Fudge, T. J., Winstrup, M., Cole-Dai, J., Ferris, D., McConnell, J. R., Taylor, K. C.,
1337 Welten, K. C., Woodruff, T. E., Adolphi, F., Bisiaux, M., Brook, E. J., Buizert, C., Caffee, M.
1338 W., Dunbar, N. W., Edwards, R., Geng, L., Iverson, N., Koffman, B., Layman, L., Maselli, O.
1339 J., McGwire, K., Muscheler, R., Nishiizumi, K., Pasteris, D. R., Rhodes, R. H. and Sowers, T.
1340 A.: The WAIS Divide deep ice core WD2014 chronology - Part 2: Annual-layer counting (0-
1341 31 ka BP), *Clim. Past*, 12(3), 769–786, doi:10.5194/cp-12-769-2016, 2016.
- 1342 Spolaor, A., Vallelonga, P., Gabrieli, J., Martma, T., Björkman, M. P., Isaksson, E., Cozzi, G.,
1343 Turetta, C., Kjær, H. A., Curran, M. A. J., Moy, A. D., Schönhardt, A., Blechschmidt, A. M.,
1344 Burrows, J. P., Plane, J. M. C. and Barbante, C.: Seasonality of halogen deposition in polar
1345 snow and ice, *Atmos. Chem. Phys.*, 14(18), 9613–9622, doi:10.5194/acp-14-9613-2014, 2014.
- 1346 Steig, E. J., Mayewski, P. A., Dixon, D. A., Kaspari, S. D., Frey, M. M., Schneider, D. P.,
1347 Arcone, S. A., Hamilton, G. S., Spikes, V. B., Albert, M., Meese, D., Gow, A. J., Shuman, C.
1348 A., White, J. W. C., Sneed, S., Flaherty, J. and Wumkes, M.: High-resolution ice cores from
1349 US ITASE (West Antarctica): development and validation of chronologies and determination
1350 of precision and accuracy, *Ann. Glaciol.*, 41(1), 77–84, doi:10.3189/172756405781813311,
1351 2005.
- 1352 Stenni, B., Proposito, M., Gragnani, R., Flora, O., Jouzel, J., Falourd, S. and Frezzotti, M.: Eight
1353 centuries of volcanic signal and climate change at Talos Dome (East Antarctica), *J. Geophys.*
1354 *Res.*, 107(D9), 1–13, doi:10.1029/2000JD000317, 2002.
- 1355 Stenni, B., Curran, M. A. J., Abram, N. J., Orsi, A., Goursaud, S., Masson-Delmotte, V.,
1356 Neukom, R., Goosse, H., Divine, D., van Ommen, T., Steig, E. J., Dixon, D. A., Thomas, E. R.,
1357 Bertler, N. A. N., Isaksson, E., Ekaykin, A., Frezzotti, M. and Werner, M.: Antarctic climate
1358 variability at regional and continental scales over the last 2000 years, *Clim. Past*, 13, 1609–
1359 1634, doi:10.5194/cp-2017-40, 2017.
- 1360 Stowasser, C., Buizert, C., Gkinis, V., Chappellaz, J., Schapbach, S., Bigler, M., Fan, X.,
1361 Sperlich, P., Baumgartner, M., Schilt, A. and Blunier, T.: Continuous measurements of methane
1362 mixing ratios from ice cores, *Atmos. Meas. Tech.*, 5(5), 999–1013, doi:10.5194/amt-5-999-
1363 2012, 2012.
- 1364 Svensson, A., Andersen, K. K., Bigler, M., Clausen, H. B., Dahl-Jensen, D., Davies, S. M.,
1365 Johnsen, S. J., Muscheler, R., Parrenin, F., Rasmussen, S. O., Rothlisberger, R., Seierstad, I.,
1366 Steffensen, J. P. and Vinther, B. M.: A 60 000 year Greenland stratigraphic ice core chronology,
1367 *Clim. Past*, 4, 47–57, doi:10.5194/cpd-3-1235-2007, 2008.
- 1368 [Svensson, A., Bigler, M., Blunier, T., Clausen, H. B., Dahl-Jensen, D., Fischer, H., Fujita, S.,](#)
1369 [Goto-Azuma, K., Johnsen, S. J., Kawamura, K., Kipfstuhl, S., Kohno, M., Parrenin, F., Popp,](#)
1370 [T., Rasmussen, S. O., Schwander, J., Seierstad, I., Severi, M., Steffensen, J. P., Udisti, R.,](#)
1371 [Uemura, R., Vallelonga, P., Vinther, B. M., Wegner, A., Wilhelms, F. and Winstrup, M.: Direct](#)
1372 [linking of Greenland and Antarctic ice cores at the Toba eruption \(74 ka BP\). *Clim. Past*, 9\(2\).](#)

1373 [749–766, doi:10.5194/cp-9-749-2013, 2013.](#)
1374
1375 Thomas, E. R. and Abram, N. J.: Ice core reconstruction of sea ice change in the Amundsen-
1376 Ross Seas since 1702 A.D., *Geophys. Res. Lett.*, 43(10), 5309–5317,
1377 doi:10.1002/2016GL068130, 2016.

1378 Thomas, E. R., Hosking, J. S., Tuckwell, R. R., Warren, R. A. and Ludlow, E. C.: Twentieth
1379 century increase in snowfall in coastal West Antarctica, *Geophys. Res. Lett.*, 42(21), 9387–
1380 9393, doi:10.1002/2015GL065750, 2015.

1381 Thomas, E. R., van Wessem, J. M., Roberts, J., Isaksson, E., Schlosser, E., Fudge, T.,
1382 Vallelonga, P., Medley, B., Lenaerts, J., Bertler, N., van den Broeke, M. R., Dixon, D. A.,
1383 Frezzotti, M., Stenni, B., Curran, M. and Ekaykin, A. A.: Regional Antarctic snow
1384 accumulation over the past 1000 years, *Clim. Past*, 13, 1491–1513, doi:10.5194/cp-13-
1385 14912017-18-2017, 2017.

1386 Traversi, R., Becagli, S., Castellano, E., Maggi, V., Morganti, A., Severi, M. and Udisti, R.:
1387 Ultra-sensitive Flow Injection Analysis (FIA) determination of calcium in ice cores at ppt level,
1388 *Anal. Chim. Acta*, 594(2), 219–225, doi:10.1016/j.aca.2007.05.022, 2007.

1389 Tuohy, A., Bertler, N., Neff, P., Edwards, R., Emanuelsson, D., Beers, T. and Mayewski, P.:
1390 Transport and deposition of heavy metals in the Ross Sea Region, Antarctica, *J. Geophys. Res.*
1391 *Atmos.*, 120(20), 10996–11011, doi:10.1002/2015JD023293, 2015.

1392 Turner, J., Comiso, J. C., Marshall, G. J., Lachlan-cope, T. A., Bracegirdle, T., Maksym, T.,
1393 Meredith, M. P., Wang, Z. and Orr, A.: Non-annular atmospheric circulation change induced
1394 by stratospheric ozone depletion and its role in the recent increase of Antarctic sea ice extent,
1395 *Geophys. Res. Lett.*, 36(L08502), 1–5, doi:10.1029/2009GL037524, 2009.

1396 Turner, J., Hosking, J. S., Marshall, G. J., Phillips, T. and Bracegirdle, T. J.: Antarctic sea ice
1397 increase consistent with intrinsic variability of the Amundsen Sea Low, *Clim. Dyn.*, 46(7),
1398 2391–2402, doi:10.1007/s00382-015-2708-9, 2016.

1399 Udisti, R., Traversi, R., Becagli, S. and Piccardi, G.: Spatial distribution and seasonal pattern
1400 of biogenic sulphur compounds in snow from northern Victoria Land, Antarctica, *Ann. Glaciol.*,
1401 27, 535–542, doi:10.3189/1998AoS27-1-535-542, 1998.

1402 WAIS Divide Project Members: Precise inter-polar phasing of abrupt climate change during the
1403 last ice age, *Nature*, 520(7549), 661–665, doi:10.1038/nature14401, 2015.

1404 Wheatley, S. and Kurbatov, A. V.: Antarctic Ice Core Tephra Analysis, U.S. Antarct. Progr.
1405 Data Center. Dataset., doi:10.15784/601038, 2017.

1406 Winstrup, M.: A Hidden Markov Model Approach to Infer Timescales for High-Resolution
1407 Climate Archives, in Proceedings of the 30th AAAI Conference on Artificial Intelligence and
1408 the 28th Innovative Applications of Artificial Intelligence Conference, pp. 4053–4061, AAAI
1409 Press, Palo Alto, California, February 12 – 17, 2016, Phoenix, Arizona USA., 2016.

1410 Winstrup, M., Svensson, A. M., Rasmussen, S. O., Winther, O., Steig, E. J. and Axelrod, A. E.:
1411 An automated approach for annual layer counting in ice cores, *Clim. Past*, 8(6), 1881–1895,
1412 doi:10.5194/cp-8-1881-2012, 2012.

1413 Yu, S. Z.: Hidden semi-Markov models, *Artif. Intell.*, 174(2), 215–243,
1414 doi:10.1016/j.artint.2009.11.011, 2010.

1415 Yuan, X. and Martinson, D. G.: Antarctic sea ice extent variability and its global connectivity,
1416 J. Clim., 13(10), 1697–1717, doi:10.1175/1520-0442(2000)013<1697:ASIEVA>2.0.CO;2,
1417 2000.

1418 Zreda-Gostynska, G., Kyle, P. R., Finnegan, D. and Meeker Prestbo, K.: Volcanic gas
1419 emissions from Mount Erebus and their impact on the Antarctic environment, J. Geophys. Res.,
1420 102055(10), 39–15, doi:10.1029/97JB00155, 1997.

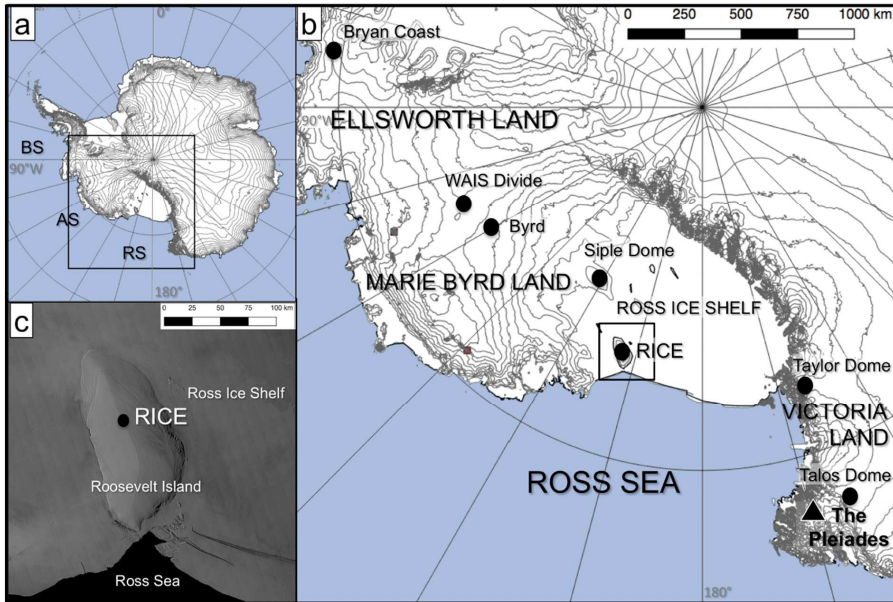
1421

1422

1423

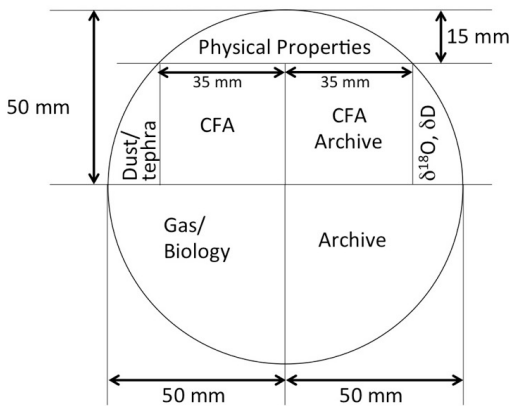
1424

1425 **Figures**



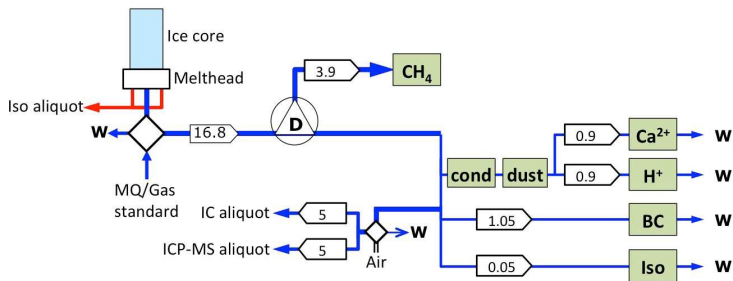
1426
1427

1428 **Figure 1: a, b):** Roosevelt Island is located in the eastern sector of the Ross Ice Shelf
 1429 embayment. Locations discussed in the text are represented by circles (ice cores) and by
 1430 triangles (volcanoes) and circles (ice cores). RS: Ross Sea; AS: Amundsen Sea; BS:
 1431 Bellingshausen Sea. **c)** MODIS image of Roosevelt Island (Haran et al. 2013), protruding as an
 1432 ice dome from the surrounding Ross Ice Shelf. The RICE ice core was -is- drilled on the ice
 1433 divide of Roosevelt Island.



1434

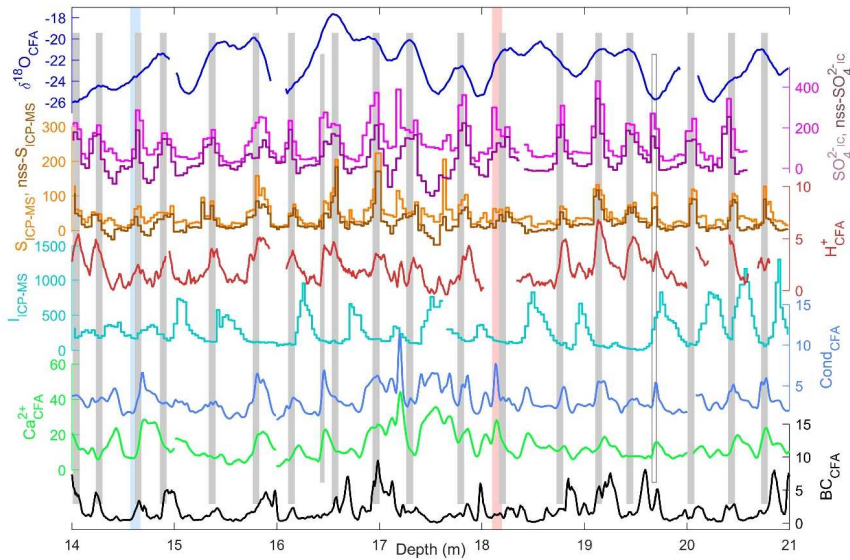
1435 **Figure 2:** The RICE main core cutting plan included 2 CFA sticks of size 35x35mm.



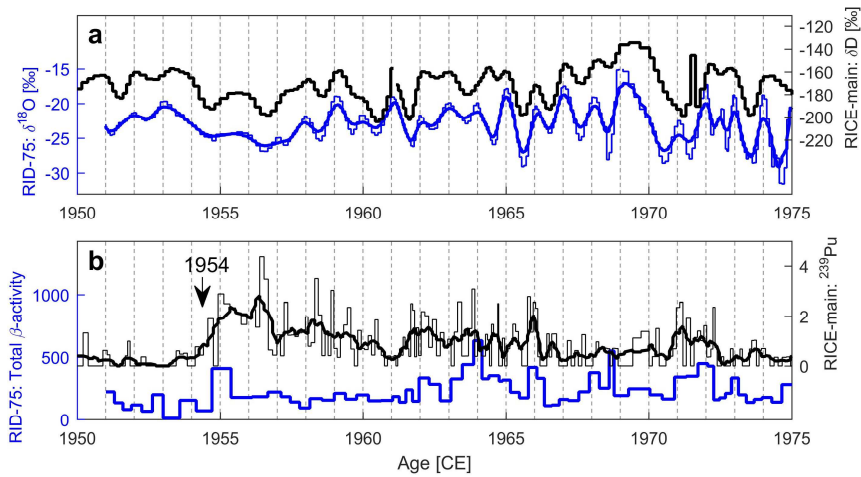
1436

1437 **Figure 3:** The RICE CFA set-up. A 1m long ice-core rod (light blue) is placed on a melt head,
 1438 which separates melt water from the pristine inner part of the core from that of the more
 1439 contaminated outer rim. Meltwater from the outer stream (red) is used for discrete
 1440 measurements of water isotopes, while the melt water stream from the inner core section (dark
 1441 blue) passes through a debubbler (D), which separates air from the melt water. The air
 1442 composition is analyzed for methane concentration, while the meltwater stream is channeled to
 1443 various analytical instruments for continuous impurity analysis of dust, conductivity (cond),
 1444 calcium (Ca²⁺), acidity (H⁺), black carbon (BC), and water isotopes (Iso), as well as collected
 1445 in vials for discrete aliquot sampling by IC and ICP-MS. W denotes waste water. Diamonds
 1446 represent injection valves used for introduction of air or water standards when the melter system
 1447 is not in use. Arrow boxes indicate liquid flow rates in mL min⁻¹. Green boxes represent
 1448 analytical instruments.

1449

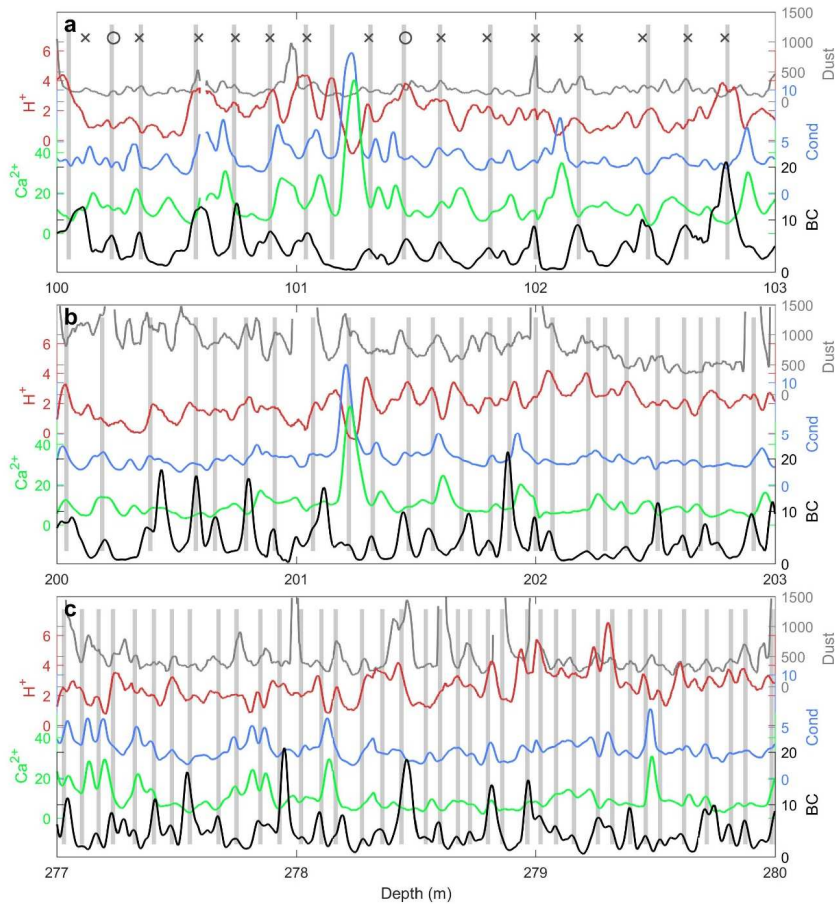


1450
 1451 **Figure 4:** Assignment of annual layers in an upper section of the RICE core. All units are in
 1452 ppb, except for $\delta^{18}\text{O}$ (in ‰), H^+ (in $\mu\text{eq L}^{-1}$), and conductivity (in $\mu\text{S cm}^{-1}$). The CFA chemistry
 1453 records are smoothed with a 3-cm moving average filter. The timescale is constrained by two
 1454 tie-points within this interval: the isotope match to RID-75 (blue bar; 14.6 m) and the Raoul
 1455 tephra horizon (red bar; 18.1 m). At two locations, the annual layering is unclear (shorter bars),
 1456 but can be mostly resolved on basis of the tie-point ages. As a result, the uncertain layer at 16.6
 1457 m (short grey bar) is included as a year in the timescale, whereas the uncertain layer at 19.7m
 1458 (short white bar) is not. For the second layer, the sulfate record suggests that it is an annual
 1459 layer, but this is not supported by iodine and $\delta^{18}\text{O}$. As we assume an uncertainty of $\pm 1\text{yr}$ for the
 1460 tie-point ages, the layer at 16.6m could possibly be removed from the timescale, while still
 1461 adhering to the age constraints. The existence of this uncertain layer therefore gives rise to a 1-
 1462 year increase of the timescale uncertainty. Two uncertain layers exist within the section: At
 1463 16.6 m, an uncertain layer is being counted as part of the timescale, in order to match the tiepoint
 1464 ages corresponding to the isotope match to RID-75 (cyan bar; 14.6 m) and the Raoul tephra
 1465 horizon (red bar; 18.1 m). A second uncertain layer is located at 19.7 m; the sulfate record
 1466 suggest that it is an annual layer, but this is not supported by iodine and $\delta^{18}\text{O}$. This layer is not
 1467 counted in the RICE17 chronology, in order to match the age of the next tie-point located at 22
 1468 m.
 1469



1470

1471 **Figure 5:** a) RICE water isotope profile (δD) compared to isotope data ($\delta^{18}\text{O}$) from the RID-
 1472 75 core for the period 1950-1975. Diffusion causes the isotope record to smooth over time, and
 1473 a smoothed version of the RID-75 isotope profile (thick blue) highlights its similarities to the
 1474 RICE isotope record (black). b) Total specific β -activity (in disintegrations per hour, dph) for
 1475 the RID-75 core compared to ^{239}Pu measurements (normalized intensities) from the RICE main
 1476 core. Both cores show a sharp increase in nuclear waste deposition starting in 1954 CE, and
 1477 several broader peaks hereafter.



1478

1479

1480

1481

1482

1483

1484

1485

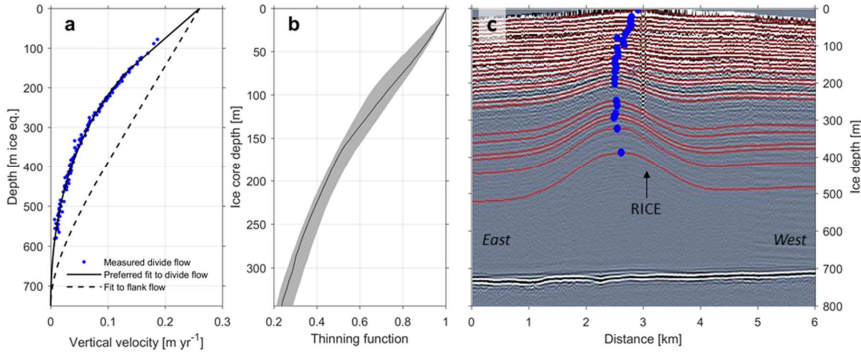
1486

1487

1488

Figure 6: CFA data and annual layer counts (grey bars) in three 3m-long sections (a-c) of the RICE core. In general, the most distinct annual signal is found in the BC record, but the other records also contain valuable information on the annual layering. Due to contamination from drill fluid, the dust record was not used for layer counting below 129m. For the top section (a), the preliminary set of manual layer counts used for initializing StratiCounter are shown: Crosses (x) indicate certain layers and circles (o) indicate uncertain layers. For this section, the manual layer counts have a bias towards counting too few layers in total. This is a general tendency of the manual timescale, resulting in a manually-counted age for the Pleiades tephra that is a few decades younger than observed in WAIS Divide.

Formatted: Font: (Default) Times New Roman, 12 pt, Bold

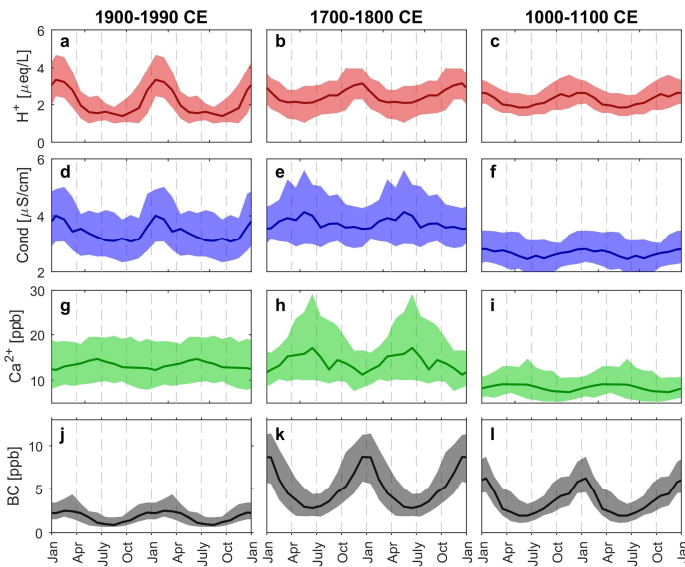
1490
1491

1492 **Figure 67: a)** Vertical velocity profiles for divide-like flow and flank flow (Kingslake et al.,
 1493 2014). For divide flow is plotted the preferred Liboutry-fit along with the measured vertical
 1494 velocities (blue dots). Vertical velocity measurements (Kingslake et al., 2014) and the
 1495 associated fitted functions. Fit used here improves overall misfit and does not have a bias at
 1496 mid-depth. b) Thinning function with associated 95% confidence interval uncertainties (2 σ). c)
 1497 Radar echogram (Kingslake et al., 2014) with traced layers (red) and location of maximum
 1498 amplitudes of the stack of Raymond arches (blue circles). The location of the modern
 1499 topographic ice divide (and the RICE drill site) is marked by the returns from a pole. The core
 1500 site is located west of the maximum bump amplitudes at depth, as indicated with an arrow.

1501

1502

1503

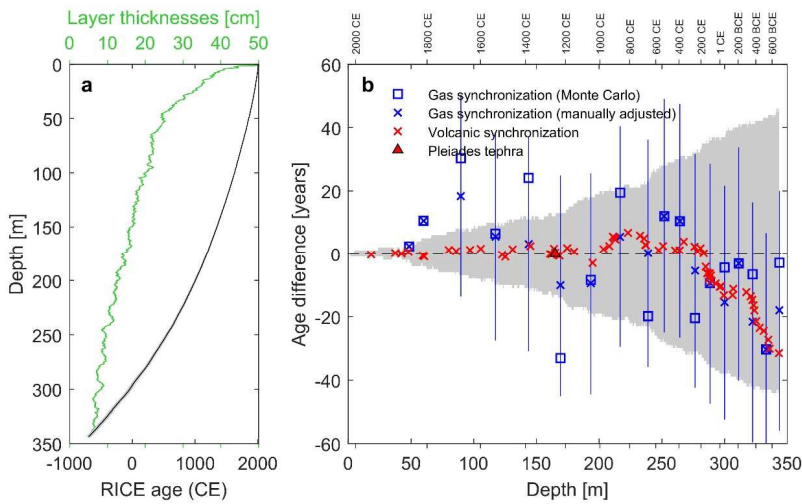


1504

1505 **Figure 8:** Average annual signals of 2 successive years in ~~RICE~~ **a-c**) acidity (H^+), **d-f**)
1506 conductivity (Cond), **g-i**) calcium (Ca^{2+}), and **j-l**) black carbon (BC) during three centuries,
1507 calculated under the assumption of constant snowfall through the year. The main RICE CFA
1508 data only extends to 1990_CE. The line shows the monthly-averaged median value of measured
1509 concentrations, and colored area signifies the 50% quantile envelope of the value distribution.

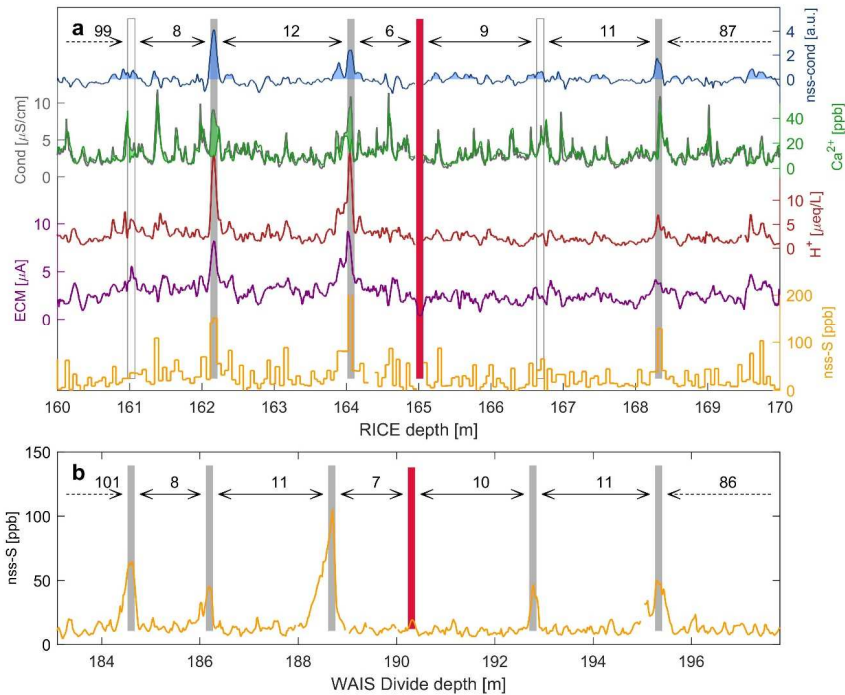
1510

1511
1512



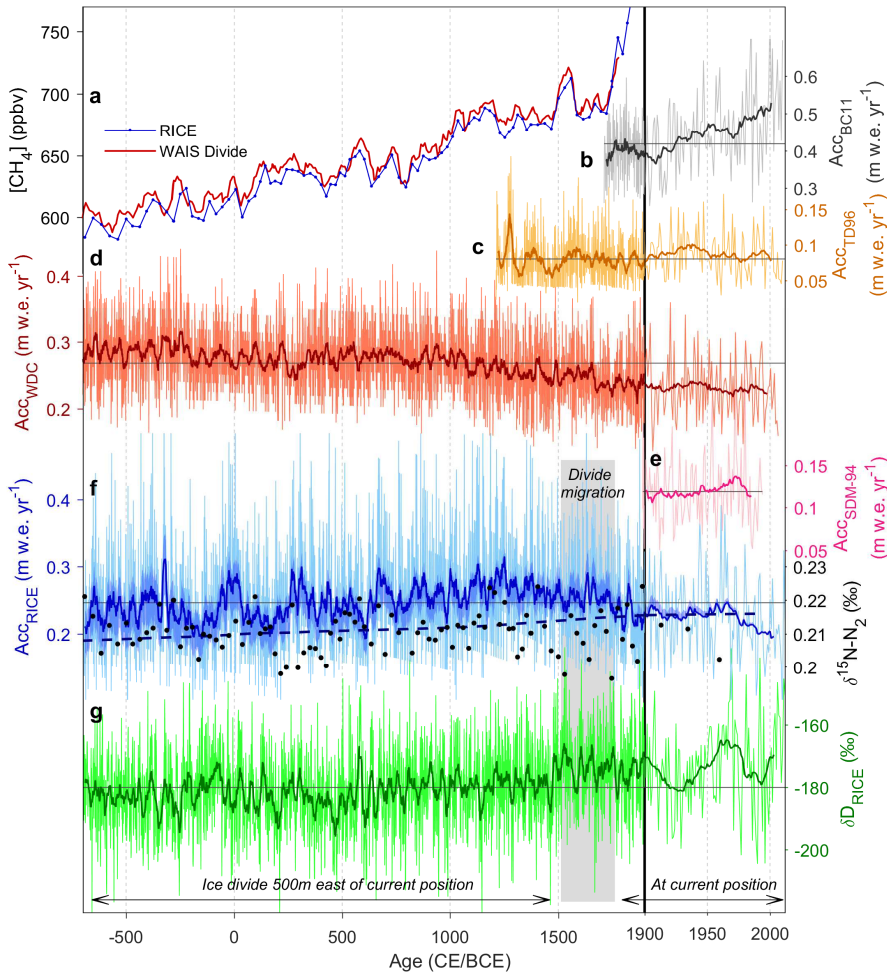
1513

1514 **Figure 98:** a) Depth evolution of RICE17 ages (black), including the associated 95%
1515 confidence interval (grey area, almost invisible due to scale), and corresponding mean layer
1516 thicknesses (50 year running mean; green). b) Comparison of RICE17 ages and 1-sigma confidence
1517 interval (grey area) to WD2014 from volcanic (red) and gas (blue) matching to WAIS Divide.
1518 A negative age difference implies fewer layers in RICE17 than in WD2014. Blue vertical lines
1519 represent 1-sigma age uncertainties on Monte Carlo methane matches. The solid red
1520 triangle indicates the Pleiades tephra layer at 165m depth.



1521
 1522 **Figure 109:** a) The RICE volcanic proxy records: non-sea-salt-sulfur (nss-S; orange), ECM
 1523 (purple), acidity (H^+ ; red), and non-sea-salt conductivity (nss-cond; blue) based on the
 1524 conductivity-to-calcium (grey, green) excess (grey, green). Green and blue areas are sections
 1525 of positive excess. b) Matching of the RICE records to the WAIS Divide non-sea-salt sulfur
 1526 record (Sigl et al., 2015). Vertical bars indicate volcanic match points (Table 2), with the
 1527 number of annual layers between match points in the two records given according to their
 1528 respective timescales. †The red bar represents the Pleiades tephra horizon (1251 CE). Two
 1529 match points (grey bars) had prominent peaks in most records, and an average significance
 1530 exceeding two standard deviations of the general variability of the signal, while the peaks
 1531 corresponding to two other match points (white bars) were less significant. However, direct
 1532 comparison of calcium and conductivity records revealed significant conductivity excess also
 1533 at these depths.

1534
 1535



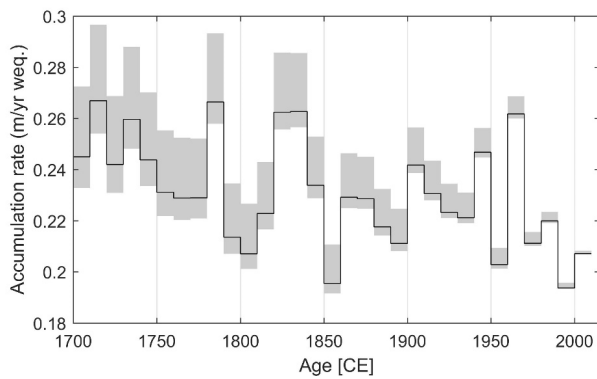
1536

1537 **Figure 101:** **a**) Measured methane concentrations from RICE (blue, on the RICE17 timescale)
 1538 and from WAIS Divide (red, on the WD2014 timescale). **b**) Bryan Coast (BC11, grey),
 1539 Ellsworth Land (Thomas et al., 2015), **c**) Talos Dome (TD96, orange), Northern Victoria Land,
 1540 (Frezzotti et al., 2007; Stenni et al., 2002) (no thinning function applied, extended to 2010 CE
 1541 using stakes measurements), **d**) WAIS Divide (WDC, red), Central West Antarctica (Fudge et
 1542 al. 2016) (corrected for ice advection), **e**) Siple Dome (SDM-94, pink), Marie Byrd Land
 1543 (Kaspari et al. 2004), and **f**) RICE (blue) accumulation histories over the past 2700 years, in
 1544 annual resolution and 20-year smoothed versions (thick lines). The shaded blue area indicates
 1545 the 95% confidence interval of the RICE accumulation rates. The short-lived peak in
 1546 accumulation rates around 320 BCE is likely to be an artefact caused by timescale inaccuracies
 1547 in this period, during which RICE17 diverges from WD2014 (Fig. 9b). Also shown are the gas-

1548 derived accumulation rates for this time interval (f, blue dashed line), and measurements of
 1549 $\delta^{15}\text{N}$ of N_2 informing on past firn column thickness (f, black dots; on the RICE gas timescale).
 1550 **g)** RICE stable water isotope record (δD). Thick green line is a 20-year smoothed version of
 1551 the isotope profile. Grey horizontal lines ~~denote~~ indicate mean values of the respective
 1552 accumulation rates and δD over the displayed period. Note that the scale changes at 1900_CE
 1553 (thick vertical line). The migration period of the Roosevelt Island ice divide is marked with a
 1554 grey box.

1555

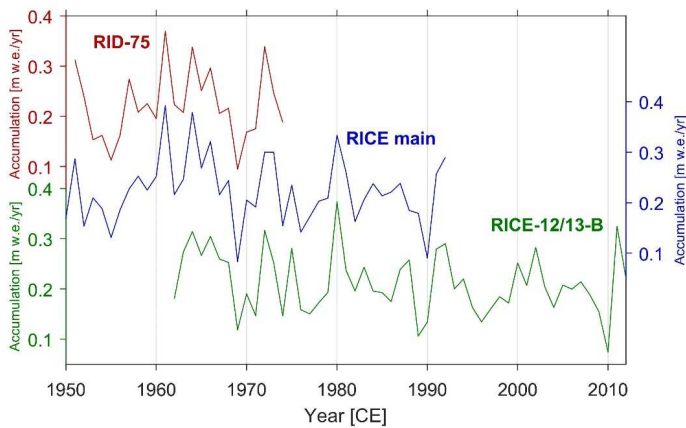
1556



1557

1558 **Figure 142:** Decadal accumulation rates at Roosevelt Island since 1700 CE. Grey shadows
 1559 indicate the 95% uncertainty bounds on the accumulation rate reconstruction due to
 1560 uncertainties in the thinning function.

1561



1562

1563 **Figure 143:** Accumulation reconstructions since 1950 CE for the three Roosevelt Island ice
 1564 cores described in Table 1.

1565

1566

1567

1568 **Tables**

Ice core:	RID-75	RICE	RICE-12/13-B
Drilled	1974/75	2011/12 (0-130 m) 2012/13 (130-764.6 m)	Jan 2013
Depth	0-10.68 m	8.57-764.60 m	0-19.41 m
Location	79°22' S, 161°40' W	79°21.839' S, 161°42.387' W	79°21.726' S, 161°42.000' W
Data sets:			
β -activity	16 cm resolution (Clausen et al., 1979)	-	-
$\delta^{18}\text{O}$, δD	Only $\delta^{18}\text{O}$; 4 cm resolution (Clausen et al., 1979)	Continuous and 2 cm resolution (Bertler et al., 2018)	Continuous and 2 cm resolution (Bertler et al., 2018)
CFA	-	H^+ , Ca^{2+} , conductivity, dust, BC; 8.57-344 m; continuous (this work)	H^+ , Ca^{2+} , conductivity, dust, BC; continuous (this work)
ECM	-	49-344 m; continuous (this work)	-
IC	-	Na^+ , Ca^{2+} , Mg^{2+} , SO_4^{2-} ; 8.57-20.6 m; 4 cm resolution (pers. comm., N. Bertler)	Na^+ , Ca^{2+} , Mg^{2+} , SO_4^{2-} ; 4.5 cm resolution (pers. comm., N. Bertler)
ICP-MS	-	S, Na, I; 8.57-249 m; 2-7 cm resolution (pers. comm., P. Mayewski)	S, Na, I; 9.5 cm resolution (pers. comm., P. Mayewski)
	-	Pu^{239} ; 8.64-40m; 4 cm resolution (pers. comm., R. Edwards)	-
CH_4 $\delta^{18}\text{O}_{\text{atm}}$	-	Discrete samples (Lee et al., 2018)	-

1569

1570 **Table 1:** The Roosevelt Island ice and firm core records used in this study.

1571

Depth (m)	RICE17 age (CE)	Significance of volcanic peak (σ)	Event	WD2014 age (CE)
0	2013.0±0	-	Snow surface in RICE-12/13-B (Jan 2013)	-
14.62	1975.1±1	=	Isotope match to RID-75 snow surface (winter 74/75)	-
16.18	1970.9±1	=	Radioactivity peak (winter 1970/71 ¹)	-
18.10-18.20*	(1965.0-1965.2) ±1	=	Tephra likely from Raoul Island, New Zealand (Nov 1964)	(1964.7-1964.9) ±1
21.98	1954.7±1	-	Onset of high radioactivity levels from Castle Bravo, Marshall Islands (March 1954)	-
37.45	1903.8±1	2.7	Santa Maria, Guatemala (Oct 1902)	1904.0±1
42.34	1885.0±1	1.3	Krakatau, Indonesia (Aug 1883), bipolar	1885.0±1
47.90	1863.3±2	>3	Makian, Indonesia (Dec 1861), bipolar	1863.9±1
59.46 [#]	1817.0±4	1.9	Tambora, Indonesia (April 1815), bipolar	1816.4±0
80.09 [#]	1722.3±6	2.0	Unknown	1723.5±1*
85.99	1695.0±6	1.0	Unknown, bipolar	1695.8±1
97.12	1641.2±7	2.0	Parker Peak, Philippines (Jan 1641), bipolar	1642.4±1
105.58 [#]	1599.3±8	2.3	Huaynaputina, Peru (Feb 1600), bipolar	1600.9±1
122.67	1507.0±10	1.9	Unknown	1506.7±2
125.19	1493.4±10	2.8	Unknown	1492.4±2*
131.04	1458.4±10	>3	Kuwae, Vanuatu, bipolar	1459.8±2
145.15	1376.2±11	2.0	Unknown	1378.7±2
161.02	1277.3±12	1.2	Unknown	1277.2±2
162.17	1269.9±13	>3	Unknown	1269.7±2
164.06	1257.3±13	>3	Samalas, Indonesia, bipolar	1258.9±1
165.01-165.02*	1251.5±13	=	Tephra from the Pleiades, West Antarctica	1251.6±2
166.68	1242.3±13	1.0	Unknown	1241.9±2

Formatted: table

Formatted: table, Centered

Formatted: Centered

168.32	1231.4±13	> <u>3</u>	Unknown, bipolar	1230.7±2	Formatted: Centered
174.50	1190.1±14	<u>1.2</u>	Unknown, bipolar	1191.9±2	Formatted: Centered
180.01	1152.3±16	<u>1.9</u>	Unknown	1153.0±2	Formatted: Centered
194.81	1043.3±18	<u>2.9</u>	Unknown	1040.3±2	Formatted: Centered
203.44	974.5±19	<u>2.8</u>	Unknown, bipolar	976.0±2	Formatted: Centered
208.11	937.1±20	<u>1.0</u>	Unknown	939.6±2*	Formatted: Centered
211.02 ^s	912.6±20	<u>2.0</u>	Unknown, bipolar	918.1±2	Formatted: Centered
212.03 ^x	903.9±20	<u>2.6</u>	Unknown	909.0±2*	Formatted: Centered
212.88 ^x	896.3±20	<u>1.9</u>	Unknown, bipolar	900.9±2	Formatted: Centered
222.94	813.2±20	<u>2.3</u>	Unknown, bipolar	819.9±2	Formatted: Centered
232.66	720.3±21	≥ <u>3</u>	Unknown	726.1±2	Formatted: Centered
235.78	693.1±22	<u>2.0</u>	Unknown, bipolar	698.0±2	Formatted: Centered
236.94	683.0±22	<u>1.7</u>	Unknown, bipolar	685.9±2	Formatted: Centered
237.25	680.1±22	≥ <u>3</u>	Unknown, bipolar	682.9±2	Formatted: Centered
247.49	575.1±27	<u>2.1</u>	Unknown, bipolar	576.2±2	Formatted: Centered
250.93	539.2±27	<u>1.4</u>	Unknown, bipolar	541.7±3	Formatted: Centered
260.59	434.3±29	> <u>3</u>	Unknown, bipolar	435.4±3	Formatted: Centered
264.19	394.4±30	<u>2.5</u>	Unknown, bipolar	395.5±3	Formatted: Centered
267.41	356.9±30	≥ <u>3</u>	Unknown, bipolar	360.8±3	Formatted: Centered
276.06	264.3±31	> <u>3</u>	Unknown, bipolar	266.6±3	Formatted: Centered
278.41	236.4±31	<u>1.4</u>	Taupo (New Zealand), bipolar	237.1±3	Formatted: Centered
280.82	205.3±32	<u>2.5</u>	Unknown	207.1±3	Formatted: Centered
283.36 [†]	170.9±33	<u>1.5</u>	Unknown, bipolar	171.0±3	Formatted: Centered
284.97	148.1±34	<u>1.1</u>	Unknown	143.9±3	Formatted: Centered
286.17	131.6±35	<u>2.8</u>	Unknown	125.3±4	Formatted: Centered
286.40	128.1±35	<u>2.8</u>	Unknown	121.9±4	Formatted: Centered
287.49	113.4±35	<u>1.5</u>	Unknown	105.5±4	Formatted: Centered
288.11	105.2±35	<u>2.3</u>	Unknown	97.8±4*	Formatted: Centered
288.35	102.3±35	1.8	Unknown	96.0±4	Formatted: Centered
289.18	90.8±36	<u>2.6</u>	Unknown	83.8±4	Formatted: Centered
289.54	86.2±36	<u>1.4</u>	Unknown	77.5±4*	Formatted: Centered
292.80	41.2±37	<u>2.2</u>	Unknown	31.7±4	Formatted: Centered
296.12 [#]	3.1±37	<u>1.8</u>	Unknown	-7.5±4	Formatted: Centered
297.24 [#]	-10.4±37	<u>2.2</u>	Unknown	-20.3±4	Formatted: Centered

299.30 [#]	-34.0±37	<u>1.8</u>	Unknown	-46.3±4
306.39	-130.9±39	<u>2.3</u>	Unknown	-143.1±4*
306.89	-137.9±39	> <u>3</u>	Unknown	-148.1±4
317.30	-295.9±41	> <u>3</u>	Unknown	-307.2±4*
320.87	-344.4±41	> <u>3</u>	Unknown	-357.0±5
322.15	-362.8±41	<u>1.8</u>	Unknown	-376.5±5
323.14	-376.7±41	<u>2.1</u>	Unknown	-392.1±5
323.84	-385.7±42	<u>1.6</u>	Unknown	-402.7±5*
325.25	-405.7±42	> <u>3</u>	Unknown	-426.1±5*
328.05 [*]	-446.6±42	3.1	Unknown	-469.1±5*
331.21	-496.4±43	<u>2.3</u>	Unknown	-519.9±5*
334.94	-554.7±43	> <u>3</u>	Unknown	-581.0±5*
335.84	-567.5±43	> <u>3</u>	Unknown	-596.6±5*
343.30 [#]	-691.5±44	<u>2.7</u>	Unknown	-722.0±6*

1573 †: Age from Clausen et al. (1979). ★ Depths indicate the tephra sampling interval. #: CFA acidity is missing for
1574 relevant interval, attribution is based on remaining records. † Significant peak only in nss-conductivity CFA acidity
1575 does not record peak. x: Conductivity and Ca records missing for interval. ✖: CFA and IC data missing, depth
1576 annotation based on ECM only. *: Eruption not identified in existing compilation of volcanic eruptions in WAIS
1577 Divide (Sigl et al., 2013).

1578 **Table 2:** Marker horizons used for development and validation of the RICE17 chronology.
1579 Strata in bold were used for constraining the timescale. The statistical significance of volcanic
1580 peaks in the RICE records (column 3) is given in terms of the average peak size in smoothed
1581 and standardized versions of the four records (ECM, H⁺, nss-cond, nssS (down to 249m)),
1582 computed relative to a running mean and standard deviation. Volcanic matching to WAIS
1583 Divide allows comparison between RICE17 ages (with 95% confidence interval indicated) and
1584 the corresponding WD2014 ages with associated uncertainties (Sigl et al., 2015, 2016).
1585 Indicated depths and ages correspond to peaks in the volcanic proxies. Below 42.3m, decimal
1586 ages have been calculated assuming BC to peak Jan 1st. Historical eruption ages (in column
1587 43) indicate starting date of the eruption. In column 34 is also stated whether the eruption
1588 previously has been observed to cause a bipolar signal, based on the compilation in Sigl et al.
1589 (2013), here updated to the WD2014 timescale. Since this compilation only identifies bipolar
1590 volcanoes back to 80 CE, volcanoes prior to this are not classified. Three exceptionally large
1591 volcanic signals observed in the RICE core are indicated in italics.

Formatted: Centered

Formatted: Danish

Field Code Changed

Formatted: Danish

1593

Change point	Time period (rounded)	Mean accumulation rate [m. w.e./yr]	Accumulation rate trend [mm w.e. yr ⁻²]
1287 CE (1291 ± 135)*	700 BCE – 1300 CE	0.25 ± 0.02 3	+0.02 (0.020 ± 0.003)
1661 CE (1675 ± 123)*	1300 CE – 1650 CE	0.26 ± 0.03 2	-0.04 (-0.03 ± 0.03)
1966 CE (1969 ± 34)	1650 CE – 1965 CE	0.24 ± 0.02 1	-0.10 (-0.08 ± 0.05)
	1965 CE – 2012 CE	0.21 0 4 ± 0.002	-0.80 (-0.84 ± 0.76)

1594

*Change point not well-determined from bootstrap analysis.

1595 **Table 3:** Mean value and trends in RICE accumulation rates during various time periods.
 1596 Change points and trends are found using break-fit regression (Mudelsee, 2009). The most
 1597 likely change-points and trend values are provided, as well as the associated confidence
 1598 intervals (in parenthesis: median and median absolute deviation; ~~Mudelsee (2000)~~ determined
 1599 from block bootstrap analysis. Uncertainties (95% confidence interval~~es~~) on mean
 1600 accumulation rates are calculated based on the uncertainty in the accumulation reconstruction.
 1601 Accumulation trends estimates from the bootstrap analysis (in parenthesis) includes
 1602 uncertainties in determination of the change-point, but not uncertainties associated with the
 1603 derived accumulation rate history. The analysis does not account for a potential bias due to ice
 1604 divide migration, which may slightly affect the mean accumulation rate values prior to 1750
 1605 CE, and the trend during the period of divide migration (~1500-1750 CE).

1606

1607

Rank	Decade	Decadal mean accumulation rate [m. w.e./yr]
1	1990-1999	0.194 ± 0.001
2	1850-1859	0.197 6 ± 0.010
3	1950-1959	0.204 3 ± 0.004 6
4	1800-1809 1800-2000- 2009	0.207 ± 0.013 0.207 ± 0.001
5	2000-2009 2009-1800- 1809	0.208 7 ± 0.001 4 7
6	1970-1979	0.212 1 ± 0.004 8

1608

1609 **Table 4:** Ranking of decades since 1700 CE according to lowest mean accumulation.
 1610 Uncertainties (~~26~~95% confidence interval) on the mean values are due to uncertainties in the
 1611 accumulation reconstruction.

Supplementary material

S1. Effective depth resolution of the CFA records

Effective depth resolution of the CFA records ~~was~~ evaluated based on the time it took for the various measurement lines in the system to respond to an abrupt change in concentration level. Following the approach in Bigler et al. (2011), response times were calculated as the average time required for the system to transition from a blank water standard to the highest calibration standard plateau, using the 10% and 90% levels of the transition curve. From the employed melt rate of 3 cm/min, response times were then converted to equivalent response depths as a measure for the effective depth resolution. For the RICE CFA set-up, the conductivity record has the highest effective resolution of 0.8 cm, closely followed by black carbon (Table S1).

	Response time (s)	Response depth (cm)	Missing data fraction
Conductivity	15 ± 2	0.8 ± 0.1	6%
Acidity	38 ± 3	1.9 ± 0.2	17%
Calcium	49 ± 6	2.5 ± 0.3	9%
Black carbon	20 ± 3	1.0 ± 0.2	<1%
Insoluble dust particles	17 ± 3	1.0 ± 0.2	8%

Table S1: Response times for the CFA system to transition between the blank water level and a calibration standard plateau, and the equivalent response depths. Core breaks, contamination, measurement errors etc. gave rise to sections of missing data, these comprising from 1% to 17% of the total length of the record. Below 129 m, the dust record was extensively contaminated by drill liquid, and the missing data fraction is calculated for the uncontaminated top part only.

S2. StratiCounter settings and procedure

StratiCounter was initialized based on a preliminary set of manual layer annotations (Fig. 6a) within a selected depth interval (40-150 m). The manual annotations were used to produce a set of generalized templates for an annual layer in the various impurity records. We note that the manually-counted timescale was observed to have a bias towards counting too few layers, resulting in an age for the Pleiades tephra that is a few decades younger than observed in WAIS Divide. Applying the Expectation-Maximization algorithm (e.g. Gupta and Chen 2010), StratiCounter continuously updates and refines the statistical description of an annual layer, thereby allowing for changes in layer characteristics with depth (Winstrup, 2016; Winstrup et al., 2012). To further increase the independence of the StratiCounter timescale from the preliminary manual interpretation, in a final step the entire timescale was reevaluated using an improved set of layer templates derived from the algorithm output.

Rapid thinning of layers with depth in the ~~RICE~~-core necessitated slight changes in StratiCounter settings with depth. We therefore divided the record into four sections: an upper

(42-180 m), an upper middle (165-250 m), a lower middle (240-300 m), and a lower section (280-344 m). Overlap sections served as base for comparison between the runs, which were found to contain only minor differences. Within these sections, the results from the deeper section were used to produce the final timescale.

For the uppermost section (42-180 m), performance of the algorithm was tested using a variety of algorithm settings, which all resulted in very similar timescales (± 10 years at 165 m). The final version was chosen as the timescale in best agreement with the WD2014 age of the Pleiades tephra horizon (Dunbar et al., 2010) found at 165 m depth (Kaltefleiter, 2015) (Wheatley and Kurbatov, 2017). Proceeding to the deeper sections, the algorithm settings were kept as similar as possible to those employed for the upper part (Table S2).

The main change in settings with depth was the averaging distance employed to produce a lower-resolution record from the original 1-mm resolution CFA records, performed before automatic layer identification. Section delimitations were selected based on estimated layer thicknesses obtained from methane matching to the WAIS Divide ice core (Lee et al., 2018), and chosen so that an average layer consisted of approximately 10-15 individual data points. Accordingly, the averaging distance was successively reduced from 1.5 cm to 0.5 cm to account for the general decrease in layer thicknesses with depth (Table S2). Note that the averaging distance applied for the deepest section is less than the effective resolution of even the highest-resolution impurity records (Table S1), meaning that successive averaged data points are significantly correlated.

StratiCounter was run based on the full suite of CFA records: Black carbon, acidity, calcium, conductivity, and dust (topmost section only). The dust record was excluded for the lower sections due to drill liquid contamination. The impurity records were weighted so that records of large similarity (e.g. the calcium and conductivity) were not treated as independent data series, and with added emphasis on the black carbon, which displayed the most pronounced annual signal (Table S2). Before analysis, extreme peaks caused by measurement noise and processing errors were removed from the data series. These were further standardized using z-scores based on the logarithm of the impurity concentrations in order to reduce inter-annual variability in layer signal.

Section	42.34–180 m	165–250 m	240–300 m	280–350 m
	(42.34-165 m)	(165-240 m)	(240-280 m)	(280-343.7 m)
Depth resolution (cm)	1.5	1.0	0.75	0.5
Weights of impurity series				
Black carbon	1	1	1	1
Acidity	0.5	0.5	0.5	0.5
Dust	0.5	0	0	0
Calcium	0.25	0.25	0.25	0.25
Conductivity	0.25	0.25	0.25	0.25

Table S2: StratiCounter settings for each depth range; (in parenthesis is given the interval for which the results were used to produce the final combined timescale): Interpolated depth

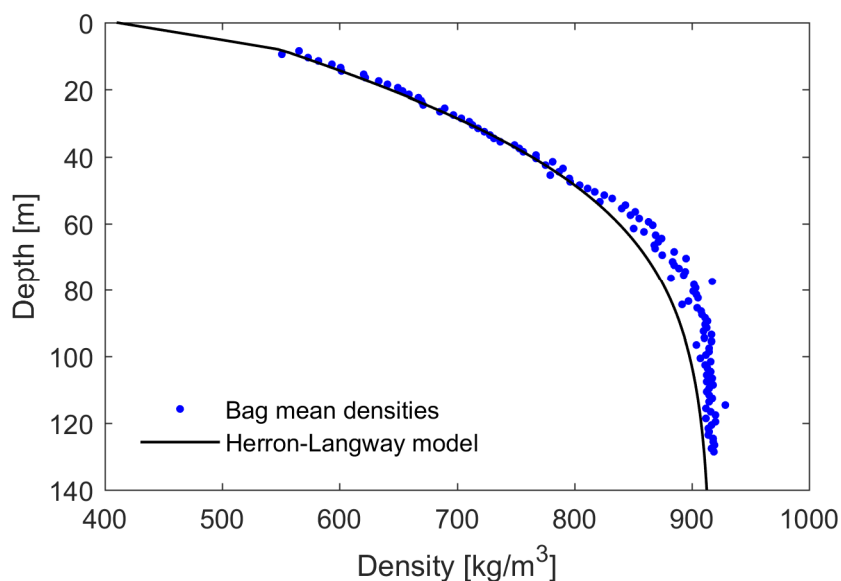
1 resolution of the impurity records before automated layer identification, and weighting of the
2 various impurity records in the StratiCounter algorithm.

3

4 **S3. The RICE density profile**

5 Measured densities for the RICE core (Fig. S1) show good agreement with a modelled density
6 profile calculated from a steady-state Herron-Langway densification model (Herron and
7 Langway, 1980) when using appropriate values for the initial snow density (410 kg m^{-3} ; within
8 the range measured in adjacent snow pits), surface temperature (-23.5°C ; consistent with
9 borehole temperatures (Bertler et al., 2018)), and accumulation rate ($0.22 \text{ m w.e yr}^{-1}$). The
10 measured density profile was extended to the surface using the modelled densities. We note
11 that the initial densification in the Herron-Langway model is parameterized as a linear function
12 of depth, depending only on initial snow density and surface temperature.

13 At intermediate depths (50-120 m), the observed density profile has slightly denser snow than
14 predicted by the Herron-Langway model, and, as a result, the firm-ice transition is reached at
15 significantly shallower depths than predicted by the model. This difference may indicate that a
16 steady-state assumption is invalid, or it may be due to the additional vertical strain present at
17 divide locations (Kingslake et al., 2014).



18

19 **Figure S1:** Measured and modelled density profile for the RICE core.

20 **S4: Modeling of the thinning function for reconstructing the** 21 **accumulation rate history**

22 **Model setup**

23 To calculate the thinning function, we employ a one-dimensional ice-flow model run at an
24 annual time step, which tracks the cumulative thinning of an ice layer. At each time step, the
25 full-depth vertical velocity profile is found by scaling the shape of the vertical profile (discussed
26 below) to the surface velocity. The vertical surface velocity is determined as the sum of the
27 accumulation rate and the rate of ice-sheet thinning, the latter assumed constant in time. Forced
28 with a time-dependent accumulation rate, the model computes the thinning function based on

1 integration of the vertical strain over time. Starting from an assumption of constant
2 accumulation, we iterate until the accumulation history and thinning function are consistent.
3 While the surface vertical velocity likely does not vary at annual timescales, the resulting
4 thinning functions are smooth, and no improvement comes from using a smoothed
5 accumulation history.

6 Typical shapes of respectively “pure divide flow” and “flank flow” vertical velocity profiles at
7 Roosevelt Island (Figure S2) were found by fitting Lliboutry-type ice-flow shape
8 parametrizations (Lliboutry, 1979) to englacial velocities measured from repeat phase-sensitive
9 radar measurements (Kingslake et al., 2014). However, no velocity measurements were
10 possible in the upper 90m due to effects of firn compaction, meaning that some assumptions on
11 the near-surface velocities were required. We therefore computed the thinning function using
12 two different parametrizations of the velocity profile.

13 As discussed in the main text, the divide may have migrated in the past, and the vertical velocity
14 profiles experienced by the ice in the core may thus have changed through time. To account for
15 this, we follow Nereson and Waddington (2002) and describe the vertical velocity profiles as
16 time-varying linear combinations of the divide and flank profiles. This allows a smooth
17 variation in the vertical velocity profiles through time.

18 **Uncertainties**

19 For RICE, there are three primary sources of uncertainty in estimating the thinning function: 1)
20 the shape of the vertical velocity profile where no measurements exist in the upper 90m, 2) the
21 history of changes in the vertical velocity profile as the divide may have migrated, and 3) the
22 rate of ice-sheet thickness change. Each source of uncertainty is discussed below.

23 The total uncertainty is estimated by calculating the thinning function using two possible
24 parametrizations of the vertical velocity profiles, two divide-history scenarios, and three
25 plausible rates of ice-sheet thinning, described below. The resulting accumulation histories are
26 shown in Figure S3. We define the uncertainty as the full range of these 12 scenarios, which
27 we interpret as a 95% confidence interval.

28 **The vertical velocity profile**

29 Following the work of Lliboutry (1979), the vertical ice-flow velocity profiles (w) at
30 normalized depth (ζ) can be parameterized using the vertical velocity at the surface (w_s) and a
31 shape factor (p):

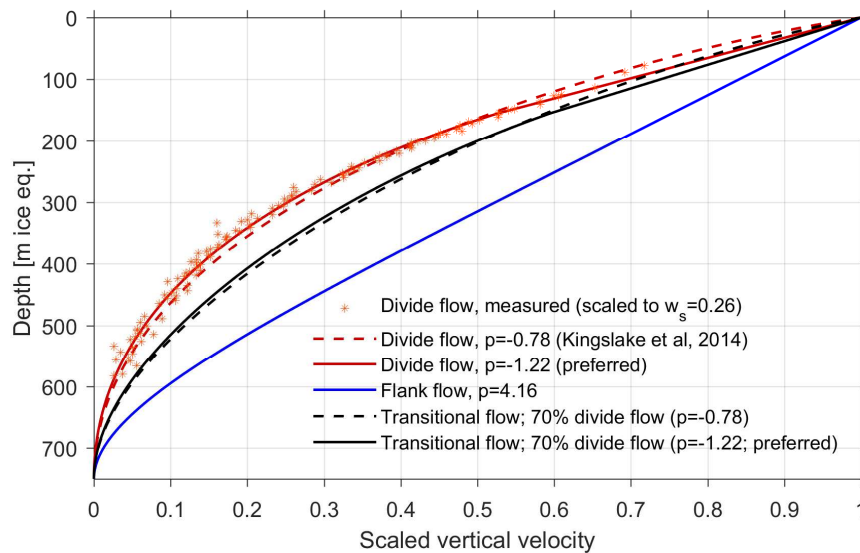
$$32 \quad w(\zeta) = w_s \left(1 - \frac{p+2}{p+1} \zeta + \frac{1}{p+1} \zeta^{p+2} \right)$$

33 Fitting to the vertical velocities measured for divide-like flow at Roosevelt Island (Fig. S2, red
34 asterisks), (Kingslake et al., 2014) found the best fit with a surface velocity (w_s) of 0.27 m/yr
35 and $p = -0.78$ (Fig. S2, red dashed line). However, this fit has two limitations: i) it over-predicts
36 the vertical velocity at mid-depths, and ii) given a recent accumulation rate of 0.24 m ice eq./yr,
37 it implies a thinning of the ice sheet of 0.03m/yr. This amount of ice-sheet thickness change is
38 at the upper limit of what is plausible given the observed structure of the Raymond Arch.

39 A more negative p value, $p = -1.22$, better matches the vertical velocity measurements, but
40 requires a larger surface velocity, which can be excluded. As noted by (Kingslake et al., 2014),
41 the vertical velocity profile is near-linear in the upper part of the measurements. We therefore
42 construct a second parametrization of the velocity profile as follows: We employ the Lliboutry
43 fit using $p = -1.22$, but replace the top part with a linear velocity increase towards the surface,
44 starting at 155m ice equivalent depth (Fig. S2, solid red line). This is our preferred vertical

1 velocity profile for divide-type flow at Roosevelt Island. The associated downwards surface
2 velocity of 0.26m/yr corresponds to an ice-sheet thinning rate of 0.02 m/yr, which is consistent
3 with the characteristics of the Raymond Arch.

4 For flank-type flow, the misfit to the measured vertical velocity measurements was minimized
5 using $w_s = 0.24$ m/yr and $p = 4.16$ (Fig. S2, blue line), for which good agreement between
6 measurements and model was obtained (Kingslake et al., 2014).



7
8 **Figure S2:** Vertical velocity profiles (scaled to the surface velocity, w_s) used for calculating the
9 RICE thinning functions. Two shape parametrizations for divide flow were used (red lines),
10 both derived from fitting to the measured vertical velocities (Kingslake et al., 2014). Our
11 preferred fit (solid red line) improves the overall misfit and does not have a bias at mid-depth.
12 For the flank-flow profile (blue), we used the fit from Kingslake et al. (2014). Also shown are
13 vertical velocity profiles for transitional flow (black lines), calculated as a linear combination
14 of the two profiles consisting of 70% divide flow and 30% flank flow, as appropriate for the
15 majority of the RICE core.

16 **Divide migration history**

17 As discussed in the main text, there is ambiguity in the history of divide migration, and how it
18 has influenced the vertical strain history at the core site. The main cause of uncertainty is the
19 inference of maximum near-surface strain rates, i.e. the most “divide-like” flow, being slightly
20 offset to the east of the present topographic divide (Kingslake et al., 2014; Fig 6b), where the
21 ice core was drilled. It may therefore be that the drill site is not located at the present location
22 of full divide-like flow. However, we note that there is considerable uncertainty in the pRES
23 measurements of vertical strain rates, and that these do not extent to within 90m of the surface.
24 In the near-surface layers, the peak of the Raymond Arch tilts towards to the modern summit,
25 suggesting that the divide (and the location of maximum divide-flow) has migrated towards the
26 current topographic summit in the most recent past. We consider this to be the most likely ice-
27 divide migration and corresponding flow history.

28 In our preferred scenario with recent divide migration, the older ice in the core experienced a
29 transitional flow regime somewhere between flank and ice-divide flow, but is now experiencing
30 full divide flow. Starting from ~120m (~1500 CE), the amplitude of the Raymond Arch at the

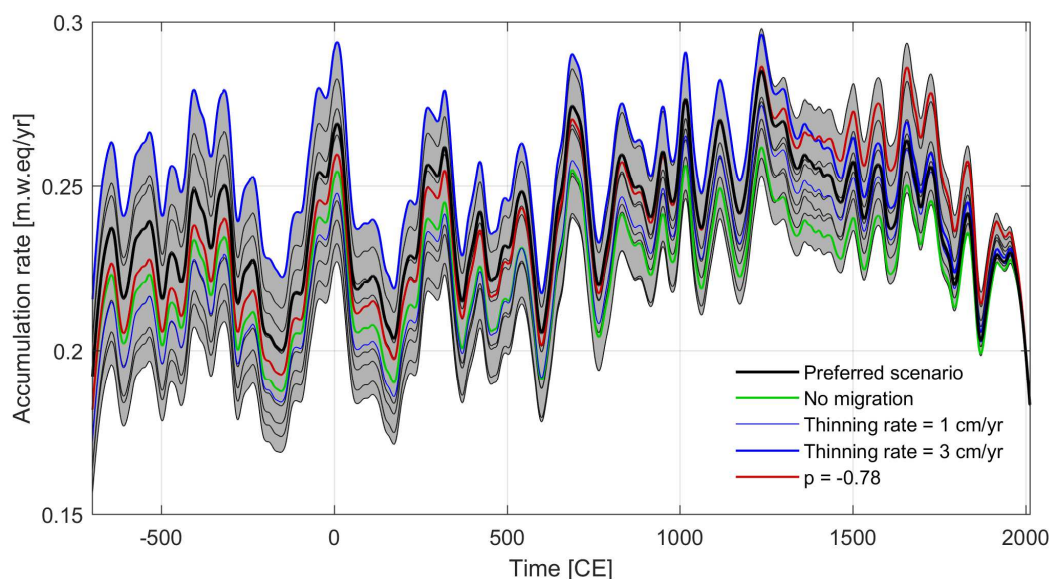
1 core site is approximately 70% of the peak amplitude. Prior to 1512 CE (500 years before the
2 core was drilled), we therefore used a vertical velocity profile appropriate for divide-flank
3 (70%/30%) transitional-type ice flow (Fig. S2; black lines). Over the following 250 years
4 (1512-1762 CE), the ice divide was assumed to migrate to its present position, while the vertical
5 velocity profile transitioned to full divide-type flow.

6 To account for the uncertainty in divide migration during the most recent past, the thinning
7 function was also calculated for the following second scenario: We assume that maximum
8 divide-flow has always been offset from the topographic summit, and thus that the ice in the
9 core has experienced entirely transitional flow.

10 **Ice-sheet thinning rate**

11 A third source of uncertainty is the amount of ice-sheet thickness change. Changes in ice-sheet
12 thickness will affect the vertical velocity, causing more vertical strain of layers in a thinning
13 ice sheet. For the deeper part of the ice core, changing the prescribed thinning rate is the most
14 important source of uncertainty for the accumulation rate reconstruction (Figure S3, blue lines).

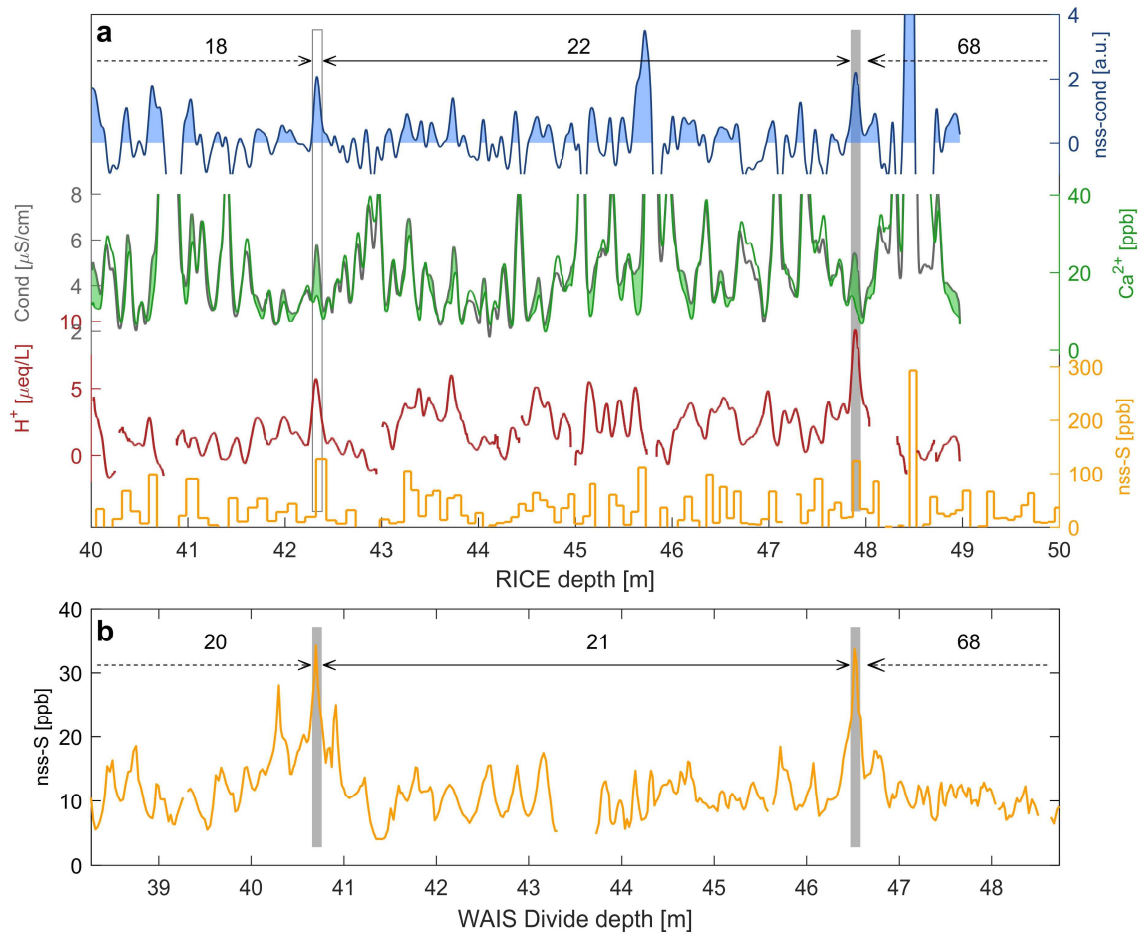
15 We assessed the plausible range of ice-sheet thickness change both by fitting the measured
16 vertical velocity profiles and by modeling the amplitude of the Raymond Arch. While 2D
17 modeling of the dated internal stratigraphy of Roosevelt Island is on-going, we find that the
18 likely range of ice-sheet thickness change is 1 to 3 cm/year, with 2 cm/year being the preferred
19 amount.



21 **Figure S3:** Reconstructed accumulation histories according to the 12 scenarios described in the
22 text. The 95% confidence interval (grey area) is taken as the envelope of all accumulation
23 histories. Colored lines show the impact on the accumulation history from the various sources
24 of uncertainty, when changing one of these at a time relative to the preferred scenario (thick
25 black line).

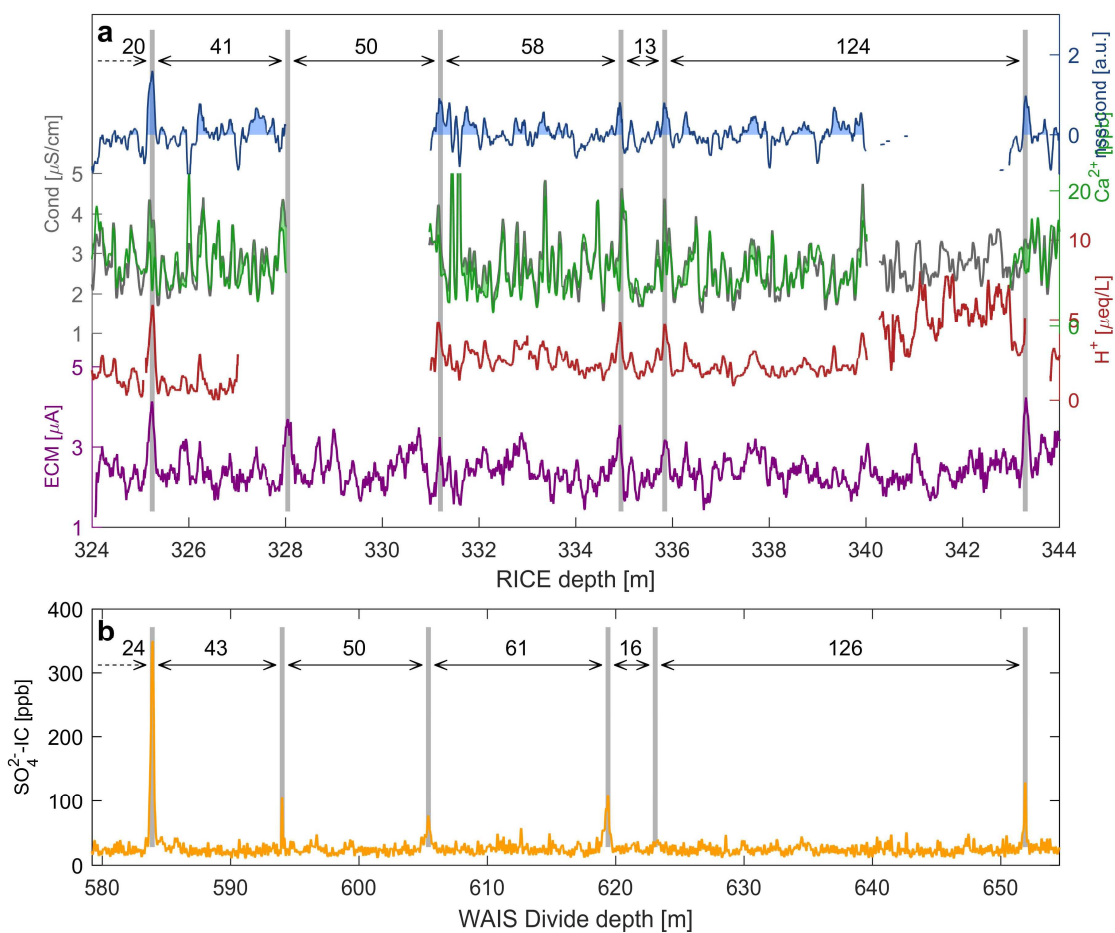
26

1 **S5: Volcanic matching to WAIS Divide**



2 **Figure S4:** Volcanic matching between **a)** RICE and **b)** WAIS Divide for a recent section,
 3 including the Krakatau (1883 CE) and Makian (1861 CE) volcanic horizons. Vertical bars
 4 indicate volcanic match points (Table 2), and numbers denote the number of annual layers
 5 between match points in the two records according to their respective timescales. Mean peak
 6 height for Krakatau (white bar) does not exceed 2σ of the internal variability (mean of all
 7 available records), but is clearly visible when e.g. comparing the Ca^{2+} and conductivity records
 8 directly. Green area shows the conductivity-to-calcium excess directly from the two records,
 9 with the resulting non-sea-salt conductivity record shown in the top panel.

10



1
2
3
4
5
6
7
8

Figure S5: Volcanic matching between **a)** RICE and **b)** WAIS Divide for the deepest part of the RICE record considered here. Vertical bars indicate volcanic match points (Table 2), and numbers denote the number of annual layers between match points in the two records according to their respective timescales. For this section, the RICE17 timescale shows a small, but distinct, bias towards counting fewer layers than present in WD2014.

1 Supplementary references

- 2 Bertler, N. A. N., Conway, H., Dahl-Jensen, D., Emanuelsson, D. B., Winstrup, M., Vallelonga,
3 P. T., Lee, J. E., Brook, E. J., Severinghaus, J. P., Fudge, T. J., Keller, E., Baisden, W. T.,
4 Hindmarsh, R. C. A., Neff, P. D., Blunier, T., Edwards, R., Mayewski, P. A., Kipfstuhl, S.,
5 Buizert, C., Canessa, S., Dacic, R., Kjær, H. A., Kurbatov, A. V., Zhang, D., Waddington, E.
6 D., Baccolo, G., Beers, T., Brightley, H. J., Carter, L., Clemens-Sewall, D., Ciobanu, V. G.,
7 Delmonte, B., Eling, L., Ellis, A. A., Ganesh, S., Colledge, N., Haines, S. A., Handley, M.,
8 Hawley, R. L., Hogan, C. M., Johnson, K. M., Korotkikh, E., Lowry, D. P., Mandeno, D.,
9 McKay, R. M., Menking, J. A., Naish, T. R., Noerling, C., Ollive, A., Orsi, A., Proemse, B. C.,
10 Pyne, A. R., Pyne, R. L., Renwick, J., Scherer, R. P., Semper, S., Simonsen, M., Sneed, S. B.,
11 Steig, E. J., Tuohy, A., Ulayottil Venugopal, A., Valero-Delgado, F., Venkatesh, J., Wang, F.,
12 Wang, S., Winski, D. A., Winton, V. H. L., Whiteford, A., Xiao, C., Yang, J. and Zhang, X.:
13 The Ross Dipole - temperature, snow accumulation, and sea ice variability in the Ross Sea
14 Region, Antarctica, over the past 2700 years, *Clim. Past*, 14, 193–214, doi:10.5194/cp-14-193-
15 2018, 2018.
- 16 Bigler, M., Svensson, A., Kettner, E., Vallelonga, P., Nielsen, M. E. and Steffensen, J. P.:
17 Optimization of high-resolution continuous flow analysis for transient climate signals in ice
18 cores, *Environ. Sci. Technol.*, 45(10), 4483–4489, doi:10.1021/es200118j, 2011.
- 19 Dunbar, N. W., Kurbatov, A. V., Koffman, B. G. and Kreutz, K. J.: Tephra Record of Local
20 and Distal Volcanism in the WAIS Divide Ice Core, in WAIS Divide Science Meeting
21 September 30th-October 1st, La Jolla, CA, USA. [online] Available from:
22 <https://geoinfo.nmt.edu/staff/dunbar/publications/abstracts/dakk2010.html>, 2010.
- 23 Gupta, M. R. and Chen, Y.: Theory and Use of the EM Algorithm, *Found. Trends® Signal*
24 *Process.*, 4(3), 223–296, doi:10.1561/20000000034, 2010.
- 25 Herron, M. M. and Langway, C. C.: Firn densification: an empirical model, *J. Glaciol.*, 25(93),
26 373–385, doi:10.3189/S0022143000015239, 1980.
- 27 [Kingslake, J., Hindmarsh, R. C. A., Adalgeirsdottir, G., Conway, H., Pritchard, H. D., Corr, H.](#)
28 [F. J., Gillet-Chaulet, F., Martin, C., King, E. C., Mulvaney, R. and Pritchard, H. D.: Full-depth](#)
29 [englacial vertical ice sheet velocities measured using phase-sensitive radar, *J. Geophys. Res.*](#)
30 [Earth Surf., 119, 2604–1618, doi:10.1002/2014JF003275, 2014.](#)
- 31 ~~[Kalteyer, D. A.: Tephra in Antarctic Ice Cores, Master Thesis, University of Maine, 2015.](#)~~
- 32 [Kurbatov, A. V., Kalteyer, D. A., Dunbar, N. W., Yates, M. G., Iverson, N. A. and Bertler, N.](#)
33 [A.: Major element analyses of visible tephra layers in the Roosevelt Island Climate Evolution](#)
34 [Project ice core \(Antarctica\), *Interdiscip. Earth Data Alliance*, doi:10.1594/IEDA/100554,](#)
35 [2015.](#)
- 36 Lee, J., Brook, E. J., Bertler, N. A. N., Buizert, C., Baisden, W. T., Blunier, T., Ciobanu, G.,
37 Conway, H., Dahl-Jensen, D., Fudge, T. J., Hindmarsh, R. C. A., Keller, E. D., Parrenin, F.,
38 Severinghaus, J. P., Vallelonga, P., Waddington, E. D. and Winstrup, M.: A 83,000 year old
39 ice core from Roosevelt Island, Ross Sea, Antarctica, *Clim. Past Discuss.*, 1–44,
40 doi:10.5194/cp-2018-68, 2018.
- 41 [Lliboutry, L. A.: A critical review of analytical approximate solutions for steady state velocities](#)
42 [and temperatures in cold ice sheets, *Gletscherkd. Glazialgeol.*, 15\(2\), 135–148, 1979.](#)

43

- 1 [Nereson, N. A. and Waddington, E. D.: Isochrones and isotherms beneath migrating ice divides,](#)
2 [J. Glaciol., 48\(160\), 95–108, doi:10.3189/172756502781831647, 2002.](#)
- 3 Winstrup, M.: A Hidden Markov Model Approach to Infer Timescales for High-Resolution
4 Climate Archives, in Proceedings of the 30th AAAI Conference on Artificial Intelligence and
5 the 28th Innovative Applications of Artificial Intelligence Conference, pp. 4053–4061, AAAI
6 Press, Palo Alto, California, February 12 – 17, 2016, Phoenix, Arizona USA., 2016.
- 7 Winstrup, M., Svensson, A. M., Rasmussen, S. O., Winther, O., Steig, E. J. and Axelrod, A. E.:
8 An automated approach for annual layer counting in ice cores, *Clim. Past*, 8(6), 1881–1895,
9 doi:10.5194/cp-8-1881-2012, 2012.